# POLITECNICO DI TORINO

**Master's Degree in Aerospace Engineering**


**Master's Degree Thesis**

# Tip gap recess influence on the performance of a low speed, 1.5 stage, axial turbine

**Supervisors**

**Prof. Andrea FERRERO**

**M.Sc. Lorenzo FABRIS**

**Prof. Volker GÜMMER**

**Candidate**

**Matteo SOLESIO**

**December 2024**

# Summary

In modern aviation, turbofan engines are widely used, particularly in the commercial sector. Constant improvements in terms of thermodynamic and propulsive efficiency are essential to reduce in-flight emissions and operational costs. To achieve this outcome, every primary component of the propulsive system must be specifically designed and optimized. With this as the primary objective, an axial turbine is analyzed in this study. These machines are involved into the extraction of energy from a flowing stream of hot gas. As the fluid proceeds, flowing through the turbine, the rotation blading extracts work in the form of mechanical energy. Since the process is not ideal, various types of energy dissipation occur which include not only thermodynamic losses due to irreversibilities in the cycle but also aerodynamic losses and mechanical friction. These combined losses reduce the overall efficiency and limit the power extraction capability of the turbine.

This research examines the potential benefits in terms of performance of applying physical modifications to the rotating blade row of a shroudless, 1.5 stage axial turbine. A numerical evaluation of the flow field inside the machine is performed using the commercial Computational Fluid Dynamics (CFD) software Ansys. The validation of the obtained results is conducted by analyzing the experimental data of the Multi-stage Axial Turbine Research Facility at the ETH Zurich, which have been published by the Global Power and Propulsion Society (GPPS). Additionally, this work investigates the aerodynamics inside the turbine, focusing on the losses generated by the necessary presence of a clearance between the rotor blade and the outer casing of the rotating blisk. The resulting tip leakage mass flow is analyzed by addressing the flow structures responsible for the performance reduction.

Subsequently, modifications to the geometry of the studied region are applied by introducing recessed tip on the rotor blades. A parametric investigation based on the main geometrical dimensions of the tip cavity created is conducted. The results assess a strong dependency between the aerodynamics of the recessed tip and the overall efficiency. The reduction of the tip leakage flow due to the cavity leads to a decrease of turbine internal losses which is responsible for the performance improvements as demonstrated in the current work.

# Acknowledgements

In the following acknowledgments, I would like to express my sincere gratitude to those who have accompanied me in this journey, offering their friendship, encouragement, expertise and guidance.

I express my deepest gratitude to my family for their constant support and encouragement. During these five years, they have always believed in me, pushing me to strive for excellence, even in the face of challenges. Their constant presence and faith in my abilities have been an invaluable source of strength.

Heartfelt thanks go to my partner, to whom I owe special regard for her faith in me and support. Her confidence in my potential and her constant encouragement have inspired me to always face my limits, especially during difficult times.

To my friends, with whom I have shared every moment, celebrating milestones and overcoming obstacles. Each of you has enriched this experience, making each step both memorable and meaningful.

My sincere thanks to my co-supervisor at the Technical University of Munich (TUM), Lorenzo Fabris, who has meticulously guided me from the very beginning of this project. His expertise and patience have been instrumental in producing the work presented here.

I thank my supervisor at Politecnico di Torino, Professor Andrea Ferrero, for his availability and assistance, providing me with valuable direction and perspective.

My gratitude also goes to the Chair of Turbomachinery and Flight Propulsion at TUM, and especially to Professor Volker Gümmer, for the technical support extended to me. Their provision of a dedicated workstation was vital to the progress and completion of this project.

Finally, I am thankful to Professor Reza S. Abhari, head of the Laboratory of Energy Conversion at ETH Zurich, and to the Global Power and Propulsion Society, for publicly sharing the experimental data employed in this research.

# Table of Contents

# List of Figures

# List of Tables

# Chapter 1

# Introduction

In the past decades, the world has seen an exponential increase in air traffic, in both goods and passenger transport sector. As a direct consequence of this scenario, the operational costs managed by airline companies multiplied with the number of operational aircraft. Having this background, the need to reduce expenses has become crucial.

Maintenance and fuel consumption are often considered the two main categories in which operational costs are divided. While the first one relates to the entire aircraft, the latter specifically depends on the propulsion system, particularly on the engines, although other aspects, such as the aerodynamics of the aircraft structure, also play a role.

Nowadays, the world of aircraft engines is led by turbofan (in Figure 1.1). This machine is the result of decades of improvements in the field of air-breathing propulsion. It is driven by the Brayton thermodynamic cycle which consists, in the ideal case, in order, of one isentropic compression followed by an isobaric heat addition, an isentropic expansion and a second isobaric transformation. To fulfill this cycle, the engine is built of three main components: a compressor, a combustion chamber and a turbine. In particular, the turbine is responsible for the partial extraction of energy from the fluid, that has gained pressure and temperature in the upstream combustion chamber, which is used to drive the compressor and to supply secondary loads.

Gas turbines consist of blade rows, each built on different disks attached to the power shaft of the engine. Every group of disk plus blade row forms the so-called blisk [2]. Stationary and rotating blisks are placed alternately in the axial direction. Each block of stator and rotor blisk is typically called a stage. The stator row deflects and accelerates the flow, giving it the right circumferential velocity and angle, while the rotor row directly downstream extracts the energy reducing pressure and temperature of the fluid.

Since the turbine is located immediately downstream of the combustion chamber,

**Figure 1.1:** Cutaway of an aircraft turbofan engine [1]

the flow field which enters the stages is highly non-uniform and unsteady, with temperature and pressure values close to the maximum points experienced by the entire machine. These factors, combined with the expansion process, leads to high aerodynamics losses which affects directly the overall efficiency and the output power of the engine.

A significant reduction in performance is related to the necessary relative motion of rotor blades. To allow the blisk to rotate within the turbine's external casing, the radial tip of the blade must be physically separated from it, leaving a space called tip gap. This small clearance connects the pressure side with the suction side of the blade causing the creation of a secondary flow through it, driven by the circumferential pressure difference. As a consequence, relevant vortex structures are created along the suction side and downstream of the blade, interfering with the main flow. It's been quantified that tip leakage losses can account for up to one third of the total aerodynamic losses of a turbine stage, which comprehends also profile losses, related to the blade boundary layer, and endwall losses, generated by the casings boundary layers [3]. Moreover, the amount of fluid passing through the gap leads to a reduction of performance in terms of work extracted since is not actively turned by the blade. Finally, the working conditions of the tip are extremely relevant in terms of blade lifetime. This gap region experiences high velocity and high heat loads which can bring to rapid deterioration and therefore required effective and complex cooling systems.

Even though a tip clearance is required, minimizing it can lead to a reduction of the above-mentioned issues. In order to achieve the minimal distance between the external case and the rotor blade tip, it is therefore necessary to analyze accurately structural and thermal loads which the turbine is subjected to. Radial forces as

well as thermal expansion rates influence the dimensions of engine components causing the tip to rub against the casing, introducing deformations in aerodynamic performance and modification of the blade cooling system. Those phenomena are encountered more often in aero-turbines than in energy generation gas turbines since they can depend also on hard maneuvers such as landings.

To counteract these effects while reducing the impact of tip gap leakage on the overall performance of turbines, active controls, such as active cooling systems, or passive controls, such as modifications on the blade or casing geometries, have been studied.

This study focuses on reducing the gap secondary flow passively by recessing the tip blade. The recess consists of thin elevated rims on pressure and suction side in the radial direction. With this modification, in the event of rubbing, only the edges are affected while the inner portion of the tip bordered by the rims is kept at a lower radius, avoiding any issues related to cooling holes. A numerical steady flow study has been conducted using Ansys-CFX commercial solver on a 1.5 stage axial turbine. The results have been validated with experimental data acquired from the Multi-stage Axial Turbine Research Facility LISA-D, published by the Turbomachinery Laboratory at the Swiss Federal Institute of Technology Zurich (ETH). Afterwards, the resulting simulation with flat rotor blade tip has been considered as baseline case for the subsequent tip gap recess analysis. A parametric study, based on tip geometry modifications, has been performed, focusing on the effects of length, depth and width of the new cavities created. Eleven different configurations have been tested, addressing benefits and limitations of the tip recess technique in terms of aerodynamic contributions to overall efficiency, by comparing the obtained results with the nominal baseline simulation.

# Chapter 2

# Literature review

## 2.1 General reviews

Through the past decades, tip leakage losses have been widely studied and considerable amount of open literature has been published on the topic. The impact of these losses on the total aerodynamic losses in turbomachines, comprehending both compressors and turbines, has been quantified to be up to $\frac{1}{3}$ by Denton [3]. In particular, the work confirmed this magnitude specifically for unshrouded, low speed, axial turbines where the vorteces creation and the related entropy generation cover a wide percentage of the region in both spanwise and streamwise direction. The investigation of this phenomenon is therefore highly demanded.

The strategies tested for tip leakage reduction have been various in the past years and it is common to divide them into passive and active mechanisms. The first group of methods includes techniques such as injecting flow into the tip region and, more in general, the whole group of static geometry modifications, included shaping the blade tip and casing treatments. Active approaches, on the other hand, require real-time adjustments to the tip gap geometry or flow, which can be adapted based on specific mission conditions to achieve the best performance.

Regarding passive methods, alongside tip recess techniques, cooling systems have been widely studied by Dey et al. [4] and Rao et al. [5], [6]. The studies agreed on the effectiveness of injecting coolant from purge holes placed on the tip surface. The gain in performance was dependent on the tip leakage reduction due to virtual partial obstruction of the gap created by interaction between flows. Rao et al. [5] found through experiments that injection into the tip of a recessed blade through four cooling holes reduced the losses associated with tip leakage. In particular, the research by Rao et al. [5] discovered that the global optimum is achieved with an injected coolant mass flow of 0.6% of the passage mass flow into the tip area, as determined by the calculation of the average pressure loss

coefficient downstream.

Cooling using film instead of less larger holes has been proposed and studied by Rezasoltani et al. [7].

Regarding casing shaping, profiled endwalls were first proposed by Rose [8]. Following it, different endwall shapes have been proposed and thoroughly analyzed by Harvey et al. [9], followed by Hartland et al. [10]. Studies have been conducted on non-axisymmetric endwall designs. Germain et al. [11] and Schuepbach et al. [12] analyzed the utility of shaped endwalls for both stators and rotors. Finally, endwall shaping has been shown by Trent 500 engine [13] and Trent 900 engine [14] to yield good performances.

Other solutions have been proposed for the same purpose. Fences and grooves in different configurations have been applied in the works of Chung [15] and Aunapu et al. [16]. Trenches within the external casing of the rotor were investigated by Offenburg et al. [17]. For small clearances, the choice of a smooth shroud seemed to be the best option, while trenches become more effective as the tip gap increases. Moreover, important flow disturbances have been noticed to appear with the introduction of steps in the flow path.

## 2.2 Tip recess literature

In parallel with the growing awareness of the negative effects which the tip leakage flow is related to, a considerable number of tip profile modifications have been proposed. In 1982, Booth et al.[18] performed a series of experiments on different tip clearances with water as working fluid. They assessed that a 1% tip gap of the total blade span causes up to 2% of primary flow to leak and generates a loss of 1–3% in stage efficiency.

In more recent years, 3-dimensional numerical studies on tip recessed blade turbine have been conducted by different groups, analysing many different tip configurations and comparing them with flat tip base case. By Ameri et al. [19], 2% and 3% of blade span recesses were compared with the flat tip case. It was found that, despite a mass flow leakage reduction of 10% and 14% respectively, no significant benefits have been achieved in terms of stage efficiency. Yang et al. [20] studied different clearance heights of flat tip case, focusing on heat transfer and assessing a correlation between high peaks and large clearances. In another related work by Yang et al. [21], 3.77% of blade span recessed tip was compared with flat tip cases. It was found that the highest leakage reduction and heat transfer were related to the smallest tip gap (1% for blade span). Partial squealers have been analysed by Camci et al. [22]. The experiments with different configurations showed that these kind of rims can improve aerodynamic performances by weakening tip leakage vortex. Moreover, it has been assessed that suction side squealer are more

effective by reducing the total pressure losses relative to the vortex. Research by Krishnababu et al. [23] on different types of squealers showed that the double side squealer tips can achieve better results compared to the suction side only. In addition, they concluded that mass flow leakage and heat load rise up with increase in clearance gap height.

De Cecco et al. [24], in 1995, analyzed tip clearance issue on turbine performance in a wind tunnel. Gaps up to 15% of the blade chord were involved. Surprisingly, the results showed maximum losses for the 6% clearance case, while the 15% clearance case showed losses comparable to the zero-clearance case.

Acharya et al. [25] investigated different tip geometries and solutions. Among others, the following configurations were studied: pressure-side squealer, suction-side squealer, mean-camber line squealer, both pressure- and suction-side squealers located either along the blade edges or moved inwards, pressure-side winglet and inclined ribs on the blade tip. The examination concluded that the suction-side squealer achieved the best results in terms of leakage mass flow and heat transfer coefficient reduction.

A specific study on winglets has been presented by Saha et al. [26]. The research group analyzed pressure-side winglet for both flat and recessed cases. As a result, winglets exhibit great reduction of leakage mass flow if associated with flat tip, while they are less efficient when combined with squealers. The work of Zhou et al. [27] focused on similar configuration, conducting a parametric study on applying winglets of different size to flat tip, 0.5% and 1% recessed cases. The aim was the reduction of the driving pressure difference between pressure and suction side. The research group discovered that the pressure side winglet has low influence on performance. On the other hand, the effects of suction side one are similar to the flat case because of a balance between the benefits, in terms of pressure difference, on the leading edge and the opposite effect from the midchord to the trailing edge. Divergent results have been obtained by Coull et al. [28] which performed a parametric study on flat tips with different winglets. The study showed that large efficiency benefits can be achieved by placing winglets around the entire tip perimeter, although this increases overall heat loads due to the placement of more surface. Nevertheless, the use of only suction-side winglet achieves good results without increasing heat loads on the blade.

## 2.3 Tip gap aerodynamics

A considerable amount of research has been produced to understand and quantify the aero-thermal losses associated with turbine blade passage first and with the tip leakage flow then.

Structured and comprehensive reviews on secondary flows behavior have been

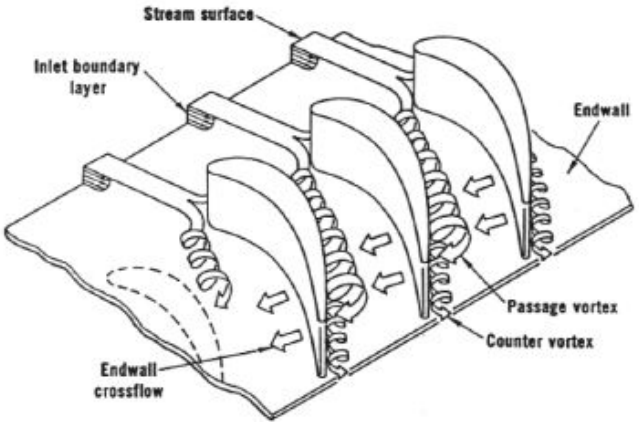


**Figure 2.1:** Langston's secondary flows schematic [30]

published by Sieverding [29] and Langston [30]. Through experimental studies and physical visualization (by means of coloured smoke or ink) the presence of three main vortex structures in the blade passage has been confirmed: the passage vortex, generated by the interaction between the inlet boundary layer and the turning blade which forces the flow through a curved passage, going from the pressure side to the suction side of two subsequent blades [29]; the horseshoe vortex which is created by the rolling-up of the endwall boundary layer when it interacts with the leading edge, generating two counter-rotating vorteces on both sides of the blade [31], [32] and the counter vortex, a smaller vortex in the suction side corner close to the endwall, rotating in opposite direction to the passage vortex and originated by the interference between the pressure side branch of the horseshoe vortex and the endwall right downstream the separation line on the suction side [29].

Regarding more specifically the blade tip gap aerodynamics of unshrouded turbine blades, Mischo et al. [33] described clearance flow structure as a result of cavity geometry optimization study. For the flat tip case, two main flow structures have been detected. The first vortex is generated by the interaction between the mainstream and the leading edge of the rotating tip. Two different streamlines can be identified as sources, the first one, starting from the suction side right close to the leading edge and the second one resulting from the mass flow flowing into the tip gap first 20% of the axial chord. The second structure is the so-called tip leakage vortex and it is generated by the mass flow passing through the gap, starting from 15% of the axial chord on the pressure side and exiting downstream through the suction side.

Concerning the recessed tip gap, the flow structure is highly dependent on the specific shaping of the tip. Nevertheless, common features can be identified. Mischo et al. [33] showed the presence of six different recursive flow structures for different

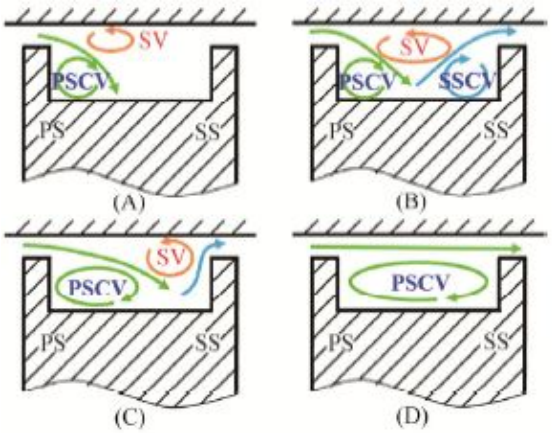


**Figure 2.2:** Typical behaviors of vortices inside the cavity [34]

geometries. First, the streamlines reaching the leading edge close to the stagnation point enter the cavity and collide on the opposite side in axial direction, creating a vortex as they move downstream in the cavity until they merge with the tip passage vortex. The boundary layer on the recess rim forms the second vortex which is split in two different structure immediately after entering the cavity. The two branches roll up running alongside the pressure and suction side respectively until they recombine downstream inside the cavity and finally join the passage vortex. A third vortex originates by the interaction between the endwall layer and the pressure rim. The other structures are similar to the one for the flat tip case, the passage vortex and the leakage vortex, with the difference that these are deviated inside the cavity due to the other structure described. Moreover, Mischo et al. [33] showed on a cutting plane orthogonal to the camberline the vortical structures detected in the cavity. This selection has been utilized by Zeng et al. [34] to analyze typical vortex layouts (Figure 2.2) and comprises: the scraping vortex (SV) which is dominant in tip-leakage flow reduction [35], the pressure side squealer corner vortex (PSCV) and the suction side squealer corner vortex (SSCV).

Although the generation of vorteces, as well as the introduction of steps related to the rims of cavities, necessarily leads to a higher grade of entropy generation and total pressure losses, a wide number of different investigations agree with the fact that the mass flow sealing introduced allows for better overall performance in terms of both aerodynamic efficiency and pressure losses. The reduction in terms of tip leakage weakens the entity of passage and leakage vorteces downstream of the blade and outside the tip gap [33], [34], [35].

# Chapter 3

# Turbine setup

The experimental validation case for the current numerical study was provided by the Turbomachinery Laboratory at Swiss Federal Institute of Technology Zurich (ETH) by publishing a complete dataset of unsteady flow measurements of the Multi-stage Axial Turbine Research Facility LISA-D at the Global Power and Propulsion Society (GPPS) Xi'an21 technical conference [36].

## 3.1 Global facility setup

The LISA-D facility, in Figure 3.1 consists of a three stage, quasi-closed air loop. The main components are a radial compressor, a calibrated Venturi nozzle for mass flow measurements, the turbine test stand, and a two-stage water to air heat exchanger.

The air flow is provided by a 750 $kW$ radial compressor with a maximum compression ratio of 1.5 and a maximum mass flow of 13 $kg/s$. The actual operating point can be set thanks to adjustable inlet guide vanes. Downstream of the compressor, the cooler system controls the temperature up to a maximum of $55°C$. Before entering the turbine test stand, the flow goes through a 3 meter long straight duct where it gains strength by reducing turbulence and aligning in axial direction thanks to honeycomb structures. The pipes between machines are designed to keep the stream velocity below 5 $m/s$ in order to reduce pressure losses before entering the turbine inlet.

The turbine is positioned with its main axis in vertical direction in the test rig. The configuration of stators and rotors can be changed as well as the number of stages by easily accessing from the first floor of the setup. The machine has an outer diameter of 800 $mm$ with a maximum rotational speed of 3000 $rpm$ and a maximum torque of 1500 $Nm$. The turbine exit is directly connected to an opening at the atmospheric pressure. The mechanical power is collected by two

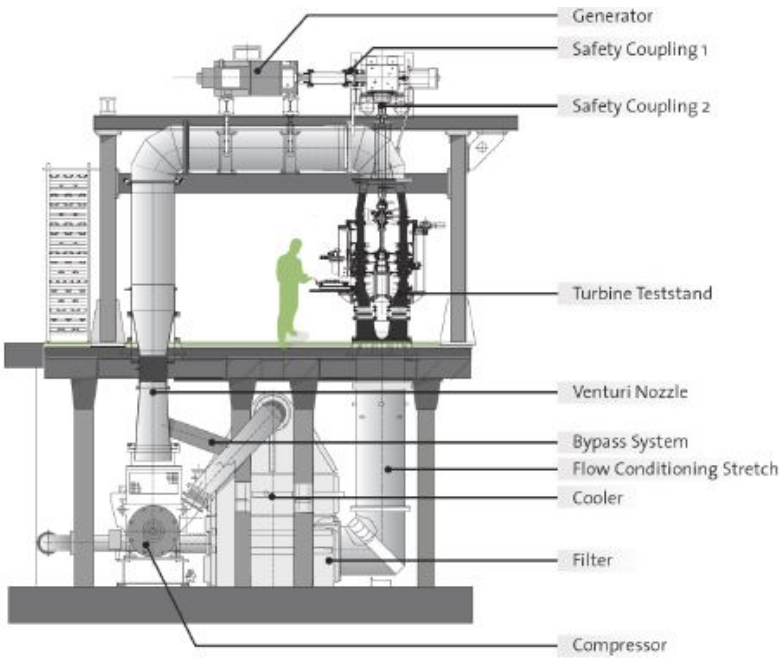


**Figure 3.1:** LISA-D experimental setup [36]

different shafts, which permit to gain different torque values in case of a two-stage configuration, with a 400 $kW$ DC generator. Downstream the turbine, before reaching the compressor, the flow passes through a Venturi nozzle for mass flow measurement. More detailed investigations on the experimental setup can be found in [37] and [38].

## 3.2 Measurement probes

The experimental data on which the results of the current work are validated have been obtained at two different planes downstream of each blade row of the turbine first stage. The time-resolved unsteady measurements were taken by the fast response aerodynamic probes (FRAP), which were developed at ETH Zurich [37].

The mainstream flow field was measured using three different FRAP probes with tip sizes of 5, 4, and 3 $mm$ in diameter, each containing four encapsulated piezo-resistive pressure sensors. With this hardware, time-resolved 3D flow-field quantities were derived. Measurements were captured at a sampling rate of 200 $kHz$ over a period of 2 $s$ with a bandwidth of 48 $kHz$, except for temperature which was limited to 10 $kHz$. A total of 85 rotor revolutions were recorded for Phase Lock Averaging (PLA) during these 2 seconds, corresponding to three blade passing

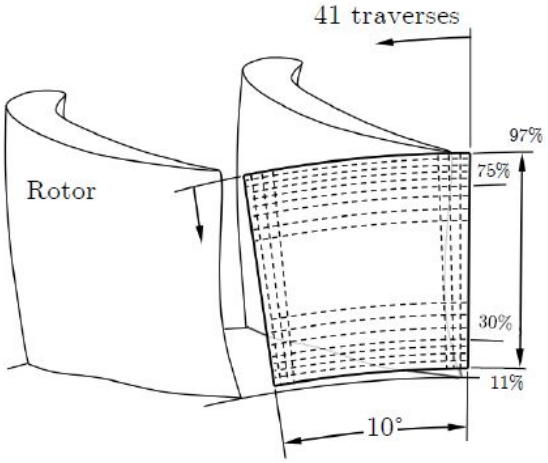


**Figure 3.2:** Measurements points distribution [36]

events. Each rotor passage had a resolving sampling rate of 82 points. The signals from probes were post-processed using low-pass filtering at 30 $kHz$. The following unsteady data were obtained from the main flow field: total and static pressure, yaw and pitch angle, Mach number, velocity and turbulence. Steady temperature values were also obtained. Detailed analysis and a study on the measurements acquisition and sensors setup can be found in [39].

Measurement planes were positioned downstream of both the stator and rotor of the first stage, each covering one stator pitch (10°). On each plane, the grid was composed of 41 points in circumferential direction and 35/36 in radial direction for first/second plane. Additionally, measurement points spanned from 11% to 97% of the blade span in the radial direction, with denser clusters of points located between 11% - 30% and 75% - 97% of span.

As a consequence of the measurement planes positions, the published experimental data which the validation process is referred to in chapter 4 are related to the first stage only. Therefore, rotor exit data is considered for the experimental/numerical comparison, while the data from the exit of the second stator is analyzed for the further recess study.

## 3.3 Turbine geometry and operational conditions

The validation case for the current study involves a high pressure, highly loaded, low aspect ratio turbine in a stator-rotor-stator configuration, entirely designed by the Turbomachinery Laboratory. The CAD model is shown Figure 3.3. Global turbine geometry and first-stage characteristics are presented in Table 3.1. Performance values were obtained from 5-hole-probe measurements at the design operating

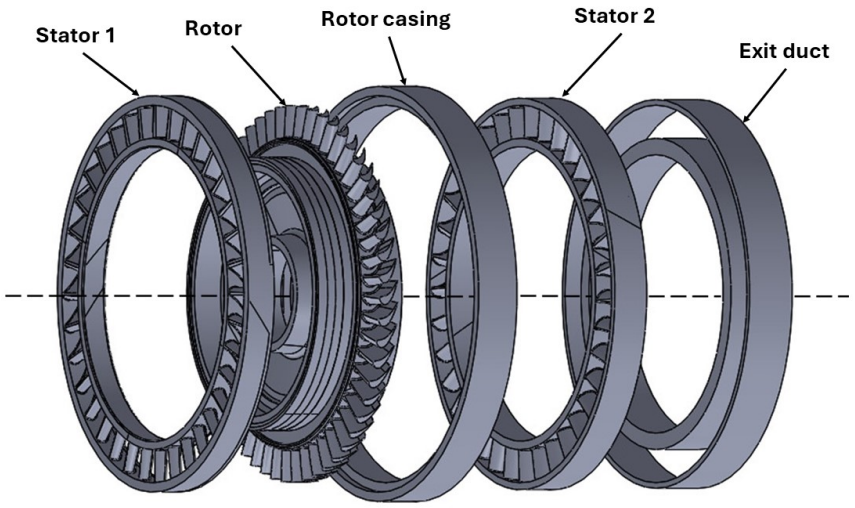


**Figure 3.3:** Exploded view of the turbine CAD model

point.

Geometry data of individual blade profiles are described in details by Behr [38]. In Table 3.3, only the most relevant values for the current study are presented. Specifically, the rotor blades present a 1% span cavity between the tip and the external casing which is composed by a cylindrical endwall. The gap width can vary by approximately 0.15% under operating conditions.

Table 3.2 presents the operating conditions at design point of the turbine. These values have been implemented in the numerical simulation of the current work in order to achieve a high level of fidelity in the validation process. However, the injection flow and the associated cavities have not been considered for the sake of simplicity in the analysis. Therefore, any potential divergences during the validation process between experimental results and simulated data obtained may be attributed to this difference in approach. Nevertheless, each case of discrepancy is analyzed in detail on a case-by-case basis.

| **Parameter** | **Value** | **Units** |
|---|---|---|
| **Turbine** | | |
| Hub/Shroud radius | 330/400 | mm |
| Blade sequence | S1/R/S2 | - |
| Blade count | 36/54/36 | - |
| Absolute exit Mach | 0.52/0.26/0.48 | - |
| Reynolds number[1] | 7.1/3.8/5.1 $\times 10^5$ | - |
| **First stage** | | |
| Loading coefficient[2] $\psi = \frac{\Delta h}{u^2}$ | 2.34 | - |
| Flow coefficient[3] $\phi = \frac{c_x}{u}$ | 0.56 | - |
| Reaction degree | 0.39 | - |
| Total-to-total pressure ratio $\Pi_{tt,1stg}$ | 1.35 | - |

[1]Based on true chord and blade row relative exit velocity.
[2]$h$: enthalpy $[kJ/kg]$; $u$: rotational speed $[m/s]$.
[3]$c_x$: absolute axial flow velocity $[m/s]$.

**Table 3.1:** LISA-D 1.5-stage global geometry and performance parameters

| **Parameter** | **Value** | **Units** |
|---|---|---|
| Rotor speed | 2700±0.5 | RPM |
| Total-to-static pressure ratio $\Pi_{ts,1.5}$ | 1.65±0.2% | - |
| Shaft Power | 284[1] | kW |
| Inlet total temperature $T_{t,inlet}$ | 328.5±0.3 | K |
| Inlet total pressure $P_{t,inlet}$ | 1.4 | bar |
| Mass flow rate $\dot{m}_{main}$ | 11.60 | kg/s |
| Injection rate $IR = \frac{\dot{m}_{purge}}{\dot{m}_{main}} \times 100$ | 0.80±0.02% | % |

[1]Measured with a torque meter.

**Table 3.2:** LISA-D 1.5-stage design operational condition

| **Parameter** | **Hub** | **Midspan** | **Tip** | **Units** |
|---|---|---|---|---|
| | | **Stator 1** | | |
| Radius | 0.33 | 0.365 | 0.4 | m |
| Profile inlet angle | 0.0 | 0.0 | 0.0 | deg |
| Profile exit angle | 72.0 | 72.0 | 72.0 | deg |
| Turning angle | 72.0 | 72.0 | 72.0 | deg |
| Axial chord | 49.82 | 49.71 | 49.61 | mm |
| Chord length | 76.40 | 80.88 | 85.37 | mm |
| Pitch | 57.60 | 63.70 | 69.81 | mm |
| Aspect ratio | 0.92 | 0.87 | 0.82 | - |
| | | **Rotor** | | |
| Radius | 0.33 | 0.365 | 0.4 | m |
| Profile inlet angle | 60.9 | 52.4 | 40.7 | deg |
| Profile exit angle | -65.8 | -66.6 | -67.4 | deg |
| Turning angle | -126.7 | -119.0 | -108.1 | deg |
| Axial chord | 50.08 | 46.83 | 43.41 | mm |
| Chord length | 60.46 | 59.72 | 59.68 | mm |
| Pitch | 38.40 | 42.47 | 45.54 | mm |
| Aspect ratio | 1.16 | 1.17 | 1.17 | - |
| | | **Stator 2** | | |
| Radius | 0.33 | 0.365 | 0.4 | m |
| Profile inlet angle | -38.2 | -35.4 | -33.0 | deg |
| Profile exit angle | 66.0 | 66.0 | 66.0 | deg |
| Turning angle | 104.2 | 101.4 | 99.0 | deg |
| Axial chord | 71.98 | 72.04 | 72.16 | mm |
| Chord length | 82.42 | 85.50 | 89.48 | mm |
| Pitch | 57.60 | 63.70 | 69.81 | mm |
| Aspect ratio | 0.85 | 0.82 | 0.78 | - |

**Table 3.3:** LISA-D blades profiles geometry data

# Chapter 4

# Numerical methodology

In the following chapter, the numerical setup of the baseline flat tip simulation is outlined. Specifically, the presentation of the numerical methodology is structured according to the following steps:

- Governing equations and turbulence model;
- Definition of the computational domains;
- Domain setup and grid generation;
- Mesh independence study;
- Boundary conditions and initial setup;
- Solver settings and convergence criteria.

## 4.1 Introduction to numerical methodology

The numerical investigation of this study is conducted on a 1.5 stage axial turbine using the commercial software Ansys CFX 2021 R1 to solve the steady, viscous Reynolds Averaged Navier-Stokes (RANS) equations.

The computational grids for the domains are generated by utilizing Ansys Turbogrid 2021 R1 tool for meshing the two stators and the rotor blade body, while Ansys Meshing is employed for the creation of rotor tip grid as Turbogrid does not support complex tip geometries. Further details are provided below in Section 4.4 and Section 4.5.

Ansys CFX products are applied for post-mesh-generation stages. In particular, Ansys CFX-Pre is employed for defining domain interface interactions, as well as setting boundary and initial conditions. A detailed analysis of the choices and their motivations is provided in Section 4.6.

Additionally, Ansys CFX-Solver Manager is used for specifying solver and convergence settings (see Section 4.7), while Ansys CFX-Post is applied for results visualization and data handling.

## 4.2 Governing equations and turbulence models

Computational fluid dynamics (CFD) analysis is governed by a set of partial differential equations known as the Navier-Stokes (N-S) equations.

Firstly, unsteady differential Navier-Stokes equations in their conservation form and in a stationary frame are considered (Equation 4.1, Equation 4.2, Equation 4.3) as the foundational set of relations on which Ansys CFX-solver is based [40]. Following this, a concise description by steps on how the system of equation can be close is provided. Finally, the turbulence models are briefly discussed, with emphasis on the model used in this study.

- Conservation of mass (continuity):

$$\frac{\partial \rho}{\partial t} + \nabla \cdot (\rho \mathbf{U}) = 0 \tag{4.1}$$

- Conservation of momentum:

$$\frac{\partial (\rho \mathbf{U})}{\partial t} + \nabla \cdot (\rho \mathbf{U}\mathbf{U}) = -\nabla p + \nabla \cdot \tau + \mathbf{S}_M \tag{4.2}$$

- Conservation of total energy:

$$\frac{\partial (\rho h_{tot})}{\partial t} - \frac{\partial p}{\partial t} + \nabla \cdot (\rho \mathbf{U} h_{tot}) = \nabla \cdot (\lambda \nabla T) + \nabla \cdot (\mathbf{U} \cdot \tau) + \mathbf{U} \cdot \mathbf{S}_M + \mathbf{S}_E \tag{4.3}$$

Where:

- $\mathbf{U}$ is the velocity vector;
- $\boldsymbol{\tau} = \mu \left( \nabla \mathbf{U} + (\nabla \mathbf{U})^T - \frac{2}{3} \delta \nabla \cdot \mathbf{U} \right)$ is the stress tensor;
- $\mathbf{S}_M$ and $\mathbf{S}_E$ are, respectively, the momentum and the energy source;
- $h_{\text{tot}} = h + \frac{1}{2} U^2$ is the total enthalpy;
- $\lambda$ is the thermal conductivity of the fluid.

In order to close the equations system, two additional relations, for density and for enthalpy, are required. Assuming the fluid behaves as an ideal gas, the following two equations of state are applied:

- Ideal gas law:

$$\rho = \frac{M p_{\text{abs}}}{R_0 T} \tag{4.4}$$

- Enthalpy-temperature relations:

$$\mathrm{d}h = c_p \, \mathrm{d}T \qquad c_p = c_p(T) \tag{4.5}$$

Where:

- $M$ is the molecular mass of the gas;
- $p_{\text{abs}}$ and $T$ are respectively absolute static pressure and temperature;
- $R_0$ is the universal gas constant;
- $c_p$ is the specific heat capacity at constant pressure.

Other fluid models could be used to close the equations system, however, they are not discussed in this study since they are not implemented in the simulation solver setup. A similar consideration applies to the buoyancy model. Regarding momentum sources, no additional terms are selected for the analysis. However, the solver introduces new sources for flows where the frame of reference rotates at angular velocity $\omega$, which account for the effects of Coriolis force, centrifugal force, and angular acceleration.

$$\mathbf{S}_{M,\text{rot}} = \mathbf{S}_{\text{Cor}} + \mathbf{S}_{\text{cfg}} + S_{M,\dot{\omega}} \tag{4.6}$$

Where:

$$\mathbf{S}_{\text{Cor}} = -2\rho\,\omega \times \mathbf{U} \tag{4.7}$$

$$\mathbf{S}_{\text{cfg}} = -\rho\,\omega \times (\omega \times \mathbf{r}) \tag{4.8}$$

$$S_{M,\boldsymbol{\omega}} = -\rho \frac{\partial \omega}{\partial t} \times \mathbf{r} \tag{4.9}$$

Where:

- $\mathbf{r}$ is the location vector;
- $\mathbf{U}$ is the relative frame velocity.

Moreover, in this case, total enthalpy used for the advection and transient terms in Equation 4.3, is replaced with the rothalpy $I$ and an additional source of energy is required to account for the effects of angular acceleration.

$$I = h_{\text{stat}} + \frac{1}{2}U^2 - \frac{1}{2}\omega^2 R^2 \tag{4.10}$$

$$S_{E,\dot{\omega}} = -\rho\left[U \cdot \left(\frac{\partial \omega}{\partial t} \times r\right) + (\omega \times r) \cdot \left(\frac{\partial \omega}{\partial t} \times r\right)\right] \tag{4.11}$$

The resulting system of five equations could theoretically be implemented to resolve both laminar and turbulent flows. However, modeling turbulence with this approach, the Direct Numerical Simulation (DNS), required a computational cost many order of magnitude higher than another commonly implemented solving methods. This issue arises due to the extremely small scale dimensions generated by the turbulence, which are much finer than the smallest finite volume elements. To avoid enormous computational and power resources, which may be not even reachable, a variety of different statistic-based models has been developed.

The statistical turbulence models allow the flow to be represented by its average characteristics, with an additional time-varying, fluctuating component, expressed as $U_i = \bar{U}_i + u_i$. This approximation reflects directly on the original Navier-Stokes equations seen before by transforming them into the Reynolds Averaged Navier-Stokes equations, enabling the flow to be described using only mean flow quantities while omitting very small-scale behaviors. This approximation significantly reduces computational requirements compared to the DNS method. However, due to the new extra fluctuating quantities in the RANS equations, a higher number of unknown terms are introduced, which require additional relations to close the system. Consequently, the turbulence model utilized is defined by the extra equations implemented.

The derivation of the N-S equations into RANS equations is presented below.

- Conservation of mass (continuity):

$$\frac{\partial \rho}{\partial t} + \frac{\partial}{\partial x_j}\left(\rho U_j\right) = 0 \tag{4.12}$$

- Conservation of momentum:

$$\frac{\partial \rho U_i}{\partial t} + \frac{\partial}{\partial x_j}\left(\rho U_i U_j\right) = -\frac{\partial p}{\partial x_i} + \frac{\partial}{\partial x_j}\left(\tau_{ij} - \rho\overline{u_i u_j}\right) + S_M \tag{4.13}$$

- Conservation of total energy:

$$\frac{\partial \rho h_{tot}}{\partial t} - \frac{\partial p}{\partial t} + \frac{\partial}{\partial x_j}\left(\rho U_j h_{tot}\right) = \frac{\partial}{\partial x_j}\left(\lambda \frac{\partial T}{\partial x_j} - \rho\overline{u_j h}\right) + \frac{\partial}{\partial x_j}\left[U_l\left(\tau_{ij} - \rho\overline{u_i u_j}\right)\right] + S_E \tag{4.14}$$

Where:

- $\overline{u_i u_j}$ are the Reynolds stresses;
- $\overline{u_j h}$ are the additional turbulence flux term or Reynolds fluxes;
- $\frac{\partial}{\partial x_j}\left[U_l\left(\tau_{ij} - \rho\overline{u_i u_j}\right)\right]$ is the viscous work term;
- $h_{\text{tot}} = h + \frac{1}{2}U_i U_i + k$ is the mean total enthalpy and $k = \frac{1}{2}\overline{u_i}^2$ is a contribution from the turbulent kinetic energy.

The necessary relations to compute Reynolds stresses and flux terms define the turbulence model implemented to close the RANS equations. The models available in CFX are commonly categorized into two classes: eddy viscosity models and Reynolds stress models. A brief introduction to these two groups is provided, along with examples of commonly used models. However, a detailed description is given only for the k-epsilon turbulence model, as it is the method implemented in the present study.

### 4.2.1 Eddy viscosity models

These models are based on the assumption that turbulence consists of small eddies that are continuously forming and dissipating. The eddy viscosity hypothesis and the eddy diffusivity hypothesis are defined, assessing that Reynolds stresses and Reynolds fluxes are proportional, respectively, to the mean velocity gradients the first and to the mean scalar gradient the latter:

$$-\rho\overline{u_i u_j} = \mu_t\left(\frac{\partial U_i}{\partial x_j} + \frac{\partial U_j}{\partial x_i}\right) - \frac{2}{3}\delta_{ij}\left(\rho k + \mu_t\frac{\partial U_k}{\partial x_k}\right) \tag{4.15}$$

$$-\rho\overline{u_i h} = \Gamma_t\frac{\partial h}{\partial x_i} \tag{4.16}$$

Where:

- $\Gamma_t = \frac{\mu_t}{Pr_t}$ is the eddy diffusivity;
- $Pr_t$ is turbulent Prandtl number.

The turbulent fluctuations in the above equations can be represented as functions of the mean flow variables, but only if the turbulent viscosity $\mu_t$ is known.

The following models, implemented in CFX, use the same hypothesis:

- The zero equation model;
- The k-epsilon model;

- The k-omega models;
- The Shear Stress Transport (SST) model;
- The eddy viscosity transport model.

### 4.2.2 The k-epsilon turbulence model

The $k-\varepsilon$ turbulence model is part of the family of two-equation models, which includes the $k-\omega$ model, among others. These models are widely used thanks to their robustness and favorable balance between accuracy and computational effort. The nomenclature of this model family derives from the implementation of two equations used to estimate turbulence velocity scale and turbulent length scale.

The $k-\varepsilon$ model introduces two new variables into the system of equations: $k\left[\frac{m^2}{s^2}\right]$ is the turbulence kinetic energy, defined as the variance of the velocity fluctuations, while $\varepsilon\left[\frac{m^2}{s^3}\right]$ defines the turbulence eddy dissipation.

With this introduction, RANS equations are transformed as follows considering that the third equation, pertinent to the energy conservation, must be specified for the two new variables presented.

- Conservation of mass (continuity):

$$\frac{\partial \rho}{\partial t}+\frac{\partial}{\partial x_j}\left(\rho U_j\right)=0 \tag{4.17}$$

- Conservation of momentum:

$$\frac{\partial \rho U_i}{\partial t}+\frac{\partial}{\partial x_j}\left(\rho U_i U_j\right)=-\frac{\partial p'}{\partial x_i}+\frac{\partial}{\partial x_j}\left[\mu_{eff}\left(\frac{\partial U_i}{\partial x_j}+\frac{\partial U_j}{\partial x_i}\right)\right]+S_M \tag{4.18}$$

- Transport equation for the turbulence kinetic energy:

$$\frac{\partial\left(\rho k\right)}{\partial t}+\frac{\partial}{\partial x_j}\left(\rho U_j k\right)=\frac{\partial}{\partial x_j}\left[\left(\mu+\frac{\mu_t}{\sigma_k}\right)\frac{\partial k}{\partial x_j}\right]+P_k-\rho\varepsilon+P_{kb} \tag{4.19}$$

- Transport equation for the turbulence dissipation rate:

$$\begin{gathered}\frac{\partial\left(\rho\varepsilon\right)}{\partial t}+\frac{\partial}{\partial x_j}\left(\rho U_j \varepsilon\right)= \\ \frac{\partial}{\partial x_j}\left[\left(\mu+\frac{\mu_t}{\sigma_\varepsilon}\right)\frac{\partial \varepsilon}{\partial x_j}\right]+\frac{\varepsilon}{k}\left(C_{\varepsilon 1}P_k-C_{\varepsilon 2}\rho\varepsilon+C_{\varepsilon 1}P_{\varepsilon b}\right)\end{gathered} \tag{4.20}$$

Where:

- $S_M$ is the sum of body forces;
- $\mu_{eff} = \mu + \mu_t$ is the effective viscosity and $\mu_t = C_\mu \rho \frac{k^2}{\epsilon}$ with $C_\mu$ a constant;
- $p' = p + \frac{2}{3}\rho k + \frac{2}{3}\mu_{eff}\frac{\partial U_k}{\partial x_k}$ is the modified pressure;
- $P_k$ is the turbulence production due to viscous forces;
- $P_{kb}$ and $P_{\varepsilon b}$ represent the influence of the buoyancy forces;
- $C_{\varepsilon 1}, C_{\varepsilon 2}, \sigma_k$ and $\sigma_\varepsilon$ are constants.

For the purpose of this project, the work by Yang et al. [20] is considered as a reference. The researchers investigated different turbulence models in the contest of the flat tip gap case, assessing that no substantial differences in results quality were detected, although the over-prediction of experimental data with $k-\varepsilon$ method was less pronounced than with the other models tested. Consequently, $k-\varepsilon$ turbulence model is adopted for the purpose of the current study.

### 4.2.3 Reynolds stress turbulence models

The transport equations for all components of the Reynolds stress tensor and the dissipation rate, form the basis of these models. Without employing the eddy viscosity hypothesis, this group of models solves algebraic equations (Equation 4.21) for the Reynolds stresses in the case of Algebraic Reynolds stress models, while it solves differential transport equations (Equation 4.22) in the case of differential Reynolds stress models.

$$\begin{aligned}\frac{\partial \rho U_i}{\partial t} + \frac{\partial}{\partial x_j}\left(\rho U_i U_j\right) - \frac{\partial}{\partial x_j}\left[\mu\left(\frac{\partial U_i}{\partial x_j} + \frac{\partial U_j}{\partial x_i}\right)\right] = \\ -\frac{\partial p''}{\partial x_i} - \frac{\partial}{\partial x_j}\left(\rho\overline{u_i u_j}\right) + S_{M_i}\end{aligned} \tag{4.21}$$

$$\begin{aligned}\frac{\partial \rho\overline{u_i u_j}}{\partial t} + \frac{\partial}{\partial x_k}\left(U_k \rho\overline{u_i u_j}\right) - \frac{\partial}{\partial x_k}\left(\left(\delta_{jk}\mu + \rho C_S \frac{k}{\varepsilon}\overline{u_k u_l}\right)\frac{\partial \overline{u_i u_j}}{\partial x_j}\right) = \\ P_{ij} - \frac{2}{3}\delta_{ij}\rho\varepsilon + \Phi_{ij} + P_{ij,b}\end{aligned} \tag{4.22}$$

Where:

- $p'' = p + \frac{2}{3}\mu\frac{\partial U_k}{\partial x_k}$ is a modified pressure which has no turbulence contribution, unlike eddy viscosity models;
- $S_{M_i}$ is the sum of body forces and the fluctuating Reynolds stress contribution;

- $P_{ij}$ and $P_{ij,b}$ are shear and buoyancy turbulence production terms of the Reynolds stresses respectively;
- $\Phi_{ij}$ is the pressure-strain tensor;
- $C$ is a constant.

The following models are based on Reynolds stress turbulence method:

- The Reynolds stress model;
- The omega-based Reynolds stress models;
- The explicit algebraic Reynolds stress model.

## 4.3 Computational domains

Three different passage domains are defined based on the blisk sequence. The turbine is modeled in a single row, single pitch configuration.

Regarding the domain geometry, the axial distance between the trailing edge of the stator 1 and the leading edge of the rotor, as well as the distance between the trailing edge of the rotor and the leading edge of the stator 2, is maintained in accordance with the CAD model of the blades. This ensures that the relative positions of the turbine components are consistent with those in the experimental setup. The CFD data utilized for post-processing is extracted from planes within the domains that are precisely aligned with the experimental measurement planes. The inlet and the outlet of the entire computational domain are located further upstream and downstream of the leading of the stator 1 and the trailing edge of the stator 2, respectively, in order to avoid back-flow issues related to the boundary conditions of these surfaces.

Since number of blades in stators and rotor rows are not equal and the modeling employs a single pitch type, the interfaces between blade domains are not coincident; therefore, numerical interpolation is necessary between meshes.

Periodic interfaces are defined in circumferential direction of each blade row. The angle spanned by each domain is determined by the number of blades in the blisk. The stator domains cover an angle of $\frac{360^\circ}{36} = 10^\circ$ while the rotor domain spans an angle of $\frac{360^\circ}{54} \approx 6.67^\circ$.

Hub and shroud interfaces follow the CAD model surfaces for each blade domain and are positioned at radial distances of 330 $mm$ and 400 $mm$. Detailed properties of interfaces are discussed in Section 4.6.

The axial distances for inlet and outlet of the multi row computational domain are defined as a ratio of the axial chord of the relative blade as shown below:

$$\frac{L_{Inlet-LE,S1}}{c_{ax,S1}} = 0.25 \tag{4.23}$$

$$\frac{L_{TE,S2-Outlet}}{c_{ax,S2}} = 0.50 \tag{4.24}$$

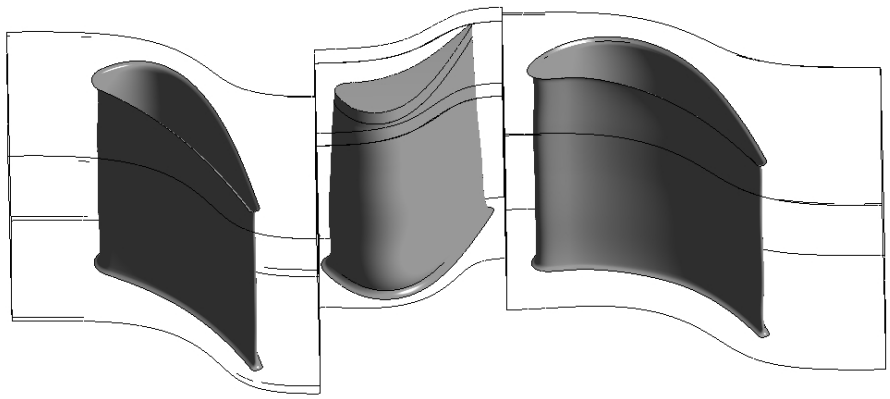

**Figure 4.1:** Wireframe of multirow computational domain and single blades

## 4.4 Mesh generation

As mentioned in the introduction section, two different Ansys tools are used for the discretization of the domain volumes.

Stator 1 and stator 2 passages are meshed using TurboGrid, along with the rotor blade body, which is included within 0% and 96.5% (corresponding to a radius of 395 $mm$) of the blade span. In contrast, the 5 $mm$ height tip volume is discretized with Ansys Meshing tool.

The meshing criteria used, which guides the grids definition, is the non-dimensional wall distance, commonly called $y^+$ value, which is defined as:

$$y^+ = \frac{y \cdot u_T}{\nu} \tag{4.25}$$

Where:

- y is the distance between wall and first element node;
- $u_T = \sqrt{\frac{\tau_w}{\rho}}$ is the friction velocity of the stream;
- $\tau_w = \frac{1}{2} \cdot \rho \cdot U^2_{freestream} \cdot C_f$ is the wall shear stress;

- $\nu = \frac{\rho}{\mu}$ is the cinematic viscosity while $\rho$ is the fluid density and $\mu$ the dynamic viscosity.

The skin friction coefficient $C_f$ for a turbulent boundary layer can be approximated by different formulations depending on flow conditions. The Prandtl's relation, given by $C_f = 0.074 Re_x^{-1/5}$, or the more complex Schlichting's relation, $C_f = [2\log_{10}(Re_x) - 0.65]^{-2.3}$, are commonly implemented in studies similar to the current study [41].

Considering Equation 4.25, the $y^+$ value is used to correlate the fluid characteristics with the first layer thickness required to accurately resolve the boundary layer near walls.

As described in the Ansys TurboGrid User's Guide [42], the formula implemented by the software is different from Equation 4.25 because it directly relates the near wall spacing $\Delta y$ to the Reynolds number $Re_L$ of the fluid flow in the following manner:

$$\Delta y = L \cdot \Delta y^+ \cdot \sqrt{80} \cdot Re_x^{1/14} \cdot \frac{1}{Re_L} \tag{4.26}$$

Where:

- L is the blade chord;
- $Re_x$ is the Reynolds number based on the distance along the chord (measured from the leading edge); by default the software sets it equal to $Re_L$;
- $Re_L$ is the Reynolds number based on chord length.

For all domains, $y^+$ target value is set to 1 near blade walls and 10 in proximity of hub and shroud surfaces. Using the Equation 4.25 and data in Table 3.1 and Table 3.3, this results in a first wall distance of $\approx 5 \cdot 10^{-6}\ mm$ near blades and of $\approx 5 \cdot 10^{-5}\ mm$ near hubs and shrouds.

For the stator and the rotor bodies, hexahedral elements are selected to build structured meshes. Moreover, a constant first element offset is considered, allowing the mesher to create a double-sided node distribution in the boundary layer instead of a single-side distribution, avoiding a constant expansion rate. In the spanwise direction, nodes distribution is set to be uniform with around 50 elements close to midspan and 25 elements each on the hub and the shroud sides to satisfy inflation requirements.

For the rotor tip volume, an unstructured mesh with tetrahedral elements is preferred due to the complex tip geometry. The number of nodes is determined to be proportional to the rotor body grid size, following the ratio between the blade tip surface area and the total rotor blade surface area. As a result, a target number of nodes equal to 11% of the total nodes required by rotor domain is considered.

Table 4.1 summarizes the most important characteristics of domain meshes.

The optimal number of nodes for the numerical study is determined through the grid independence study described in the following section.

| Domain | Part | Elements | y+ Blade | y+ H. & S. |
|---|---|---|---|---|
| Stator 1 | Stator 1 | hexahedral | 1 | 10 |
| Rotor | R1 Body | hexahedral | 1 | 10 |
| | R1 Tip | tetrahedral | 1 | 10 |
| Stator 2 | Stator 2 | hexahedral | 1 | 10 |

**Table 4.1:** Main meshes features for each domain

## 4.5 Grid independence study

A grid independence study is conducted to obtain an initial estimate of the minimum number of nodes required for the simulation. This process allows for the optimization of time effort and computational cost required, by analyzing the stability and reliability of the results.

Simulations with different total node counts are tested, while keeping the node distribution constant across domains within the same simulation. Mesh features, as well as working conditions, remain unmodified between the analyzed cases. Table 4.2 shows the simulations tested along with the respective node counts (rounded).

In Figure 4.2 to Figure 4.4, the resulting curves for different relevant output parameters are plotted. Based on these charts, a total number of nodes between 5 and 6 Million appears appropriate as an initial configuration for the current study.

| Simulation | N. S1 | N. R | N. S2 | N. total |
|---|---|---|---|---|
| Case 1 | 500k | 500k | 500k | 1.5M |
| Case 2 | 1M | 1M | 1M | 3M |
| Case 3 | 1.5M | 1.5M | 1.5M | 4.5M |
| Case 4 | 2M | 2M | 2M | 6M |

**Table 4.2:** Test cases for mesh independence study

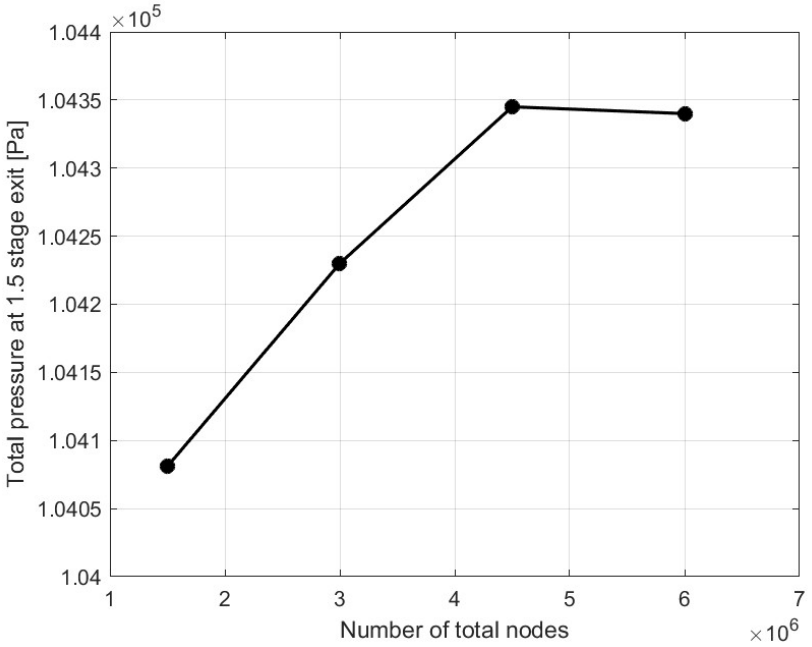


**Figure 4.2:** Total pressure at the 1.5-stage turbine exit for different simulations

## 4.6 Boundary conditions and initial setup

To numerically solve the partial differential RANS equations, the system requires initial and boundary conditions specification of the computational domain. Given the geometry and the set of mathematical relations used to resolve the flow field, this additional set of conditions is critical in achieving accurate results. With this in mind, the conditions must be defined as precisely as possible to correctly reflect the real situation under study. [40] and [43] are considered in this section as theoretical reference.

### 4.6.1 Inlet and outlet boundary conditions

A subsonic inlet condition is specified at the entrance of the multi-row computational domain, with direction of flow velocity normal to the boundary and constant in magnitude. The condition is defined by the total pressure value, selected for its robustness [43]. Based on this value, CFX-Solver computes the static pressure needed to properly satisfy the boundary condition.

Turbulence intensity $I = \frac{u}{U}$ is set to a medium level (5%) with a viscosity ratio $\frac{\mu}{\mu_t}$ equal to 10. The parameters $k$ and $\varepsilon$ are calculated using expressions that scale

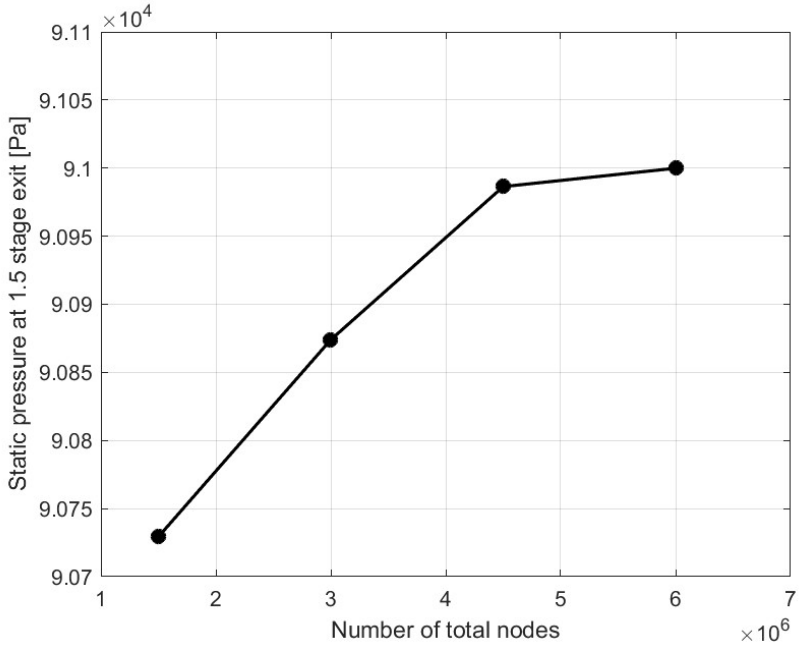


**Figure 4.3:** Static pressure at the 1.5-stage turbine exit for different simulations

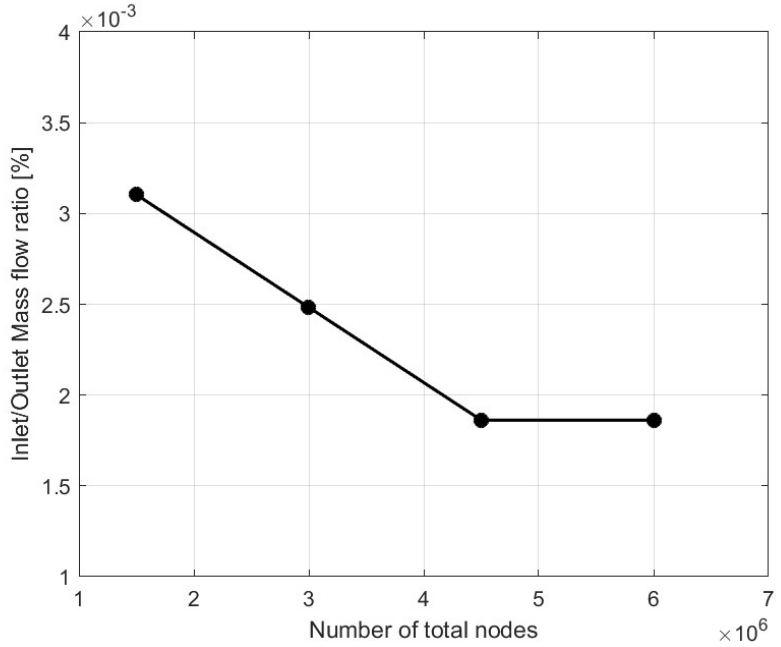


**Figure 4.4:** Mass flow inlet/outlet error of the 1.5-stage turbine for different simulations

their inlet distribution based on value $I$:

$$k_{inlet} = \frac{3}{2} \cdot I^2 \cdot U^2 \tag{4.27}$$

$$\varepsilon_{inlet} = \rho C_\mu \frac{k^2}{\mu_t} \tag{4.28}$$

Where:

- $\mu_t = CI\mu$;
- C is the turbulence intensity factor at the boundary condition. The default value of $C$ is 1000.

Heat transfer is defined using the total temperature $T_{tot,inlet}$ value.

Consequently, the following relations are implemented to calculate the inlet energy flow $Q_{inlet} = Q_{advec} - Q_{diffus}$ across the boundary utilizing a thermodynamic relationship for enthalpy $h = h(p, T)$, which depends on the properties of the fluid:

$$T_{stat,inlet} = T_{tot,inlet} - \frac{U^2}{2C_p} \tag{4.29}$$

$$h_{tot} = h_{stat} + \frac{1}{2} \cdot U^2 \tag{4.30}$$

$$Q_{advec} = h_{tot} \cdot \dot{m} \tag{4.31}$$

The diffusion contribute $Q_{diffus}$ to the total energy is considered negligible compared to advection term.

A subsonic outlet condition is defined at the exit of the multi-row computational domain. The boundary condition is specified by setting the total mass flow rate, $\dot{m}_{spec}$, for all sectors, guaranteeing consistency with inlet boundary specification [43]. The mass flux distribution across the outlet is calculated by the solver iteratively, adjusting the computed value $\dot{m}_{ip}$ with the boundary value using a correction factor $F$. The process works as follows:

$$\dot{m}_{ip} = \rho_{ip} \cdot A_{ip} \cdot U_{ip} \tag{4.32}$$

The solver calculates the total mass flow based on the computed value and generates the correction factor:

$$\dot{m}_{tot}^{est} = \sum_{all} \dot{m}_{ip} \tag{4.33}$$

$$F = \frac{\dot{m}_{spec}}{\dot{m}_{tot}^{est}} \tag{4.34}$$

The correction is applied to Equation 4.32 to restart the iterative cycle:

$$\dot{m}_{ip} = F \cdot \rho_{ip} \cdot A_{ip} \cdot U_{ip} \tag{4.35}$$

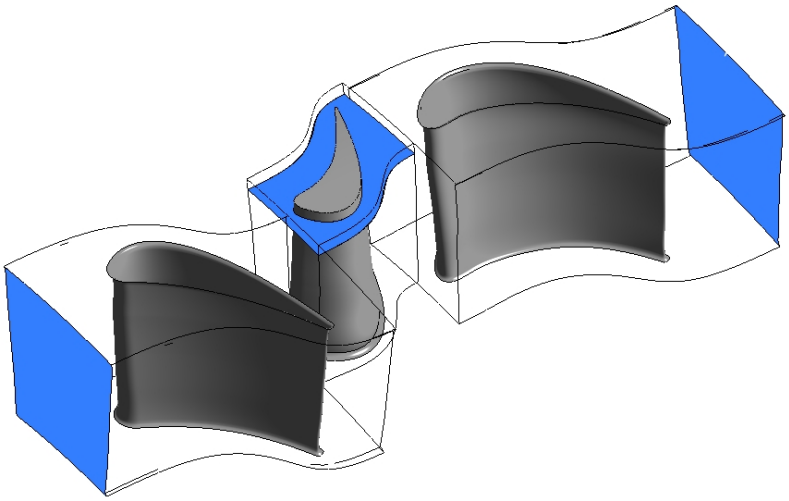

**Figure 4.5:** Inlet and outlet interfaces plus rotor body-tip interface

### 4.6.2 Wall boundary conditions

Walls are treated as impermeable boundaries to fluid flow. A no-slip wall condition is applied to all the physical surfaces of the three blade rows which contain the flow stream, including the blade areas, hub, and shroud planes. With this condition, the fluid immediately next to the wall assumes the velocity of the wall, which is zero by default.

For the stator walls, no velocity is required, hence $U_{wall} = 0$. In contrast, for the rotor walls, rotational velocity is necessary and therefore, the hub and blade surfaces are set to $U_{wall} = \omega \cdot R$, while the shroud surface is defined as a counter-rotating wall with $U_{wall} = -\omega \cdot R$

Furthermore, all walls are assumed to be adiabatic, meaning that no heat flux crosses the boundary.

### 4.6.3 Periodicity and domain interfaces

In the current study, the entire computational flow field is divided into three different domains corresponding to the three turbine blisks.

Single row, single pitch domains are used, allowing for a considerable reduction in the computational effort required to perform the simulation. This simplification is possible thanks to the rotational symmetry of the problem. Nevertheless, it is essential to note that, with this approximation, no transverse flow phenomena are detected, despite the fact that the turbine flow field exiting the combustion chamber is highly three-dimensional. For this reason, any discrepancies between

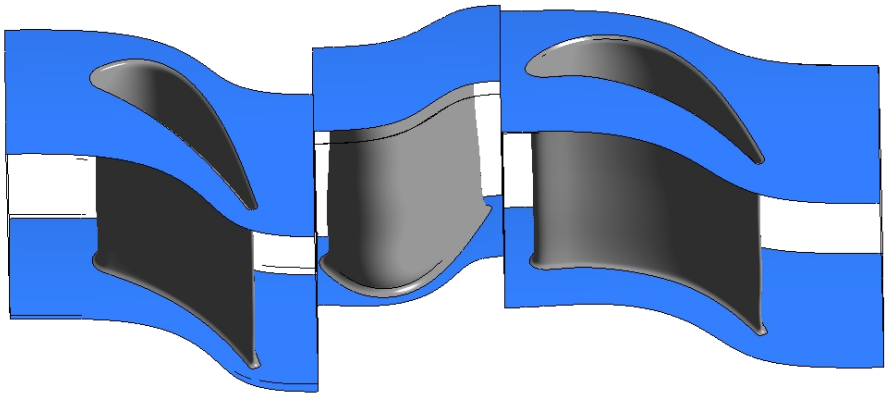

**Figure 4.6:** Hub and shroud walls of the three domains

experimental and numerical results during validation process may be attributed to this limitation. In order to implement single-blade domains, rotating periodic interfaces are set in the circumferential direction. The connection is managed by the General Grid Interface (GGI) mesh connection.

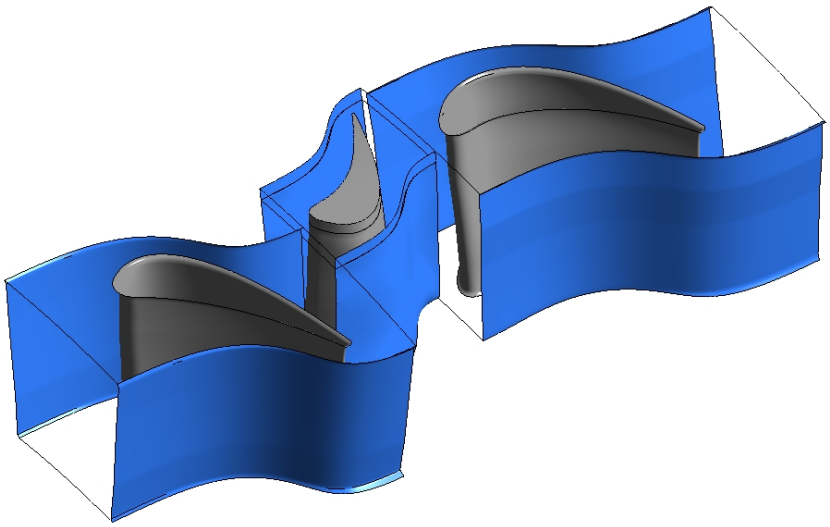

**Figure 4.7:** Periodic interfaces of the three domains

Regarding the interaction between stator 1 and rotor, as well as between rotor and stator 2, fluid-fluid general connection models are implemented. The Mixing Plane

(MP) model is employed in conjunction with the GGI for grids connectivity. The MP model performs a circumferential averaging of the fluxes through segments at the interface. The average static pressure within each band on both the upstream and downstream side of the interface is set to the average band pressure while, regarding the velocity, it is calculated based on the average band total pressure and direction in the relative frame. The pitch change between the interfaces is set to automatic. The flow angle adjustment is achieved by applying average values calculated from the upstream side of the interface to the downstream side. Variations are maintained in the meridional direction while they are removed, except pressure, if in the circumferential direction.

The interface, within the rotor domain, between body and tip meshes is considered differently from the others as no relative rotating movement exists. It is set as a fluid-fluid general connection with a frozen rotor-type mixing model. This approach allows the two mesh to connect by fixing the relative position throughout the calculation. The data exchange across the interface is achieved by directly transferring velocity, pressure, and other variables without any averaging. Moreover, pitch angle values for both sides of the interface are set to be equal to 6.67° since the circumferential distance covered is the same for both.

### 4.6.4 Initial conditions

The initial variable values are essential for providing the software solver with a flow field from which to start its calculations. Considering the steady-state nature of the study, automatic initial conditions are selected. Additionally, turbulence intensity is set to a medium level of 5%.

The automatic initialization feature provided by Ansys CFX estimates uniform values across the domain based on the boundary conditions, providing a balanced and neutral starting point for the simulation. This approach reduces the need for manual intervention while being adequate for a steady-state analysis, where the flow field reaches equilibrium over time. Moreover, the solver can approach a stable solution without slowdowns caused by overly specific or complex initial guesses, which could potentially introduce convergence issues.

## 4.7 Solver settings and convergence criteria

Although the introduction of the techniques and models discussed in Section 4.2 allows for the closure of the Navier-Stokes equations system, analytical solutions exist only for flows under significant simplifications in ideal conditions. To obtain solutions for real flows, a numerical approach must be adopted, which involves

replacing the partial differential equations with algebraic approximations that can be solved using numerical methods.

### 4.7.1 Solver methodology

Ansys CFX employs an element-based finite volume method, that begins with the mesh definition, which is subsequently used to construct finite volumes [40]. The conservation equations are integrated over each control volume, ensuring the conservation of relevant quantities such as mass, momentum, and energy. Solution fields and other properties are stored at the mesh nodes. However, to evaluate many of the terms, the solution field or its gradients must be approximated at integration points. Finite-element shape functions are used to perform these approximations as follows:

$$\varphi = \sum_{i=1}^{N_{\text{nodes}}} N_i \varphi_i \tag{4.36}$$

Where:

- $N_i$ is the shape function for node $i$;
- $\varphi_i$ is the value of the variable $\varphi$ at node $i$.

The shape functions used in Ansys CFX are linear in terms of parametric coordinates.

Moving forward in the resolution process, the High Resolution (HR) discretization scheme is employed by Ansys [40]. This scheme is based on the first-order upwind method, to which an advection term is added to achieve second-order accuracy. The general formula is here presented:

$$\varphi_{ip} = \varphi_{up} + \beta \nabla\varphi \cdot \Delta\vec{r} \tag{4.37}$$

Where:

- $\varphi_{up}$ is the value at the upwind node;
- $\vec{r}$ is the vector from the upwind node to the $ip$;
- $\beta, \nabla\varphi$ are the parameters yield by the High Resolution scheme.

The quantity $\beta\nabla\varphi \cdot \Delta\vec{r}$ is referred to as the Numerical Advection Correction and is considered as an anti-diffusive correction applied to the upwind scheme. The choice $\beta = 1$ formally corresponds to a second-order accuracy in space, allowing for a more precise reproduction of steep spatial gradients compared to the first-order base scheme. The HR scheme uses a specialized non linear function for $\beta$ at each

node, which is computed to be as close to 1 as possible without introducing new extrema.

Regarding the solution strategy, Pressure-Velocity Coupling algorithm is implemented. This algorithm allows for the simultaneous solution of pressure and velocity component equations as a single system, rather than sequentially (non-coupled). This approach offers advantages in robustness, efficiency, generality, and simplicity. The principal drawback is the high storage space needed for all the coefficients. The discrete system of linearized equations is solved by Ansys CFX using a Multigrid (MG) accelerated Incomplete Lower Upper (ILU) factorization technique. This iterative solver progressively approaches the solution through multiple iterations. The linearized system of discrete equations in matrix form can be presented as:

$$[A][\varphi] = [b] \tag{4.38}$$

Where:

- $[A]$ is the coefficient matrix;
- $[\varphi]$ is the solution vector;
- $[b]$ is the right hand side of the matrix system.

The solution process is iterative, starting from a solution approximation $\varphi^n$ that is corrected by $\varphi'$ to lead to a better solution $\varphi^{n+1} = \varphi^n + \varphi'$. In the process, $\varphi'$ is calculated by $A\varphi' = r^n$ and the residuals are obtained by $r^n = b - A\varphi^n$.

### 4.7.2 Time step and convergence

An appropriate time step size is essential for achieving good convergence rates in the simulation. In case of steady-state analysis, a false time step is used by Ansys CFX as a means of under-relaxing the equations as they iterate towards the final solution. In general, large time scales facilitate faster convergence, however, if it is too large, the solution may exhibit fluctuations without converging. On the other hand, excessive small time steps risk to slow down the simulation significantly. For the current study, a conservative, automatic time scale with a factor of 1.0 is selected. The automatic time scale is based on the solver adaptation of the time steps based on problem length scales, calculated from the mesh and geometric configuration of the flow domain, and velocities scales which are derived from the local flow velocities. The solver dynamically adjusts this time scale throughout the simulation to maintain numerical stability and ensure that the time step is appropriate for properly resolving the flow [43].

Convergence is monitored using normalized residuals, which quantify the local imbalance of each conservative control volume equation. Residuals serve as a

crucial measure of convergence, as they relate directly to the solution accuracy of the solved equations. Root Mean Square (RMS) residuals type are automatically checked by the solver by comparison with the specified target value [43]. The normalized residual value for the solution variable $\varphi$ is defined as follows:

$$[\tilde{r}_\varphi] = \frac{[r_\varphi]}{a_p \Delta\varphi} \tag{4.39}$$

Where:

- $r_\varphi$ is the raw residual control volume imbalance;
- $a_p$ and $\Delta\varphi$ are respectively a representative of the control volume coefficient and a representative range of the variable in the domain.

For the purpose of this study, an RMS residual target of $10^-3$, with a maximum iterations number equal to 300, is considered. All simulations run for this project successfully reach the residual target before reaching the maximum number of iterations, nevertheless, results are evaluated after 300 cycles to ensure consistency and facilitate easier comparisons. The computational simulations were performed on a machine equipped with an Intel(R) Core(TM) i5-8400 CPU running at 2.80 GHz. The processor has 6 cores and operates on a single socket. The system is supported by 16 GB of RAM, which provides sufficient memory to handle the medium-sized mesh and computational requirements of the CFD analysis. Because of the modest hardware resources, compared to high-performance computing clusters, particular attention is given to the computational cost associated with the analyzed problem.

Table 4.3 presents the amount of time taken by the simulations considered for the mesh independence study.

| **Simulation** | **Case 1** | **Case 2** | **Case 3** | **Case 4** |
|---|---|---|---|---|
| **Tot. Nodes** | 1.5M | 3M | 4.5M | 6M |
| **Time effort [h.min]** | 2 | 3.30 | 5.30 | 7.30 |

**Table 4.3:** Computational time taken by mesh independence study tests

# Chapter 5

# Validation process

In this chapter, the validation process is presented. A series of simulations is analyzed to examine which domain discretization configuration produces steady-state results that most closely emulate the experimental data. Various meshing strategies are tested, with close attention given to the sensitivity of the solution to mesh refinement.

## 5.1 Process definition

The modifications introduced in the simulations are mainly related to the grid configurations of the computational domains. Besides the alignment of LISA-D turbine provided measurements, the process focuses on the reduction of computational time and numerical effort required. This is considered an issue of high relevance for this work, as the tip recess study, explained in Chapter 6, requires necessarily a considerable number of tests and the computational resources available for the entire project are limited, as presented in Chapter 4.

The primary objectives of this validation process, prioritized by importance, are here listed:

- Validating pressures, temperatures, and velocity at the first-stage exit;
- Achieving reasonable predictions of first-stage efficiency and power extracted;
- Minimizing time effort and computational cost.

A comprehensive collection of experimental results have been published by the ETH Zurich related to the LISA-D turbine. Among these, Area-Averaged (AAV) flow measurement profiles in Stationary Frame of Reference (SFR) are considered in this study for the validation process.

Two sets of spanwise data are analyzed, corresponding to the measurements planes described in Chapter 3: one positioned downstream of the stator 1 and the other downstream of the rotor. Although both measurements sets of results are used for the validation, the rotor exit plane data are referenced more extensively during the process to assess first-stage performance.

The following flow parameters are evaluated:

- Total and static pressure in SFR;
- Mach number in SFR;
- Total and static temperature in SFR;
- Total-to-total first stage efficiency, both isentropic and polytropic.
- First stage extracted power.

The data from the measurement probes FRAP-4S-3 $mm$ are considered for the validation, chosen over the larger 4 $mm$ and 5 $mm$ tip diameter sensors. The choice can be justified by the following key factors. Primarily, smaller probes introduce minimal changes within the flow field, in terms of distortions and disturbances, resulting in measurements that more accurately reflect the true flow dynamics of the problem analyzed. Furthermore, the higher spatial resolution of thinner probes can better capture rapid and local variations in velocity and pressure, which is crucial for reliable and realistic data. Overall, 3 $mm$ probes are preferable in order to obtain measurements which are more accurate and representative as they provide an optimal balance of precision, minimal flow interference and robust data quality compared to other sensors options available for this study.

The AAV measurements of the three probe types, for both stator 1 exit plane and rotor exit plane, are shown in figures from 5.1 to 5.5. The results indicate no substantial differences in the measured curves across the probes. Consequently, for the purposes of this study, each sensor is theoretically suitable for capturing the required data.

The validation process involves examining the spanwise simulation curves of the specified flow quantities and calculating the extrapolated efficiency values. Percentage errors, for both flow quantities and efficiency, are calculated to quantify the discrepancies between the experimental and the CFD results and to compare the accuracy of different computational grid strategies.

Since the blade portion covered by the measurement planes, see Chapter 3, is limited in radial direction to a specific sector, while CFD results span the entire blade length, it is necessary to interpolate the CFD data to match the radial positions of the experimental measurement points. Subsequently, the percentage

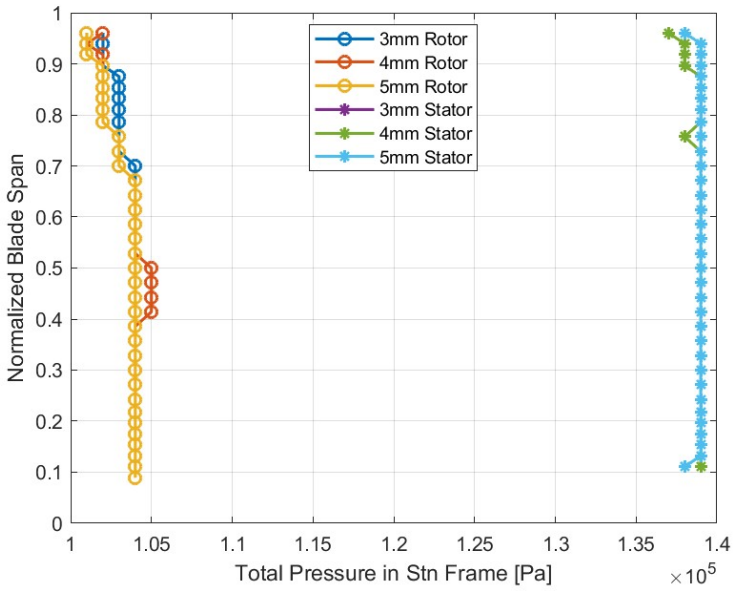


**Figure 5.1:** Total pressure measurements from LISA-D stator 1 exit and rotor exit for the 3, 4 and 5 *mm* FRAP-4S probes

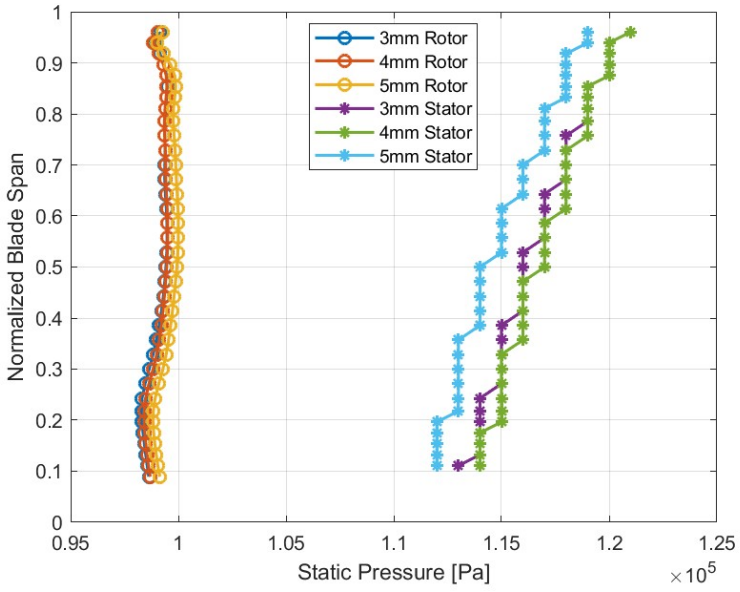


**Figure 5.2:** Static pressure measurements from LISA-D stator 1 exit and rotor exit for the 3, 4 and 5 *mm* FRAP-4S probes

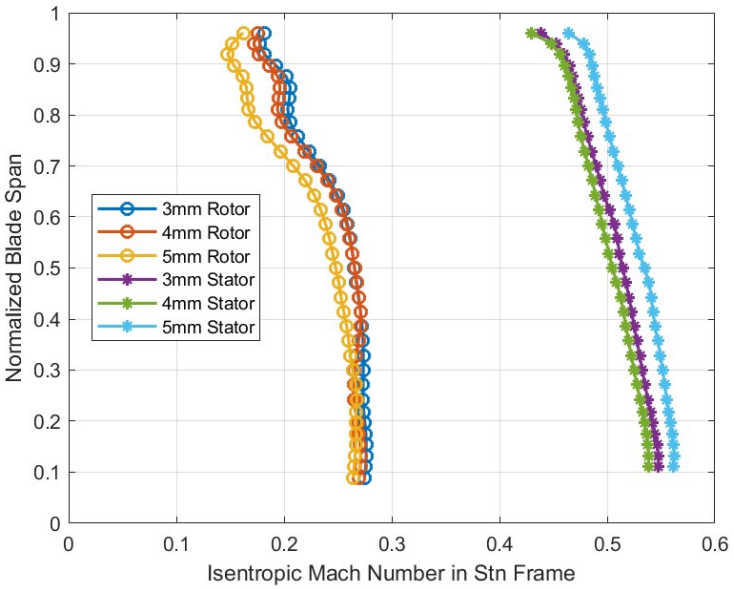


**Figure 5.3:** Mach number measurements from LISA-D stator 1 exit and rotor exit for the 3, 4 and 5 *mm* FRAP-4S probes

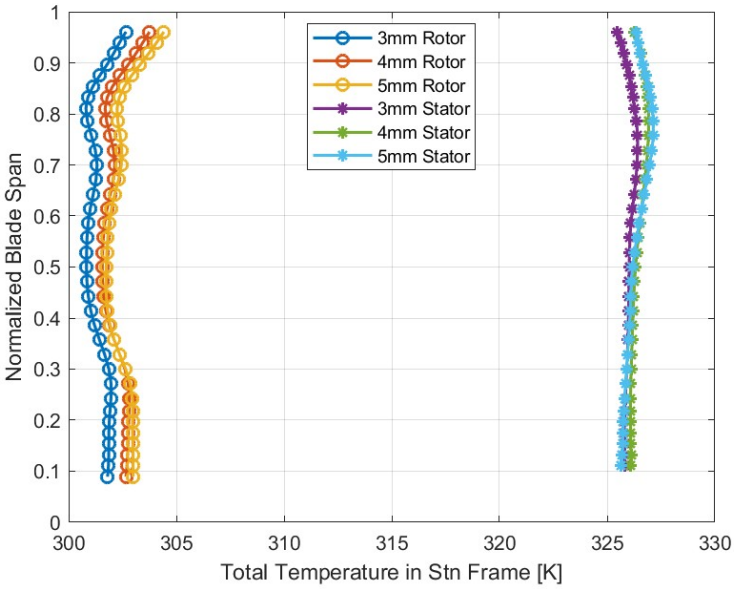


**Figure 5.4:** Total temperature measurements from LISA-D stator 1 exit and rotor exit for the 3, 4 and 5 *mm* FRAP-4S probes

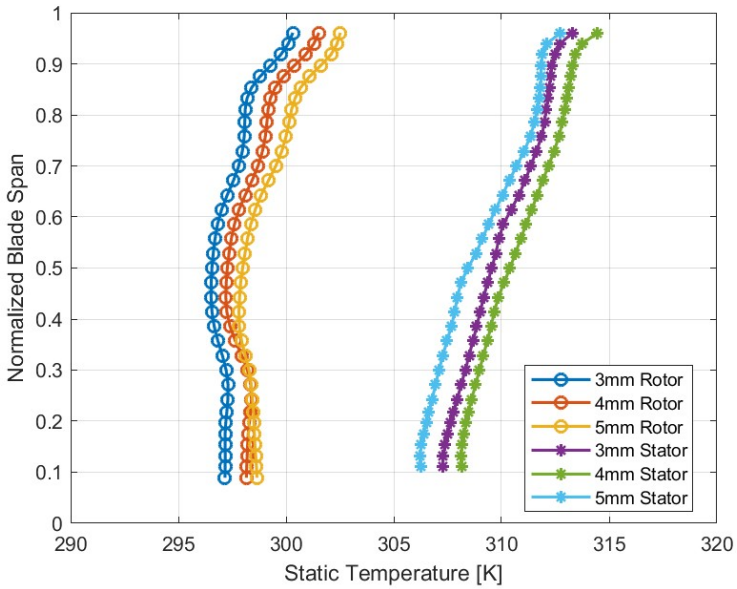


**Figure 5.5:** Static temperature measurements from LISA-D stator 1 exit and rotor exit for the 3, 4 and 5 *mm* FRAP-4S probes

error of a given quantity $\varphi$ for each point position $x$ is calculated, resulting in an error distribution curve.

$$Err_{\varphi_x} = \frac{|\varphi_{exp} - \varphi_{cfd}|}{\varphi_{exp}} \cdot 100 \tag{5.1}$$

Starting from the equation mentioned above, the arithmetic mean of error curves is calculated for an easier and faster comparison of the simulations. However, it is important to acknowledge that this approach may obscure local singular behaviors.

Regarding performance, both total-to-total isentropic and polytropic efficiencies are calculated. Knowing the total power extracted $P$ and the main flow mass rate $\dot{m}$, $\mu_{TT_{\text{isen}}}$ is obtained by taking the ratio between the actual and the ideal enthalpy extracted:

$$\mu_{TT_{\text{isen}}} = \frac{P/\dot{m}}{C_p \cdot T_{\text{tot,in}} \left(1 - \left(\frac{P_{\text{tot,out}}}{P_{\text{tot,in}}}\right)^{\frac{\gamma-1}{\gamma}}\right)} \tag{5.2}$$

For the polytropic case, the following relationship, derived from thermodynamic theory, is well established:

$$\frac{n-1}{n} = \mu_{poly} \cdot \frac{\gamma - 1}{\gamma} \tag{5.3}$$

Where:

- $\gamma$ is the adiabatic expansion coefficient;
- $n$ is the polytropic index.

Equation 5.2 can be rewritten showing the enthalpy extraction instead of the power.

$$\mu_{TT_{\text{isen}}} = \frac{1 - \frac{T_{\text{tot,out}}}{T_{\text{tot,in}}}}{1 - \left(\frac{P_{\text{tot,out}}}{P_{\text{tot,in}}}\right)^{\frac{\gamma-1}{\gamma}}} \tag{5.4}$$

Moreover, the general relation for a polytropic transformation need to be considered:

$$\frac{T_{\text{tot,out}}}{T_{\text{tot,in}}} = \frac{p_{\text{tot,out}}}{p_{\text{tot,in}}}^{\frac{n-1}{n}} \tag{5.5}$$

Combining Equation 5.3, Equation 5.4 and Equation 5.5, the relation between the two efficiencies can be obtained:

$$\mu_{TT_{\text{isen}}} = \frac{1 - \frac{T_{\text{tot,out}}}{T_{\text{tot,in}}}}{1 - \left(\frac{T_{\text{tot,out}}}{T_{\text{tot,in}}}\right)^{\frac{1}{\eta_{TT_{poly}}}}} \tag{5.6}$$

Which can be rearranged to isolate the total-to-total polytropic efficiency to the left side.

$$\mu_{TT_{\text{poly}}} = \frac{\log\left(\frac{T_{\text{tot,out}}}{T_{\text{tot,in}}}\right)}{\log\left(1 - \frac{1-\frac{T_{\text{tot,out}}}{T_{\text{tot,in}}}}{\mu_{TT_{\text{isen}}}}\right)} \tag{5.7}$$

Equation 5.2 and Equation 5.7 are the relations implemented in the validation process.

## 5.2 Baseline case

To establish a preliminary set of results for the validation process, the simulation with 6 million nodes from the mesh independence study is analyzed, as similar number of total node count was found to be necessary to balance computational effort and accuracy.

Figure 5.6 to Figure 5.10 illustrate the spanwise results at the exit of stator 1. For each quantity evaluated, both the actual values and percentage errors are presented. A high degree of accuracy of numerical results on experimental measurements behaviors is detected. The data trends are generally well captured. Average errors under 1% are obtained for three out of five quantities while static pressure is slightly higher and Mach number reaches a mean deviation of nearly 3.5% with the highest

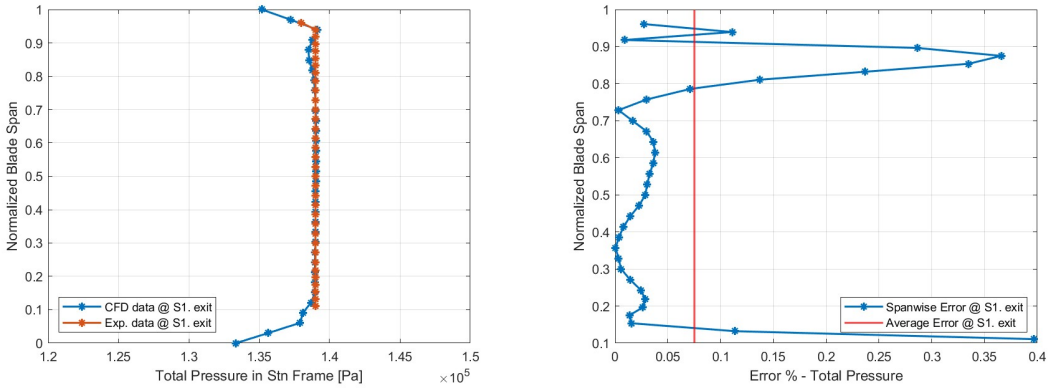


**Figure 5.6:** Tot. pressure values and errors at stator 1 exit plane, case 1

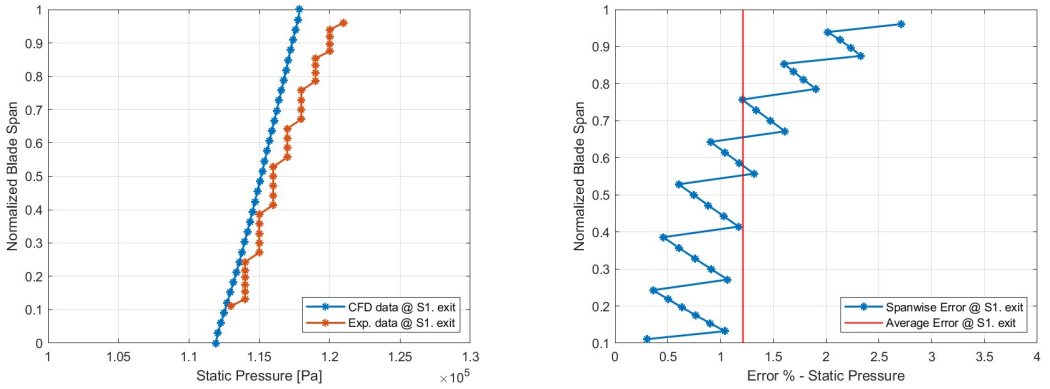


**Figure 5.7:** Stat. pressure values and errors at stator 1 exit plane, case 1

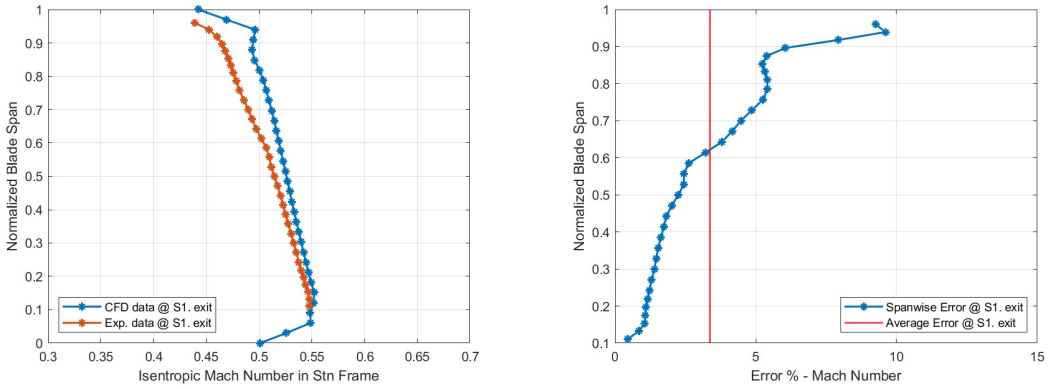


**Figure 5.8:** Mach number values and errors at stator 1 exit plane, case 1

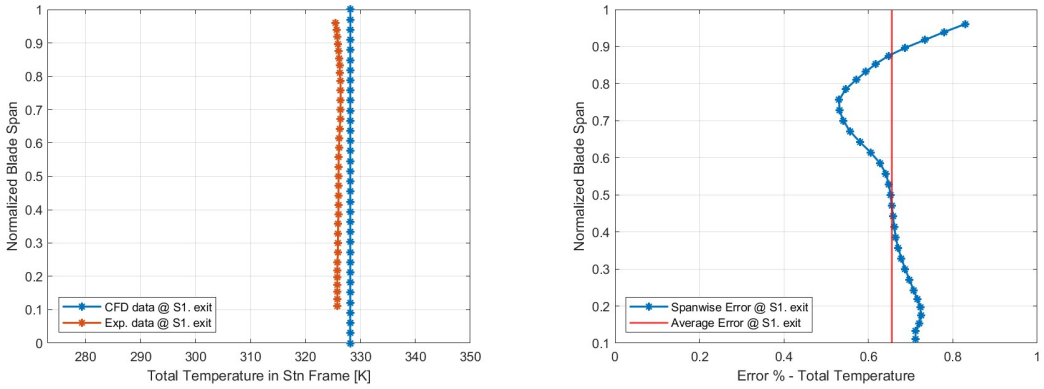


**Figure 5.9:** Tot. temperature values and errors at stator 1 exit plane, case 1

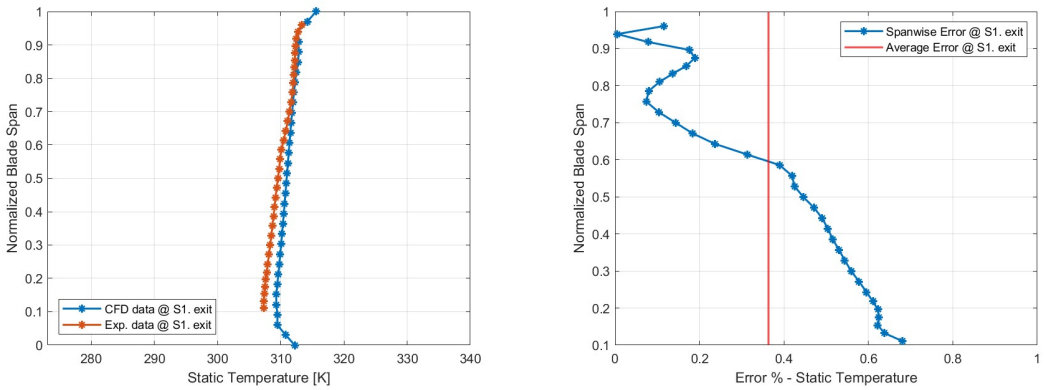


**Figure 5.10:** Stat. temperature values and error at stator 1 exit plane, case 1

error values encountered going closer to shroud. A similar pattern, although with smaller impact, can be observed analyzing the static pressure graph.

The rotor exit results are presented in Figure 5.11 to Figure 5.15. Similar to the stator exit results, both measurements and their corresponding percentage errors are shown. While the average differences are slightly higher than the stator results, four out of five quantities reveal mean errors between 1% and 2.2%. As noted in the upstream analysis, the Mach number displays the highest deviation, with an average error around 7.5%. Nearly constant discrepancies are observed close to the blade's midspan, while the most significant error fluctuations occur from approximately 70% of the blade span toward the shroud. This pattern highlights the increased instability closer to the tip region, which can be attributed to the presence of the tip gap, and the challenges associated with accurately simulating this area.

Regarding the results presented on Figure 5.6 to Figure 5.15, an overall favorable trend is observed for all quantities analyzed. Using this configuration, the following efficiency and power deviations are calculated:

- Total-to-total isentropic efficiency error: 0.81%
- Total-to-total polytropic efficiency error: 0.91%
- Extracted power error: 4.11%

These trends in the data curves, along with the efficiency and power discrepancies observed, are considered a solid foundation for the next steps of the validation process. In these subsequent steps, the computational grid is modified iteratively to reduce curve discrepancies wherever possible, aiming to minimize measurement curve differences and further optimize computational time requirements.

## 5.3 Sequential steps

The simulation cases outlined in Table 5.1 are analyzed. The process sequence is conducted by gradually reducing the amount of nodes for each domain.

Six different configurations are evaluated. As further explained in the related paragraphs, the validation process focuses, in parallel, on refining the rotor domain grid, especially within the blade tip region, and on reducing the nodes of stator meshes to reduce the computational cost.

The following modifications are applied to each of the cases:

**Case 1** This configuration serves as a starting point of the validation process, directly derived from the mesh independence study as baseline case for subsequent simulations. Further details, as well as resulting measurements, are provided in Section 5.2.

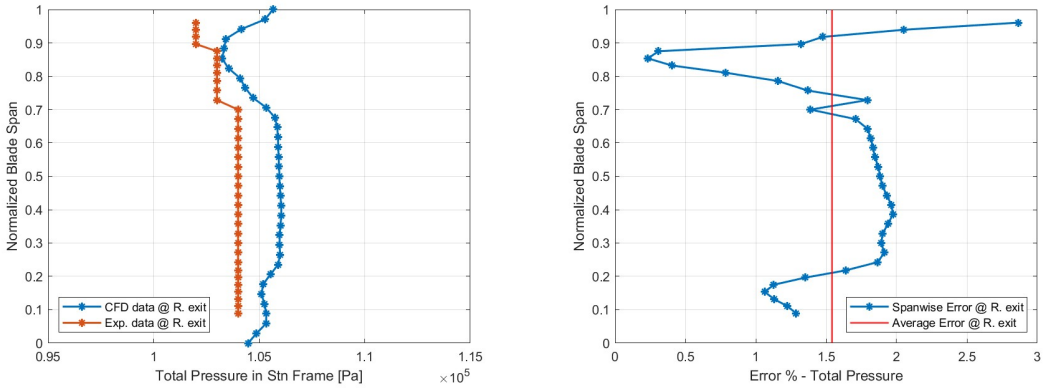


**Figure 5.11:** Tot. pressure values and errors at rotor exit plane, case 1

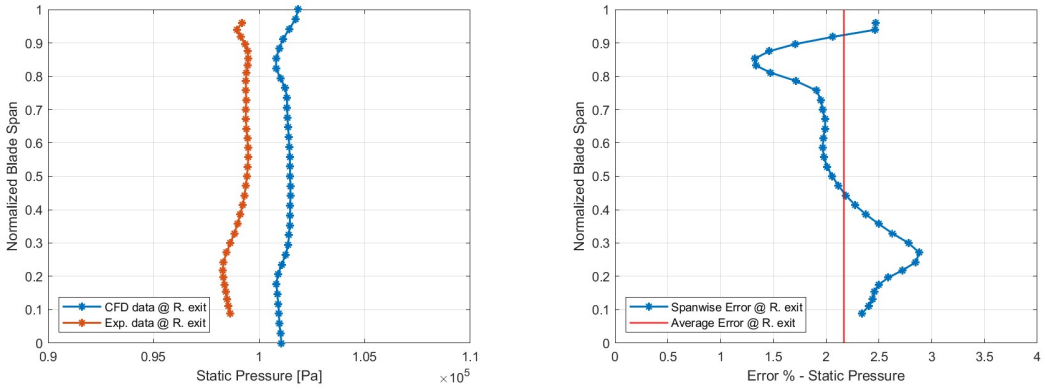


**Figure 5.12:** Stat. pressure values and errors at rotor exit plane, case 1

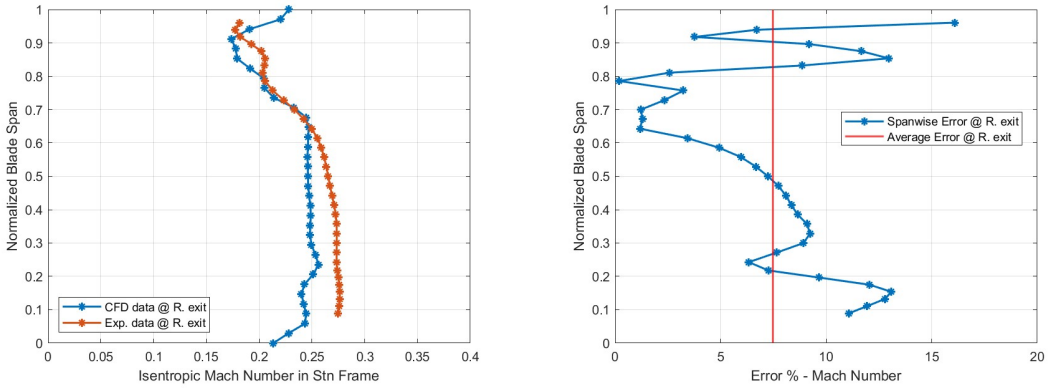


**Figure 5.13:** Mach number values and errors at rotor exit plane, case 1

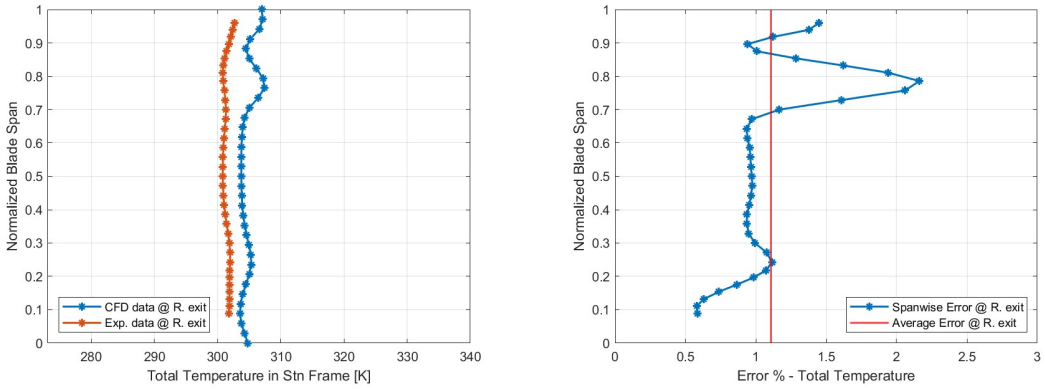


**Figure 5.14:** Tot. temperature values and errors at rotor exit plane, case 1

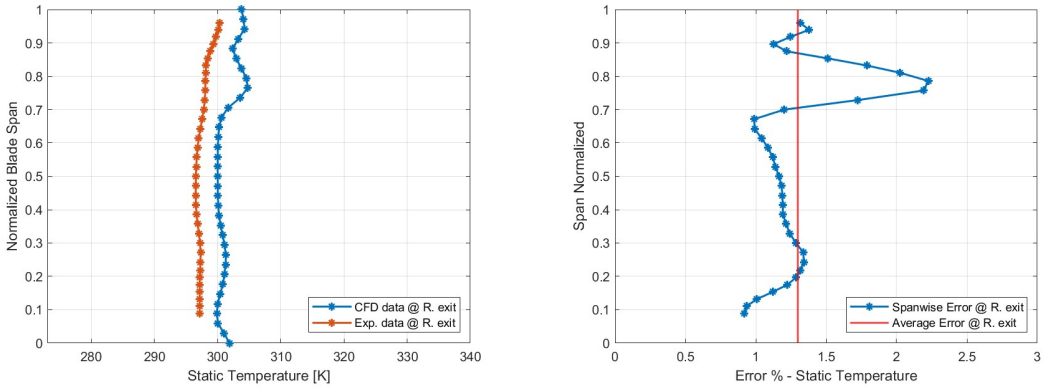


**Figure 5.15:** Stat. temperature values and error at rotor exit plane, case 1

**Case 2** The first modification tested introduces a significant grid imbalance between the stator and rotor domains. The overall node count remains consistent with case 1, keeping the computational time relatively unchanged. This setup aims to examine the following effects: the impact on stator exit results of nodes reduction on stators and the stage results refinement consequently rotor grid improvements.

**Case 3** This scenario is a time-reduced version of the previous simulation achieved by decreasing the rotor grid nodes. Stator configurations are kept consistent with case 2. The objective is to quantify the elements reduction effect on the rotating blade row, which is responsible for the turbine's power extraction. Additionally, the effect of reducing the node count imbalance between the stators and rotor domains is examined.

**Case 4** The configuration represents a further step in reducing the computational effort by significantly lowering the amount of nodes for stator grids, while maintaining the rotor domain configuration from the previous setup. As a result, approximately 0.5 million nodes are removed, yielding a computational time savings of around 30 minutes.

**Case 5** In this and the subsequent case, the stator domains are considered to have reached an effective compromise between mesh density and computational time required. The rotor row is further analyzed, focusing on tip grid refinement to ensure an accurate resolution of tip gap flow, which is essential for the recess study. In particular, this simulation involves a 0.5 million nodes reduction across the entire rotor domain while, therefore, maintaining tip region nodes count equal to case 4. Consequently, the tip to rotor node ratio increases to 15%.

**Case 6** The simulation introduces a further improvement to the rotor tip grid definition, while maintaining the same node count in the rotor body region as in the previous case. The time effort, increased by tip modifications, is considered to be minimal compared to the substantial reductions achieved in the first four cases analyzed. Stator domains remains unchanged from the previous simulation.

### 5.3.1 Stator 1 exit

Stator 1 exit measurements are used as a basis to test and verify the reliability of CFD results, ensuring an accurate flow field at the entrance of the rotor blade row. Analyzing the average errors reveals that the approximately 2 million nodes requirement, suggested by the grid independence study, is likely conservative. The node reductions, across the different configurations analyzed, do not produce

| Simulation | N. S1 | N. R[1] | N. Tip[2] | N. S2 | Time [h.min] |
|---|---|---|---|---|---|
| Case 1 | 2M | 2M | 11% | 2M | 7.15 |
| Case 2 | 1.5M | 3M | 11% | 1.5M | 7.15 |
| Case 3 | 1.5M | 2M | 11% | 1.5M | 6 |
| Case 4 | 1.25M | 2M | 11% | 1.25M | 5.30 |
| Case 5 | 1.25M | 1.5M | 15% | 1.25M | 5 |
| Case 6 | 1.25M | 1.7M | 20% | 1.25M | 5.15 |

[1]Total number of nodes, rotor body plus rotor tip.
[2]Percentage on the total number of nodes of the rotor domain.

**Table 5.1:** Simulations tested on the validation process

significant deviations in terms of both curve behavior and mean error compared to the experiment. Therefore, in this section, only measurements and error curves from case 6 are presented as a common reference for all simulations tested.

Table 5.2 presents the average errors of the analyzed flow quantities for all the configurations tested at the stator 1 exit plane.

Upon closer examination, the total pressure curve exhibits a strong alignment across all the test cases, with a maximum difference of 0.04% between the tested cases. Regarding the static pressure, the maximum disparity in average errors reaches 0.11% among the simulations. The most significant contrast among quantities is related to the Mach number variable, which displays a maximum difference of 0.46%. Conversely, the total and static temperatures yield very stable values, appearing nearly coincident throughout the analyses.

It can therefore be confirmed that, despite minimal differences in some flow quantities, the computational effort reduction consequently to the gradual grid simplifications leads to significant time advantages, without compromising the overall accuracy of the simulation results.

Figure 5.16 to Figure 5.20 show output curves, measurements and errors, of the five quantities analyzed of the sixth case simulation.

### 5.3.2 Rotor exit - first stage

Rotor exit measurements of the simulations tested are discussed in the section.

The error variations among different cases are more pronounced compared to stator exit results, as can be expected since the flow has just passed through the rotating component of the turbine.

The average errors for the analyzed quantities and efficiencies at the rotor exit are presented in Table 5.3. Generally, mean error values are approximately 1.4% to 2.2% for total and static pressure while around 1% and 1.3% for total and static

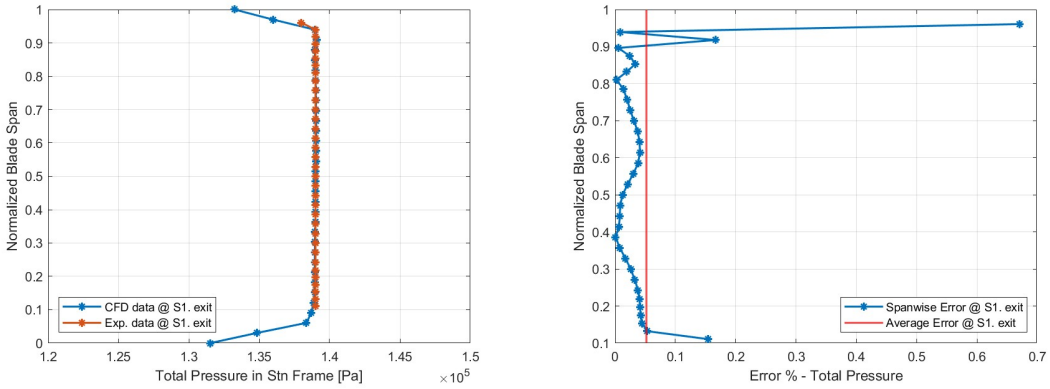


**Figure 5.16:** Tot. pressure values and errors at stator 1 exit plane, case 6

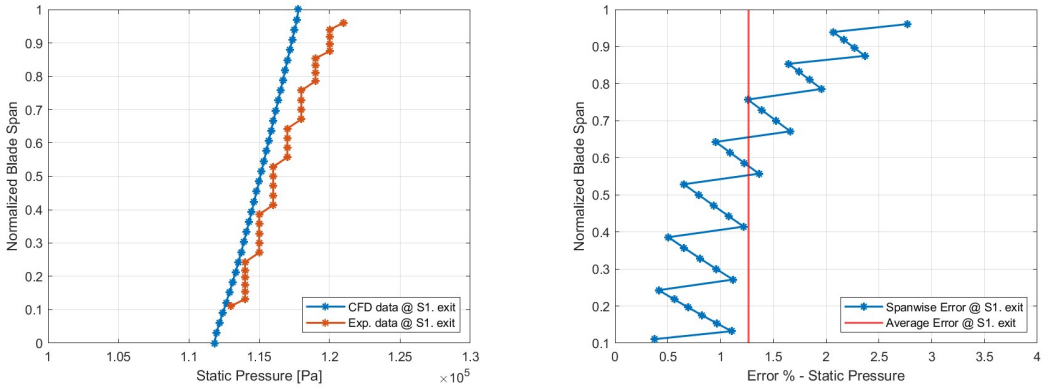


**Figure 5.17:** Stat. pressure values and errors at stator 1 exit plane, case 6

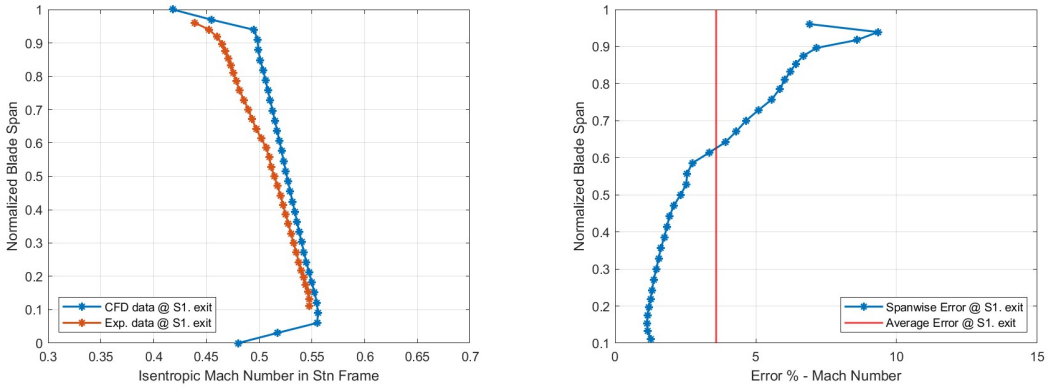


**Figure 5.18:** Mach number values and errors at stator 1 exit plane, case 6

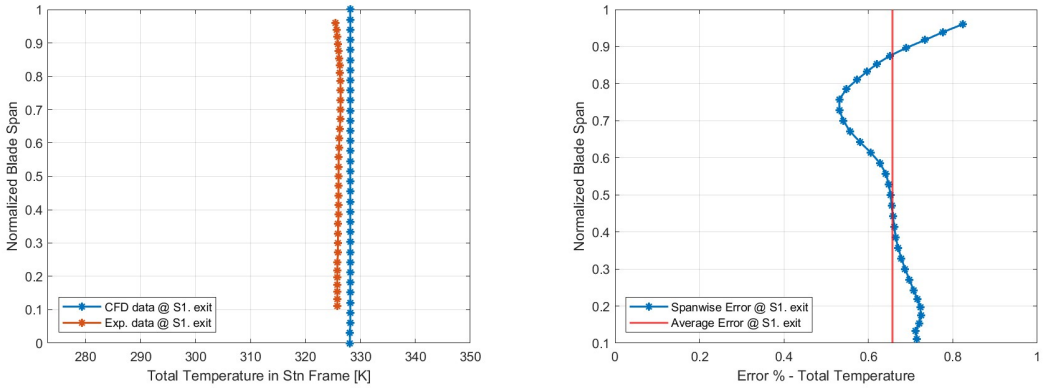


**Figure 5.19:** Tot. temperature values and errors at stator 1 exit plane, case 6

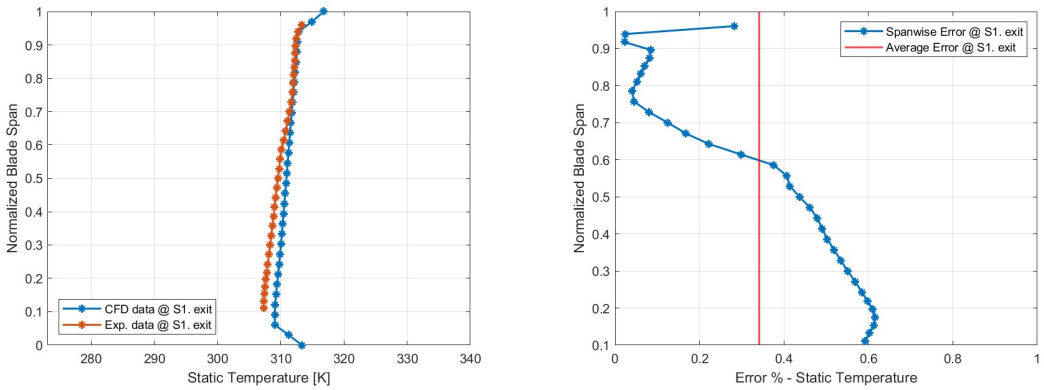


**Figure 5.20:** Stat. temperature values and errors at stator 1 exit plane, case 6

| Simulation | Average Error [%] | | | | |
|---|---|---|---|---|---|
| | $p_{\text{tot.}}$ | $p_{\text{stat.}}$ | $Mach$ | $T_{\text{tot.}}$ | $T_{\text{stat.}}$ |
| Case 1 | 0.08 | 1.21 | 3.38 | 0.66 | 0.36 |
| Case 2 | 0.09 | 1.15 | 3.14 | 0.66 | 0.39 |
| Case 3 | 0.09 | 1.15 | 3.14 | 0.66 | 0.39 |
| Case 4 | 0.08 | 1.24 | 3.44 | 0.66 | 0.36 |
| Case 5 | 0.08 | 1.24 | 3.44 | 0.66 | 0.36 |
| Case 6 | 0.05 | 1.26 | 3.60 | 0.66 | 0.34 |

**Table 5.2:** Average measurements errors at stator 1 exit for tested simulations

temperature. The Mach number results in higher discrepancies across all tested cases, with mean error values ranging from 6.6% to 7.5%. This different behavior in flow velocity compared to the experimental curve, as illustrated in Figure 5.23, may be assumed to be a consequence of the presence of cavities and inflation at the LISA-D turbine facility, which introduces secondary flow phenomena that are not accounted for in the CFD simulations.

Individual quantities and their related error curves can be found in Figure 5.21 to Figure 5.25. These graphs are addressed in the following paragraphs while commenting each case results.

As a general overview, measurements curves align sufficiently close with the experimental data across all radial position. The most significant discrepancies between the simulations tested are related to the tip span region, as may be expected due to the substantial grid modifications applied in this area. However, comparable behaviors are evident from blade root to approximately 70% of the span for all cases, indicating that the considerable reduction in the total number of nodes has not led to significant differences in performance in this region.

Besides the good quality of curve trends, it is therefore necessary to highlight the general over-prediction of the simulations, except for the Mach number, on the experimental results as well as the considerable high peaks observed in the tip region, specifically concerning total and static temperature, as illustrated in Figure 5.24 and Figure 5.25.

In the following paragraphs, a more detailed description of the individual simulations is conducted, referencing the cases descriptions in Table 5.1 and the results presented in Figure 5.24 to Figure 5.25, as well as in Table 5.3. Case 1 is not discussed, as it has already been presented in Section 5.2.

| | Average Error [%] | | | | | Performance Error [%] | | |
|---|---|---|---|---|---|---|---|---|
| **Simulation** | $p_{\text{tot.}}$ | $p_{\text{stat.}}$ | $Mach$ | $T_{\text{tot.}}$ | $T_{\text{stat.}}$ | $\mu_{TT_{\text{isen}}}$ | $\mu_{TT_{\text{poly}}}$ | $P_{ext}$ |
| Case 1 | 1.54 | 2.17 | 7.47 | 1.11 | 1.30 | 0.81 | 0.91 | 4.11 |
| Case 2 | 1.57 | 2.19 | 7.52 | 1.10 | 1.29 | 0.99 | 1.10 | 4.04 |
| Case 3 | 1.59 | 2.22 | 7.50 | 1.12 | 1.32 | 0.73 | 0.83 | 4.33 |
| Case 4 | 1.51 | 2.12 | 7.39 | 1.10 | 1.29 | 0.72 | 0.82 | 4.08 |
| Case 5 | 1.47 | 2.07 | 7.17 | 1.09 | 1.27 | 0.71 | 0.81 | 3.96 |
| Case 6 | 1.44 | 2.01 | 6.65 | 1.06 | 1.23 | 0.78 | 0.87 | 3.82 |

**Table 5.3:** Average measurements rotor exit and first stage performance errors for tested simulations

**Case 2** Compared to baseline case, the considerable increase in the number of nodes within the rotor domain does not reflect an improvement in terms of mean errors of measured quantities. On the contrary, the total and static pressure errors, as well as the Mach number error, rise of 0.03%, 0.02% and 0.05%, respectively. Total and static temperature remain nearly constant. Notably, both pressures and Mach number measurements experience considerable error spikes in the tip region compared to the other simulations tested, likely due to the elevated node density in this area. Further inaccuracy may be introduced due to the significant difference in grid node count between stator domains and rotor domain.

The observed total pressure increase is primarily driven by the pressure measurement, which counteracts the slight velocity reduction experienced. This, combined with the increase in extracted power, results in an efficiency error increase of approximately 0.18% compared to the baseline case. This underscores the need to balance the overall performance enhancement with the higher error rates relative to experimental results. Since the primary goal is to achieve reliable alignment between simulated and measured flow quantities, the increased discrepancies are considered as a critical issue, potentially overriding the absolute performance gains in the simulation.

**Case 3** Reducing the number of nodes in the rotor domain compared to case 2 results in only a slight increase in average errors, which remain within a narrow range of 0.02% to 0.03% for all measurements. Nevertheless, efficiency values experience more pronounced differences, with error reductions of 0.26% for isentropic and 0.27% for polytropic efficiency. The reason behind these behaviors may be related to the lower rotor grid resolution, which could result in a less precise capture of the local aerodynamics around the blade and, consequently, in lower differences with the experimental values. Despite this impact on efficiency, the minor increase

in errors is considered acceptable, as it allows for a one-third reduction in node count compared to case 2, bringing substantial computational time savings.

**Case 4** The fourth simulation tested represents an extreme version of the previous configuration. Stable results are achieved with the minimum number of nodes in the stator grids, resulting in a significant reduction in computational time. All the five quantities exhibit curves which have stable and favorable trends, with average errors slightly lower and in accordance with the baseline solutions. This suggests that the substantial node count reduction from case 1 to case 4 does not introduce more significant approximations related to the decreased discretization density; nevertheless the performance fluctuations seems limited while the benefit in terms of time effort required is considerable.

Furthermore, compared with the case 3, the efficiency errors see a decrease of 0.01%. Therefore, seems reasonable to conclude that the grid definition decrease on stators does not affect significantly the quality of the simulation, thereby confirming the importance of focusing on the rotor domain in order to achieve a more accurate emulation of experimental conditions.

**Case 5** This setup emphasizes the accuracy of the rotor tip region. The objective is to determine whether better results resolution of the critical tip region can be obtained without incurring excessive computational effort. In this configuration, the rotor body grid has a reduced node count relative to the previous test while the tip region maintains the same mesh density. The resulting curves exhibit behaviors similar to those observed in prior simulations. The reduction trend of average errors seen in the other cases is maintained, with considerable gains in terms of total and static pressure of 0.04% and 0.05%, respectively, as well as an improvement in Mach number accuracy by 0.22% compared to the previous case. In terms of performance, efficiency remains consistent with previous setups with a gain in extracted power of 0.12% compared to the case 4. Overall, the higher definition of the tip region results in lower errors and higher extracted power, revealing the significant impact of this region on the turbine performance.

**Case 6** This simulation incorporates insights gained from the previous attempts. Number of nodes is reduced to a minimum for both stators and rotor body, while the grid in the tip region is further refined to investigate a stable node configuration following the experience with case 5. The case 6 results in accurate curve trends similar to those observed in the other cases with significantly improved performance in terms of extracted power compared to the other simulations. Average errors achieve considerable decreases compared to the baseline for all the quantities measured. While for the other cases the error differences are less evident and detectable almost only by the mean errors, in this case the gains are visible

on the curve trends themselves. The Mach number shows the most substantial improvement, achieving a mean error reduction of approximately 0.85% compared to the highest error observed in the validation process. Regarding the performance, the efficiency experiences an increase in absolute values, as consequence of the higher extracted power achieved by the stage, which counteracts the total pressure reduction. Inevitably, a not negligible increase in average error of the efficiency metrics, by around 0.07% for isentropic and 0.06% for polytropic, is obtained compared to case 5, though still lower by 0.03% and 0.04% relative to case 1. Nevertheless, the significant improvements in terms of flow measurements and power extraction are considered more relevant for the scope of this study, indicating a favorable balance between experimental fidelity and optimized performance.

To summarize the process, six distinct CFD configurations have been tested to identify the optimal compromise between adherence to experimental measurements, performance and computational effort required. The results examined reveal accurate and satisfactory similarity with the LISA-D turbine outputs for all the simulation tested, despite the significant simplifications made in this study, such as the absence of cavities and secondary flow inflation, the use of a steady-state simulation and the assumption of domain walls as perfect surfaces with no roughness. As expected, all the trends show that the region from 70% to the shroud appears as the most critical sector of the blade, exhibiting the highest fluctuations of the measured quantities, which lead to significant aerodynamic losses and heat loads. Resulting from the validation process, the best compromise between adherence to experimental measurements curves, performance and computational effort is believed to be achieved by the sixth configuration tested. The reduction of average errors is significantly higher than the other cases despite the slight increase in efficiency errors due to better performance. This general over-prediction of quantities, and in particular of efficiencies, must be related to the strong numerical approximations considered, which reduce secondary important losses effects. Despite that, it is concluded that the sixth case simulation provides a robust and valid baseline for the following recess study.

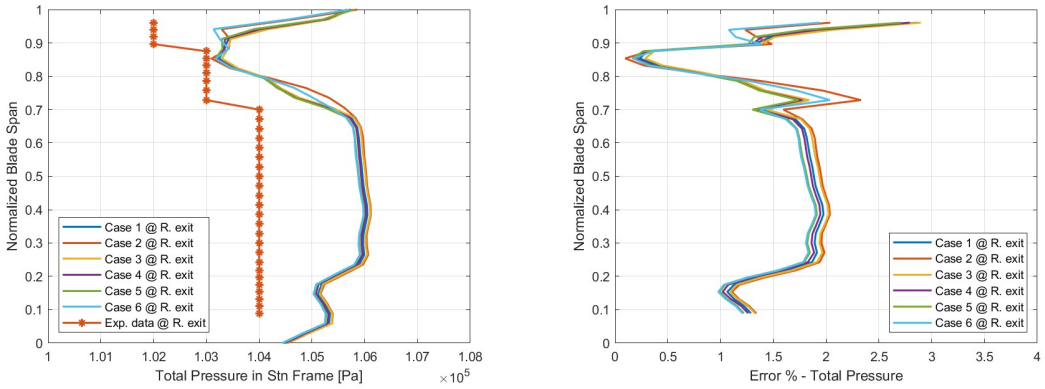


**Figure 5.21:** Tot. pressure values and errors at rotor exit for all validation cases

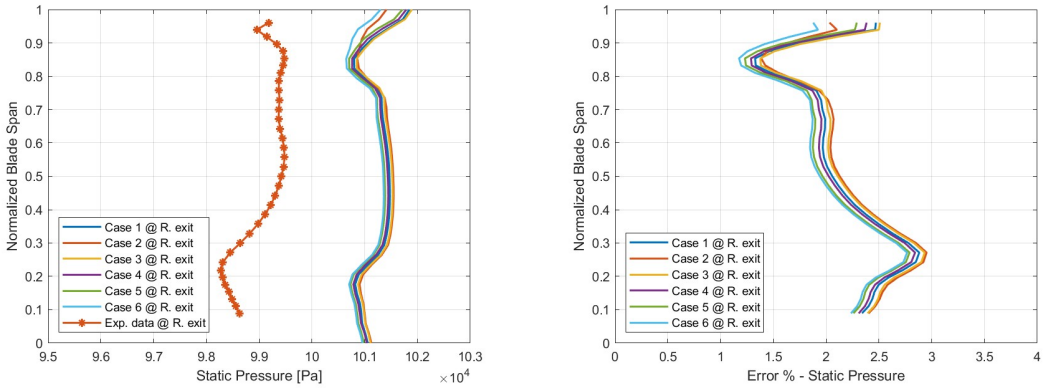


**Figure 5.22:** Stat. pressure values and errors at rotor exit for all validation cases

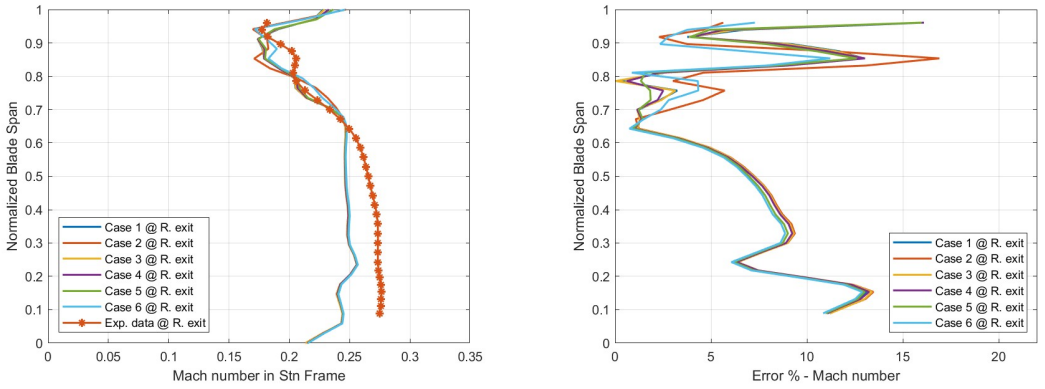


**Figure 5.23:** Mach number values and errors at rotor exit for all validation cases

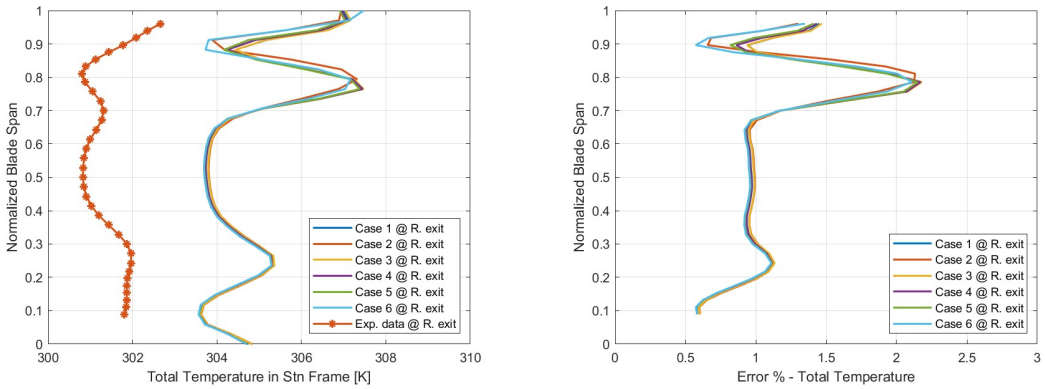


**Figure 5.24:** Tot. temperature values and errors at rotor exit for all validation cases

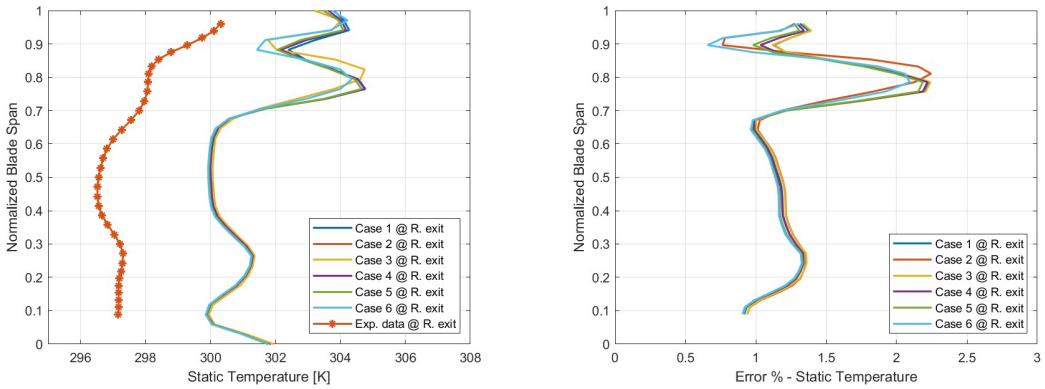


**Figure 5.25:** Stat. temperature values and errors at rotor exit for all validation cases

# Chapter 6

# Recessed tip analysis

## 6.1 Introduction

The study is conducted on a series of simulations derived from the validated configuration detailed in Chapter 5, specifically referencing simulation case 6. The computational setup remains consistent across all simulations and is identical to that used in the reference case. The only variable throughout the analysis is the rotor tip region. Specifically, different modifications are applied to the CAD model of the blade row. To ensure accurate analysis of the phenomenon without interference from other computational configuration factors of the simulation, the entire multi-domain setup remains identical to that used for the simulation resulting from the validation process. Additionally, the grid settings in the tip region are maintained without alteration, preserving discretization accuracy across the different tip geometries analyzed.

During the study, the entire 1.5 stage turbine is analyzed, in contrast with the validation analysis in the previous chapter, which focused exclusively on the first stage. This strategy allows for a more comprehensive examination of the interactions between the stationary and rotating blade rows and their respective effects on the aerodynamics, influenced by the applied geometry improvements. Moreover, the presence of a second stator row downstream the rotor can be considered as a first row of an hypothetical second stage downstream the first one, providing insights into the flow field as it would approach a subsequent rotating blade row. Therefore, the performance parameters analyzed in this chapter relate to the 1.5-stage turbine, and not to the single stage, unless specified otherwise.

For the performance analysis, the following quantities are calculated. Flow measurements are extrapolated from Ansys CFX-Post if not differently specified.

- Total-to-total polytropic efficiency;
- Tip leakage mass flow;

- Relative total pressure coefficient;
- Entropy generation.

Specifically, following the work [44], the relative total pressure coefficient is defined as:

$$C_{p_{rel,tot}} = \frac{p_{tot} - p_{stat,out}}{p_{tot,in} - p_{stat,out}} \tag{6.1}$$

Where:

- $p_{tot}$ is the total pressure in the region under analysis;
- $p_{stat,out}$ is the static pressure at the 1.5 stage outlet;
- $p_{tot,in}$ is the static pressure at the 1.5 stage inlet.

Regarding entropy generation, this study references the foundational work by Denton [3], which investigates the relationship between aerodynamic losses in turbomachines and entropy generation. Based on Denton's framework, the quantity in this study is calculated as follows:

$$\Delta s = C_p \ln\left(\frac{T}{T_{\text{ref}}}\right) - R \ln\left(\frac{p}{p_{\text{ref}}}\right) \tag{6.2}$$

Where:

- $C_p$ is the specific heat capacity of the gas at constant pressure;
- $T_{\text{ref}}$ and $p_{\text{ref}}$ are quantities at a reference state;
- $R$ is the gas constant.

In the next sections, based on Equation 6.2, $\Delta s$ is implemented for the calculation of losses generation in terms of entropy difference between two separate regions as $\Delta s_{gen} = \Delta s_{out} - \Delta s_{in}$.

The tip leakage mass flow is obtained by the following equation:

$$\dot{m}_{gap} = \rho_s \cdot A_s \cdot V_s \tag{6.3}$$

Where:

- $\rho$ is the fluid density;
- $A_s$ is the surface area considered for the calculation;
- $V_s$ is the flow normal velocity through the surface.

The analyzed quantities are typically reported as percentage differences relative to the baseline flat-tip configuration. This approach allows for a clearer comparison between solutions by highlighting the relative improvements or deviations from the baseline. The formula implemented to calculate the percentage difference for a generic quantity $\varphi$, is expressed as:

$$\Delta_{\varphi,rel} = \frac{\varphi_{sim} - \varphi_{flat}}{\varphi_{flat}} \cdot 100 \tag{6.4}$$

Where:

- $\varphi_{sim}$ is the simulation value of the quantity;
- $\varphi_{flat}$ is the baseline case value of the quantity.

Accordingly to the region analyzed, the locations for measuring flow properties may vary depending on the specific region under investigation. Generally, when referring to tip gap quantities, unless specified otherwise, these are measured at a surface within the tip blade region that is normal to the tip surface. This surface follows the camber line of the blade tip section and spans the gap from the tip surface to the external casing. Alternatively, in case of deeper examination of the gap region, surfaces on pressure and suction sides of the blade tip may be utilized to capture specific quantities. Figure 6.1 illustrates an example of tip gap geometry with measurements planes in place, which are used to capture quantities such as tip gap leakage flow and total pressure.

Regarding the process of the current study, the work by Misho [44] is referenced as a starting point for the recess analysis. The geometry of the tip cavity is described using the following geometrical dimensions:

- Length of the cavity $L_{rec}$, as the maximum distance between internal points;
- Depth of the cavity $h_{rec}$, as it is measured from the flat tip surface to the internal plane created by the recess in radial direction;
- Thickness of the cavity rims $d_{rim}$, resulting from the excavation process into the blade.

Figure 6.2 shows the three dimensions on an example of tip recess cavity. Moreover, it is important to highlight the clear division between the blade body and the tip region which are meshed with structured hexahedral grid and with unstructured tetrahedral grid respectively. This difference is evident below when the different cavities are presented.

The analysis is conducted in sequential steps, each defined by different modifications applied to the rotor tip. Firstly, the effects on cavity length and depth are examined, conducting a parametric analysis on nine different configurations, which are obtained by varying these two quantities. In the second step, modifications are made to the geometry derived from the previous analysis by changing the width of the cavity rim, leading to the evaluation of two additional solutions. Overall, a total of eleven configurations are computed during the entire process.

To evaluate the beneficial improvements or drawbacks related to the new geometries, a performance analysis is conducted after each simulation step. Finally, a detailed analysis of the aerodynamic losses is conducted based on the tip gap geometry resulting from the two-step process. The flow structures generated by the recess cavity are described and compared to those from the flat tip baseline simulation, aiming to identify the causes and effects of any potential advantages or disadvantages related to the novel geometry.

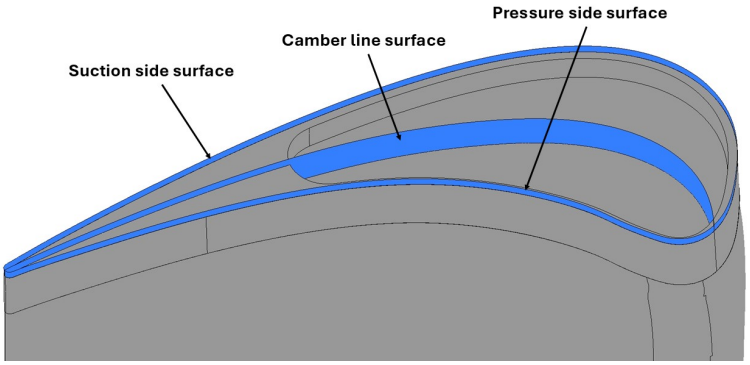


**Figure 6.1:** Recessed rotor tip surface with measurement planes

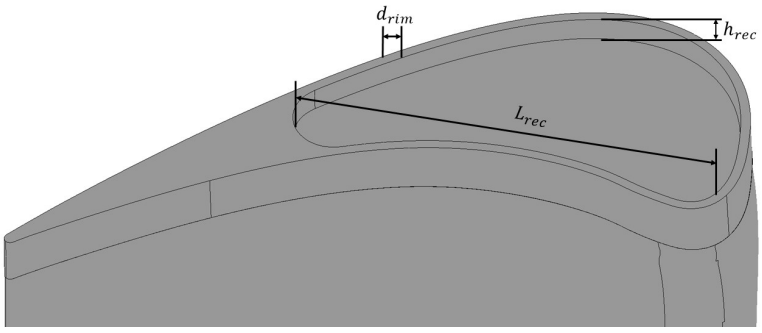


**Figure 6.2:** Characteristic dimension of a tip recess cavity

## 6.2 Aerodynamic analysis of 1.5 stage flat tip configuration

The resulting simulation from the validation process in Chapter 5 is referred to as the baseline flat tip configuration. The full 1.5 stage turbine is considered for the study; therefore, a summary of the fundamental features of the simulation, along with the main performance results obtained, is presented in Table 6.1.

| **Parameter** | **Value** | **Units** |
|---|---|---|
| N. nodes S1 | 1.25M | - |
| N. nodes R | 1.7M | - |
| N. nodes S2 | 1.25M | - |
| T.-to-t. poly. eff. $\boldsymbol{\mu_{TT_{\text{poly}}}}$ | 0.88 | - |
| Rel. tot. pressure coeff. @ tip gap $\boldsymbol{C_{p_{rel,tot}}}$ | 0.47 | - |
| Delta entropy $\boldsymbol{\Delta s_{gen,1.5}}$[1] | 10.52 | $\frac{J}{kgK}$ |
| Leakage mass flow $\frac{\dot{m}_{gap}}{\dot{m}_{main}}$ | 2.87 | % |

[1]Entropy generation between turbine inlet and turbine outlet.

**Table 6.1:** Main characteristics and performance of the flat tip baseline simulation

The aerodynamics of vortices created within the computational multi-domain is analyzed, focusing on the flow structures detected and their relevance in terms of contributes to the total losses. The analysis is organized in three sections, corresponding to the three blade rows, emphasizing the interactions between the flow and the blades, as well as the interactions between successive rows.

### 6.2.1 Stator 1 passage

The first row of stationary blades encounters a stream flow which is well-aligned with the axial direction. The deviation imposed on the flow results in a significant pressure difference between the suction and pressure sides of the blade, leading to corresponding increases and decreases in velocity.

The presence of the hub and shroud walls contributes to the formation of passage vortices, which generate after the flow passes the maximum width of the blade profile, close to the inner and outer casing. Those structures gradually intensify as they extend to cover the first 20% and the last 20% of the blade span in the radial direction, ultimately leaving the blade at the trailing edge. The behavior of these vortices is illustrated in Figure 6.4, where they are numbered 1 and 2 respectively. In these regions, total pressure and velocity reduce while temperature

increases, resulting in an increase in entropy generation, as shown in Figure 6.3, where vortices are numbered as in Figure 6.4. This rise in temperature also leads to elevated heat loads on the blade surfaces.

Finally, the passage vortices generated leave the stator proceeding downstream. Although, they tend to mix and align with the main flow, they still exhibit significant entropy differences, up to an order of magnitude, when entering the rotor domain.

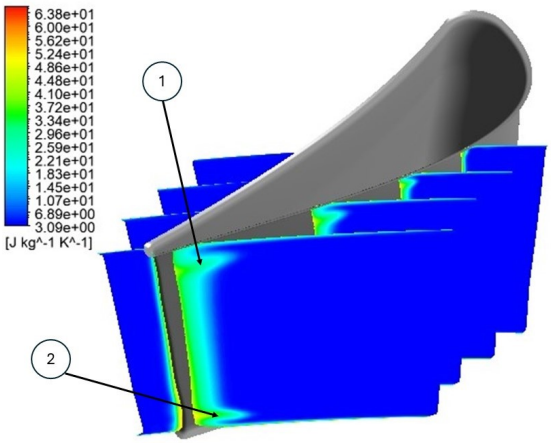


**Figure 6.3:** Entropy generation along the stator 1 axial chord

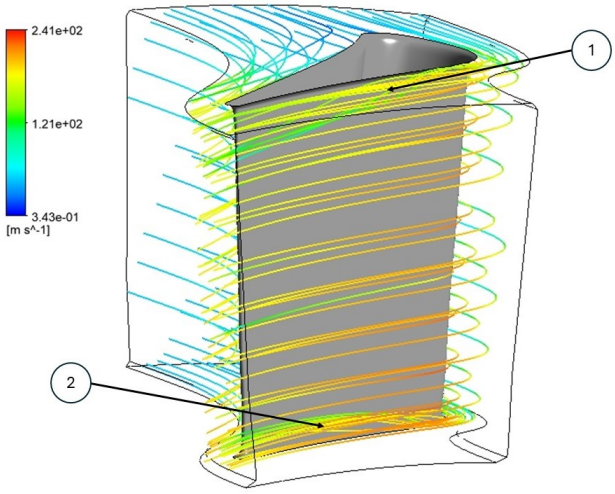


**Figure 6.4:** Vortices visualization through streamlines of the stator 1 flow

### 6.2.2 Rotor passage

The fluid stream, passing through the rotational blade row of the turbine, inevitably experiences significant modifications in its characteristics. Due to the sudden rotation imposed on the flow, the passage vortices acquire more energy compared to those in the upstream stator. Consequently, the entropy generation increases to nearly double that of the vortices in the first domain, as shown in Figure 6.5. Moreover, the turbulence is not only stronger but is also broader, covering the first 25% of the blade span from the hub and from 70% of the blade span to the shroud casing near the trailing edge.

The upper passage vortex in radial direction is pushed towards the mid-span by the progressive formation of the tip leakage vortex, which develops along the external casing and the suction side of the blade tip. In fact, as indicated in Table 6.1, 2.87% of the main flow does not enter the main passage of the rotor domain, instead, it transitions from the pressure side to the suction side of the blade, driven by the pressure difference. The mass quantity entering the clearance in the first $60\% - 70\%$ of the tip's axial chord combines with the passage vortex downstream, causing the increasing in entropy thanks to the additional mass being transported. Conversely, the percentage of leakage entering along the pressure side downstream generates the tip leakage vortex, which rotates in opposite direction to the passage vortex. This tip leakage vortex exhibits similar entropy characteristics to the passage vortex; however, it experiences an overall lower velocity, likely due to the reduced mass flow transported compared to the other vortex.

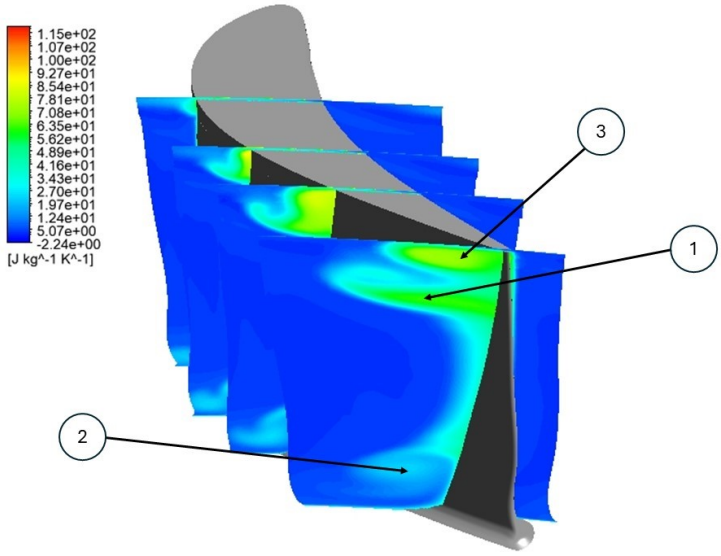


**Figure 6.5:** Entropy generation along the rotor axial chord

In Figure 6.7, the focus is on the vortices in the tip region, clearly illustrating the opposite direction of rotation of the two flow structures generated by the tip leakage secondary flow.

This results in a robust vortex system forming on the suction side of the blade, where the two structures initially are not easily distinguishable but physically separate as they proceed downstream. Once exiting the rotor blade, as shown in Figure 6.8, the passage vortex tend to dissipate, mixing with the more uniform main flow. This behavior is particularly evident regarding the structure close to the blade root, forming the inner passage vortex, while the outer passage vortex exhibits less significant energy reduction and dissipates more slowly. In contrast, the tip leakage vortex retains its energy with only a slight decrease, remaining compact and ready to enter the second stator domain almost unaltered.

Figure 6.5 to Figure 6.8 show the described vortical structures, numbering them as follows: (1) outer passage vortex, (2) inner passage vortex and (3) tip leakage vortex.

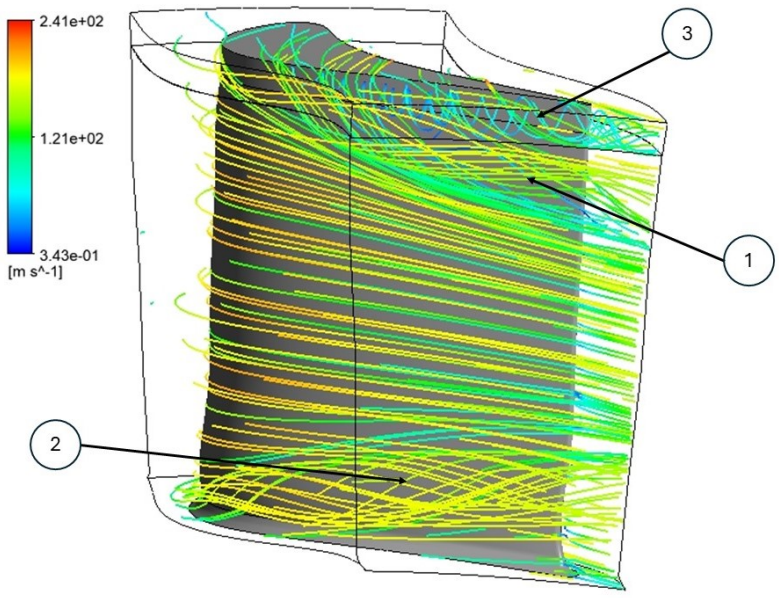


**Figure 6.6:** Vortices visualization through streamlines of the rotor flow

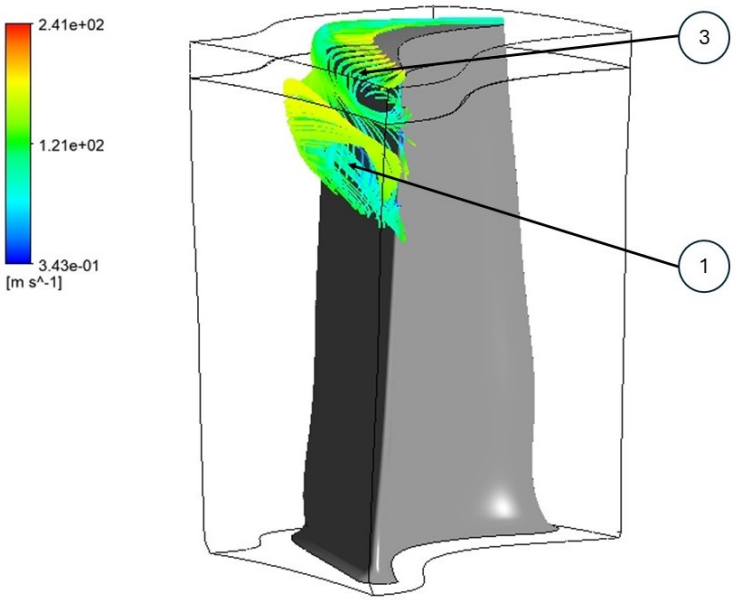


**Figure 6.7:** Particular on tip region vortices generated by the tip leakage mass flow

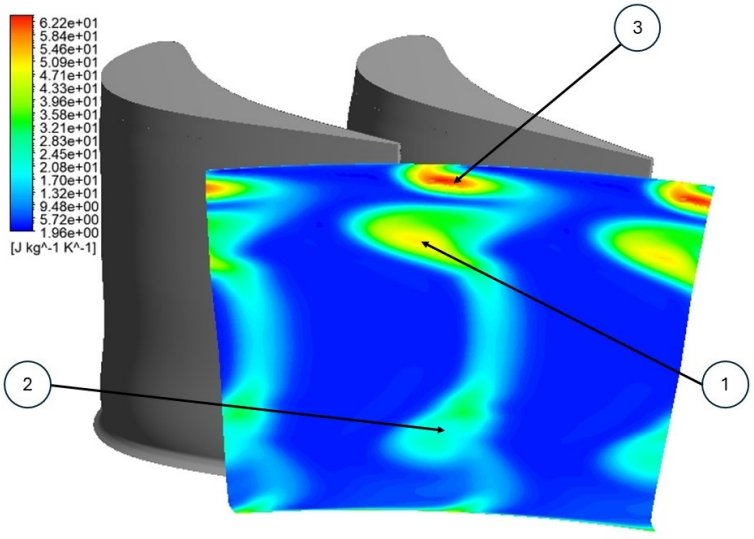


**Figure 6.8:** Rotor domain exit region, entropy generated by vortical structures

### 6.2.3 Stator 2 passage

The second stator encounters a highly turbulent flow field resulting from the rotating blade row upstream, as discussed in the previous section. The two upper vortical structures are distinguishable already at the leading edge of the blade, while the passage vortex located close to the hub casing generates similarly to that seen in the first stator of the turbine.

As the flow moves along the blade in the axial direction, the downstream structure generated by the tip leakage vortex tends to reduce its strength. However, this reduction is counterbalanced by the increasing intensity of the passage vortex, which does not merge with the tip leakage vortex but instead sustains it until it reaches the trailing edge of the blade.

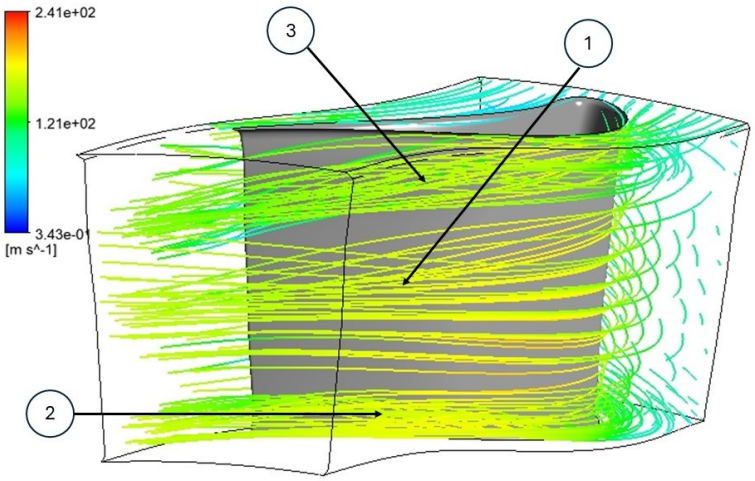


**Figure 6.9:** Vortices visualization through streamlines of the stator 2 flow

While flowing towards the trailing edge, the inner passage vortex remains confined to the first 20% of the blade span, while the other two structures travel down along the suction side surface of the blade, extending from the shroud to midspan.

Compared to the rotor vortices, the entropy generated is lower, in accordance with expectations, nevertheless their influence on the stator passage region is more pronounced, thanks to the increasing of the overall energy of a broader portion of region between adjacent stator blades, as illustrated in Figure 6.10.

The two upper structures tend to merge as they exit the blade downstream, resulting in a reduction of their strength and a more homogeneous mixing with the surrounding flow field.

Figure 6.9 and Figure 6.10 show the described vortical structures, numbering them as follows: (1) outer passage vortex, (2) inner passage vortex and (3) tip leakage vortex.

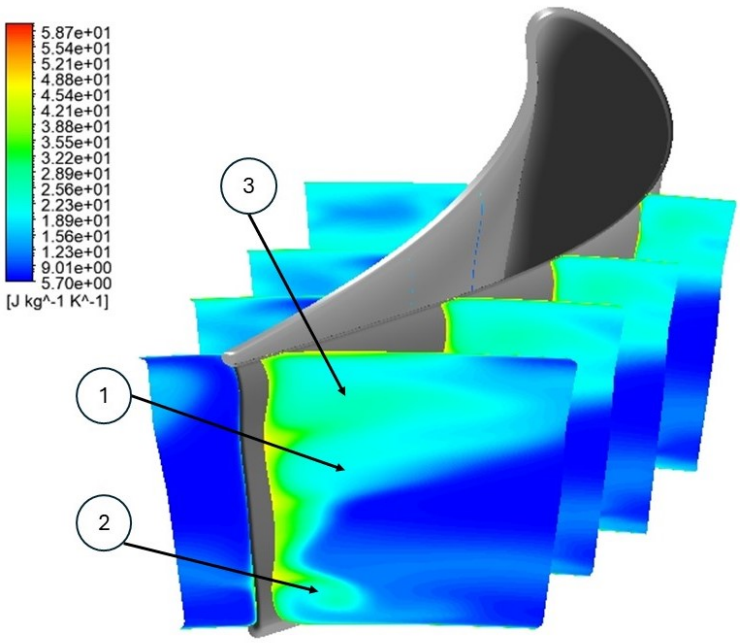


**Figure 6.10:** Entropy generation along the stator 2 axial chord

## 6.3 Geometric modifications of rotor blade tips - step 1

A parametric analysis is initially conducted on two of the three geometric quantities outlined in the study introduction. The cavity is carved into the flat surface of the rotor tip, controlling the length and depth of the new recess. The thickness of the newly created rims is kept constant and it is the objective of the second step of the analysis.

The length of the recess $L_{rec}$ is defined as a proportion of the rotor tip true chord, resulting in three distinct cavity configurations:

$$\frac{L_{rec}}{L_{ch}} = 80\% \tag{6.5}$$

$$\frac{L_{rec}}{L_{ch}} = 70\% \tag{6.6}$$

$$\frac{L_{rec}}{L_{ch}} = 60\% \tag{6.7}$$

The other two quantities are selected based on the tip gap clearance, denoted as $h_{gap}$, which is constant at 1% of the rotor hub-shroud radial distance for the flat tip configuration. The depth of the recess created, $h_{rec}$, acquired the following values:

$$\frac{h_{rec}}{h_{gap}} = 1 \tag{6.8}$$

$$\frac{h_{rec}}{h_{gap}} = 2 \tag{6.9}$$

$$\frac{h_{rec}}{h_{gap}} = 3 \tag{6.10}$$

Regarding the thickness of the tip rims, $d_{rim}$, a fixed value is temporarily chosen, referencing to the work of Mischo [44], corresponding to:

$$\frac{d_{rim}}{h_{gap}} = 1.1 \tag{6.11}$$

The resulting nine tip recess cases, as presented in Figure 6.11, Figure 6.12 and Figure 6.13, are tested while maintaining the same computational setup and discretization settings in order to accurately capture the contributions of the various geometries, thereby minimizing potential interferences in the results.

## 6.4 Performance comparison - step 1

In this section, the performance results obtained from the first of two parametric analyses on the geometric dimensions of the recessed rotor blade tip are presented.

The main performance metrics, as outlined earlier in this chapter, are plotted for all the nine tip modifications applied in Figure 6.14 to Figure 6.19. The graphs shows the measured quantities as a function of the cavity depth ratio, parametrized with the length ratio of the recess.

A leakage mass flow reduction is detected for all the simulations tested with a maximum decrease of approximately 20% compared to the flat tip baseline. Concerning the overall aerodynamic losses encountered within the 1.5 stage turbine, the recessed tip achieves a substantial reduction of the generated entropy throughout the turbine expansion. The quantity reduction varies from 3.5% to almost 5% among the geometries tested. This reduction of losses reflects, as expected, an increase in 1.5 stage efficiency up to 0.68% compared to the flat tip simulation.

Regarding tip cavity internal losses, Figure 6.17 and Figure 6.18 display trends in entropy generation and total pressure losses as captured by two measurement

**Figure 6.11:** Recessed rotor tip with $\frac{L_{rec}}{L_{ch}} = 80\%$ for the three different depths

**Figure 6.12:** Recessed rotor tip with $\frac{L_{rec}}{L_{ch}} = 70\%$ for the three different depths

**Figure 6.13:** Recessed rotor tip with $\frac{L_{rec}}{L_{ch}} = 60\%$ for the three different depths

planes, on pressure and suction side of the tip, for the first quantity and by the camber line plane, normal to the tip surface, for the second parameter. Interestingly, the geometries that exhibit the most substantial performance improvements in terms of efficiency and overall entropy reduction also show higher internal losses within the tip cavity. This trend, which may appear counterintuitive, is likely due to the vortical structures forming inside the cavity. Increased cavity depth and length amplify vortex strength, which cause higher dissipation and losses in that confined region. Nonetheless, the significant leakage mass flow reduction, achieved by cavities with grater free volume, leads to notable entropy generation reduction once the secondary tip flow exits the cavity and merges with the main flow along the suction side of the rotor blade. This observation is well described by Denton [3], analyzing entropy generation in fluid mixing processes. The research shows that when the injected secondary stream is relatively small in mass, the downstream entropy generation depends largely on the ratio of mass flows being mixed:

$$\Delta s \propto \frac{\dot{m}_{gap}}{\dot{m}_{main}} \tag{6.12}$$

Consequently, the main flow experiences less disturbance from the leakage secondary flow compared to the flat tip case and this leads to a significant reduction in entropy generation outside the cavity along the rotor and downstream towards the stator. Moreover, this effect is corroborated by the nearly complete recovery of total pressure by the time the flow exits the turbine, as illustrated in Figure 6.19.

To examine further deeper the underlying mechanisms behind these results, the aerodynamics aspects and analysis of the internal cavity vorticity, are discussed in details in a subsequent section with the aim to address global performance behaviors to specific phenomena occurring within the recessed tip geometry.

In conclusion, despite the non-negligible increase in total pressure losses and entropy generation within the gap compared to the flat tip case, the overall performance of the 1.5 stage turbine benefits from a significant reduction in tip leakage mass flow. It is therefore important to highlight that all the configurations tested in this study demonstrate improved performance across the various cavity geometries analyzed. Notably, the cavity geometry yielding the most significant improvements is the one with $\frac{L_{rec}}{L_{ch}} = 80\%$ and $\frac{h_{rec}}{h_{gap}} = 3$. As a result, this configuration is implemented for the second part of the study where the thickness of the cavity rims is parametrized.

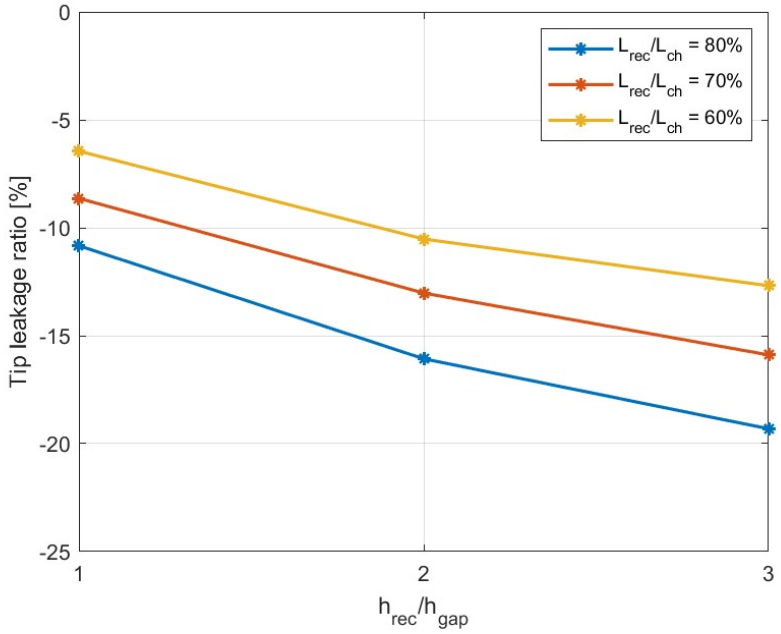


**Figure 6.14:** Tip gap leakage mass flow ratio, step 1

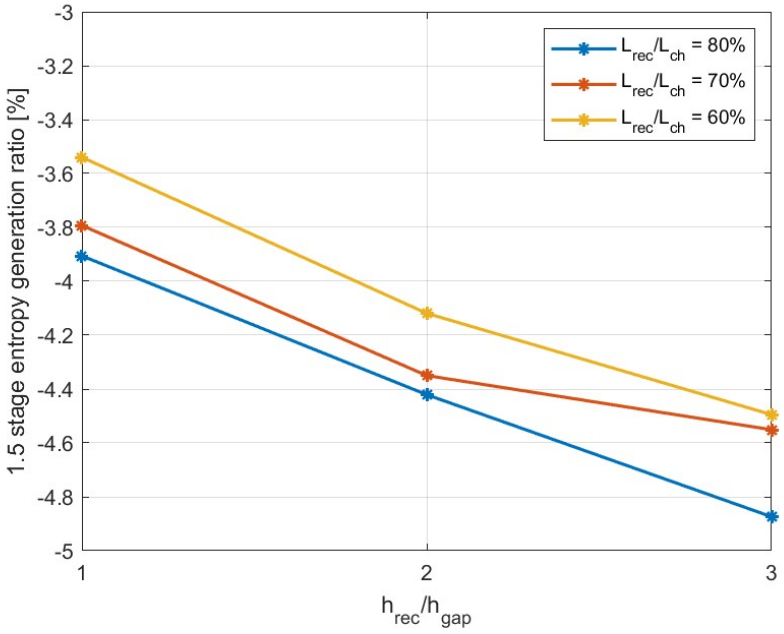


**Figure 6.15:** 1.5 stage entropy generation ratio, step 1

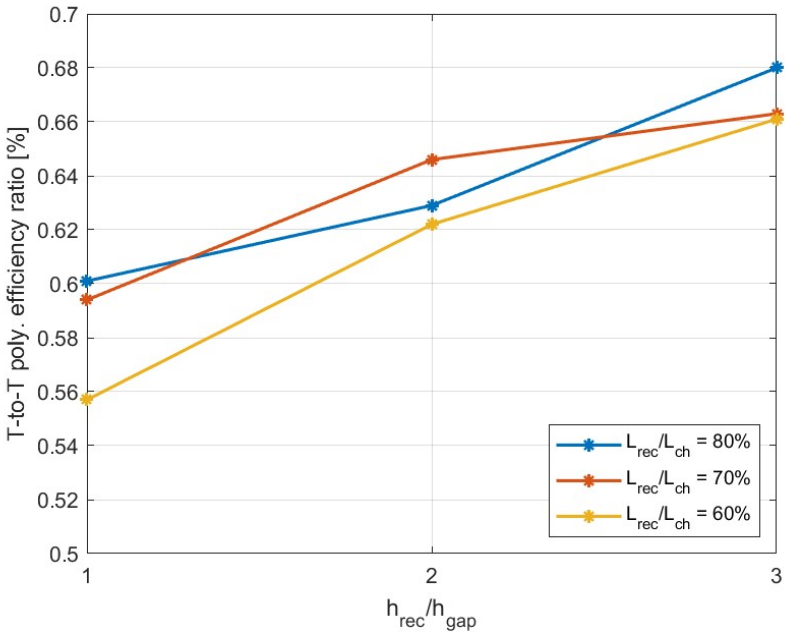


**Figure 6.16:** T.to T. polytropic efficiency ratio, step 1

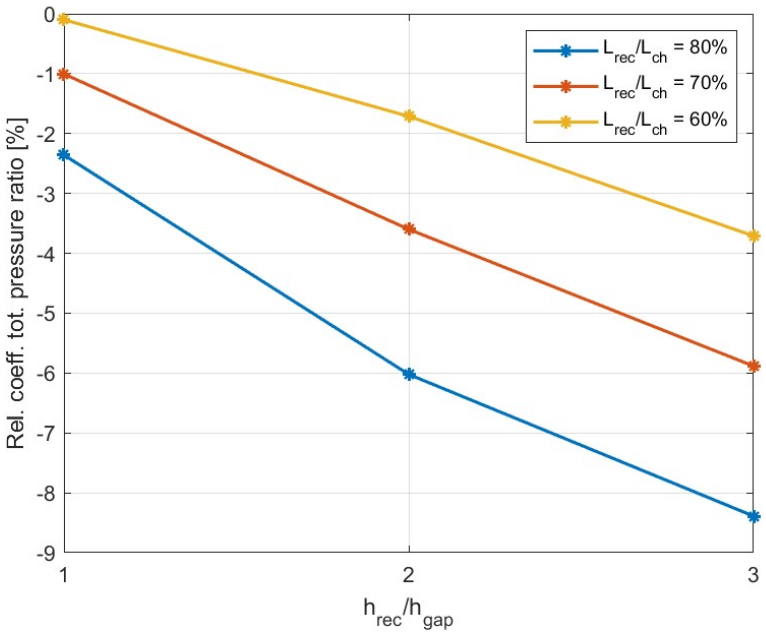


**Figure 6.17:** Total pressure coefficient ratio within the tip cavity, step 1

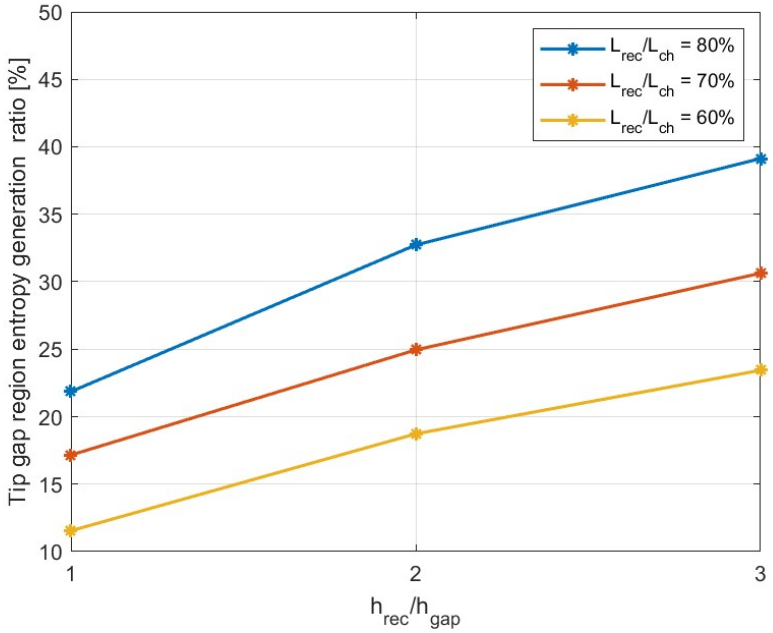


**Figure 6.18:** Entropy generation ratio within the tip cavity, step 1

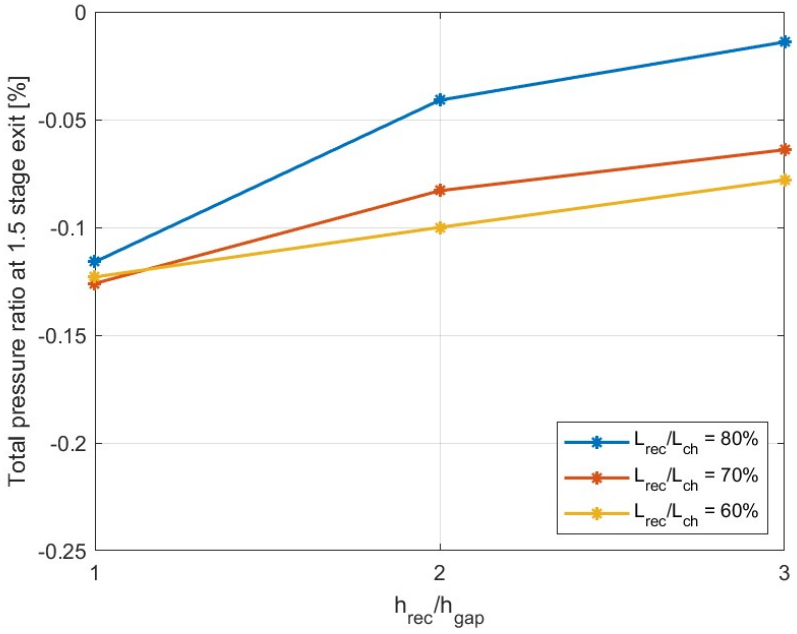


**Figure 6.19:** Total pressure ratio at the 1.5 stage exit, step 1

## 6.5 Geometric modifications of rotor blade tips - step 2

The second step of the recessed tip study is conducted on the thickness of the rims which are created by carving the blade for the creation of the tip cavity.

In this analysis, the baseline is established using the resulting tip geometry from the previous step of the process, hence, length and depth of the cavity are kept constant respectively to 80% of the true chord and three times of the clearance height. The rim thickness is then parametrized according to the following scheme. Baseline case:

$$\frac{d_{rim}}{h_{gap}} = 1.1 \tag{6.13}$$

The distance between internal surface of the tip cavity and external surface of the blade is initially reduced by half compared to the step 1 case:

$$\frac{d_{rim}}{h_{gap}} = 0.55 \tag{6.14}$$

Subsequently, the thickness is increased by half compared to the baseline case:

$$\frac{d_{rim}}{h_{gap}} = 1.65 \tag{6.15}$$

Figure 6.20 illustrates the recessed rotor tips with the newly tested thickness, while maintaining length and depth of the cavity as defined in the previous step of the analysis.

## 6.6 Performance comparison - step 2

The performance results from the second part of the tip recess analysis are discussed. Figure 6.21 to Figure 6.26 present the analyzed quantities as function of the $\frac{d_{rim}}{h_{gap}}$ ratio. Among the two new simulations tested, the base simulation resulting from the previous step is shown as reference. However, it is important to note that the ratios calculated are still compared against the flat tip baseline case.

The results indicate a significant further improvement in terms of 1.5 stage efficiency when the rim thickness is reduced to half of the original measurement. This behavior is in accordance with the machine overall entropy generated which decreases by approximately 6.7% compared to the flat tip case. Similarly to the step 1 analysis, the relative total pressure coefficient and the entropy generated exhibit a trend of reduced losses in the gap region with the increasing of the rim thickness. Considering the hypothesis presented in the first step of the analysis,

**Figure 6.20:** Recessed rotor tip with $\frac{L_{rec}}{L_{ch}} = 80\%$ and $\frac{h_{rec}}{h_{gap}} = 3$ for the three different rim thickness

these trends can be explained by the reduction of available free volume for the vortical structures to form, which cause the increase in leakage through the gap and a subsequent reduction in performance across the various thickness ratios. These consideration are well justified by $\frac{d_{rim}}{h_{gap}} = 0.55$ and $\frac{d_{rim}}{h_{gap}} = 1.1$ simulations, while the configuration with thicker cavity rims seems to diverge, showing different behaviors.

The simulation characterized by $\frac{d_{rim}}{h_{gap}} = 1.65$ exhibits higher performance, compared to the baseline case from step 1, which is not expected since, conversely, the behavior inside the tip gap is consistent with the trend and justifications given for all the other configuration tested, both in step 1 and step 2.

A deeper examination reveals that the velocity reduction in the tip gap observed from case $\frac{d_{rim}}{h_{gap}} = 1.1$ to case $\frac{d_{rim}}{h_{gap}} = 0.55$ does not persist with the same magnitude from case $\frac{d_{rim}}{h_{gap}} = 1.65$ to case $\frac{d_{rim}}{h_{gap}} = 1.1$. In other words, the rim thickness increase does not linearly affect the formation of vorticity within the recess. A similar observation applies to static pressure, which shows a more pronounced increase in case $\frac{d_{rim}}{h_{gap}} = 0.55$ but remains relatively constant between case $\frac{d_{rim}}{h_{gap}} = 1.1$ and case $\frac{d_{rim}}{h_{gap}} = 1.65$. These factors contribute to a less noticeable total pressure difference between these two last configurations compared to the significant difference observed between case $\frac{d_{rim}}{h_{gap}} = 0.55$ and case $\frac{d_{rim}}{h_{gap}} = 1.1$ , as evidenced by the relative total pressure coefficient in the tip gap. Consequently, the leakage mass flow, directly related to tip gap velocity, shows comparable quantities for these two simulations, as shown in Figure 6.21.

Conversely, the entropy generated within the cavity in configuration with thicker rims, which is independent of velocity, continues the decreasing trend seen from the other two simulations, as presented in Figure 6.25. This is likely driven by reductions in both static pressure and temperature due to lower vorticity levels.

This dual phenomenon, minimal leakage reduction paired with significant entropy generation increase, produces a particular effect downstream. In step 1 of the recess study, simulations with cavities of the same length consistently showed that leakage mass flow reduction corresponded to an increase in tip gap entropy. However, between case $\frac{d_{rim}}{h_{gap}} = 1.65$ and case $\frac{d_{rim}}{h_{gap}} = 1.1$, the minimal decrease in leakage does not offset the significant entropy augmentation. When the main flow and the secondary flow from case $\frac{d_{rim}}{h_{gap}} = 1.65$ mix downstream of the rotor blade, the smaller leakage increase fails to outweigh the entropy reduction in the secondary flow. Consequently, the combined flow exhibits reduced instability and lower entropy at the turbine exit compared to case $\frac{d_{rim}}{h_{gap}} = 1.1$, even though the leaked mass from the tip gap is slightly greater.

In conclusion, reducing the rim thickness of the cavity does not affect linearly the mass flow leaking from the tip gap of the rotor blade, which although maintains the proportionality with cavity volume increase. Moreover the results from step

2 confirm the analysis presented in step 1 of the study, indicating that optimal performance is associated with an increase in cavity volume.

In the following section, a deeper investigation on the vortical structures generated inside the tip cavity is conducted, trying to specifically address the performance trends already presented.

## 6.7 Aerodynamic analysis of the tip cavity

The aerodynamics of the recessed rotor tip region in the geometrical configuration where the best performance are obtained is analyzed. The work by Mischo et al. [33] is considered as reference for the analysis of the vortical structures detected, which are displayed in Figure 6.27.

As the flow stream enters the rotating domain, it encounters the leading edge of the blade. The fluid within the region from the outer casing to approximately 85% of blade span in radial direction, is drawn into the tip clearance by the pressure difference between pressure and suction side of the blade tip. Once entering the cavity, different vortical structures can be distinguished depending on the gap portion.

The streamlines (1), originating primarily from the shroud wall boundary layer, directly hitting the leading edge stagnation point, traverse almost undisturbed the recess until they are deflected by the suction side rim. Upon exiting the gap, they merge with the newly formed passage vortex along the suction side of the blade. A smaller number of streamlines, which encounter the initial portion of the suction side of the profile, are captured by the cavity, where they instantly roll up against the suction side, generating a vortex (2) at the very beginning of the blade profile. This structure does not survive the convergence with the flow coming from the stagnation point, it merges with it and exits the gap on the suction side, joining again the passage vortex.

Regarding the portion of the flow captured by the cavity from the pressure side downstream of the stagnation point at the leading edge, two distinct paths emerge depending on the axial position at which they enter the recess. A first significant vortical structure (3) is clearly detectable against the internal rim on the pressure side, generated by the streamlines entering from the pressure side portion between 20% and 30% of the axial chord. This vortex proceeds downstream undisturbed, occupying the entire distance between the two opposite rims of the blade tip and leaving the gap gradually until it disappears at the extremity of the recess. Once it exits, its streamlines generate the tip leakage vortex, which progressively gains space between the shroud and the passage vortex as it moves downstream. The creation of the tip leakage vortex is further sustained by the flow (4) entering the cavity from 30% of the axial chord on the pressure side until the trailing edge of

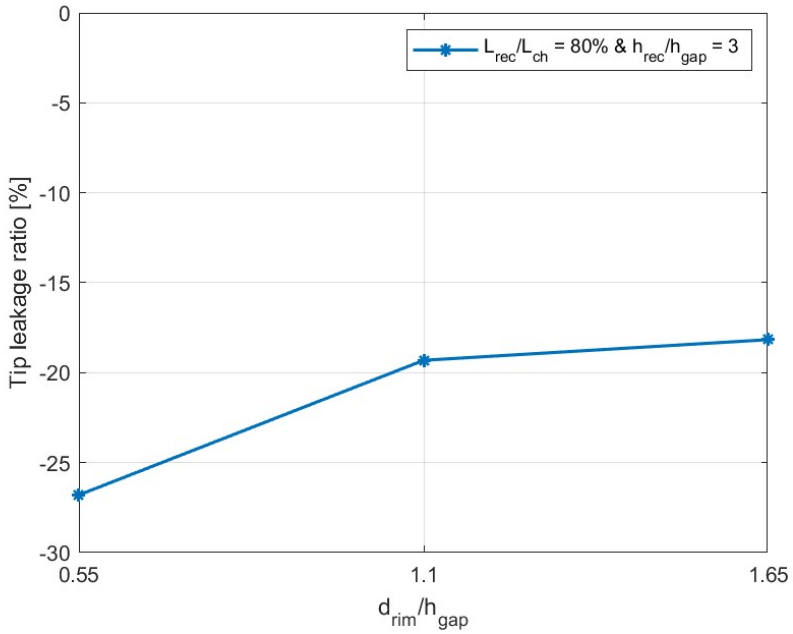


**Figure 6.21:** Tip gap leakage mass flow ratio, step 2

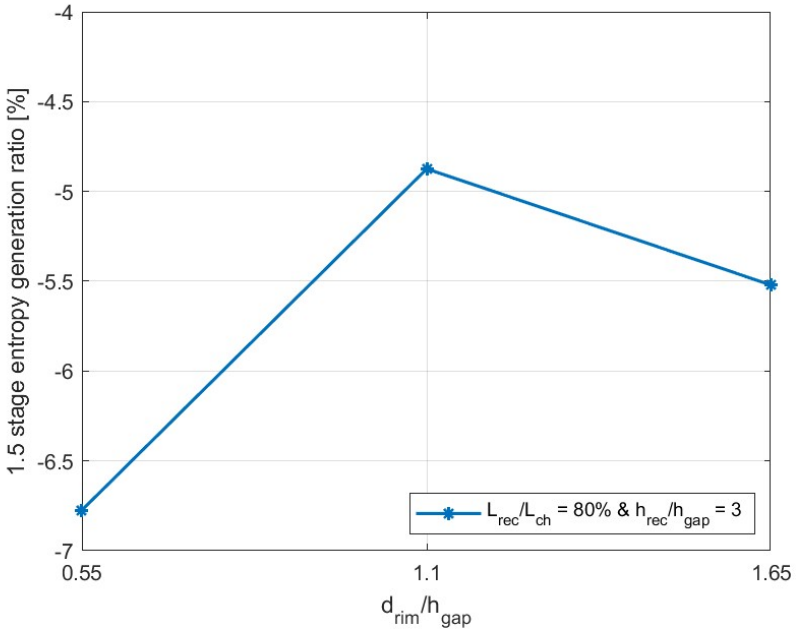


**Figure 6.22:** 1.5 stage entropy generation ratio, step 2

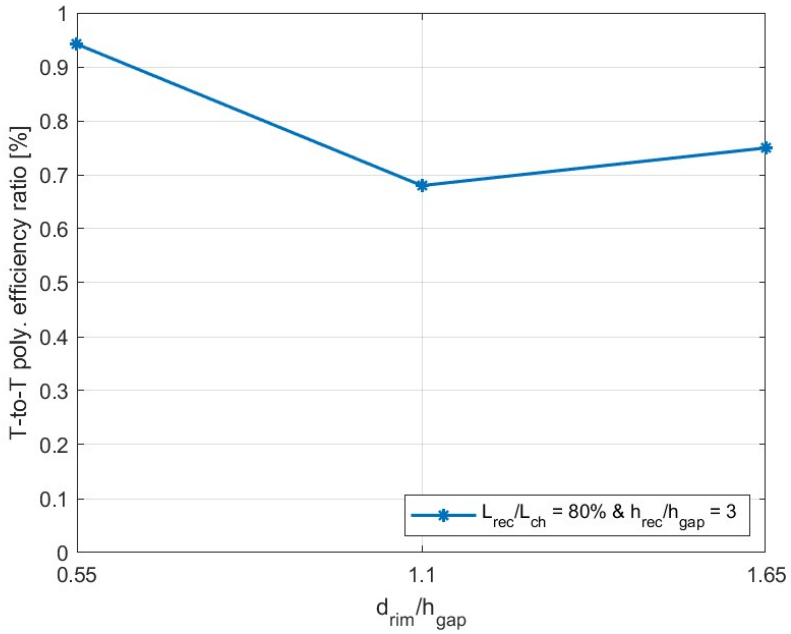


**Figure 6.23:** T.to T. polytropic efficiency ratio, step 2

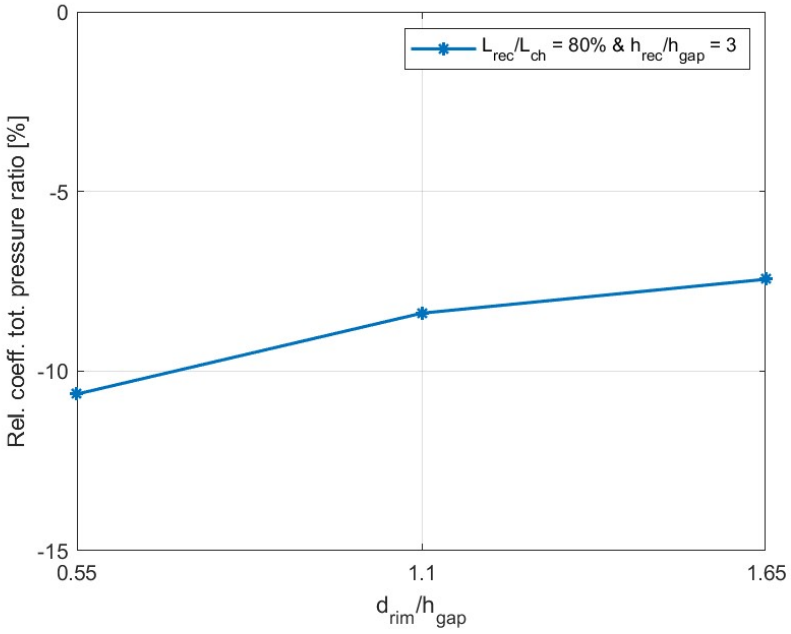


**Figure 6.24:** Total pressure coefficient ratio within the tip cavity, step 2

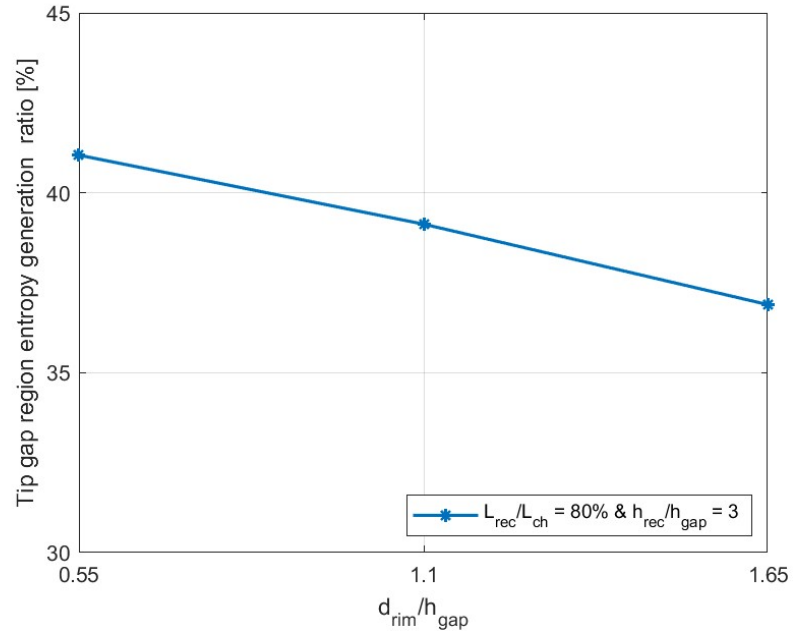


**Figure 6.25:** Entropy generation ratio within the tip cavity, step 2

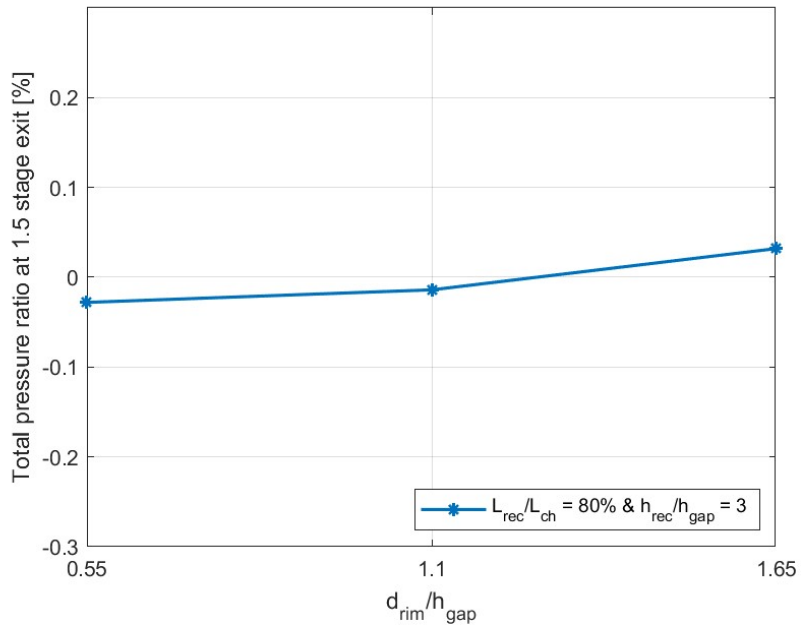


**Figure 6.26:** Total pressure ratio at the 1.5 stage exit, step 2

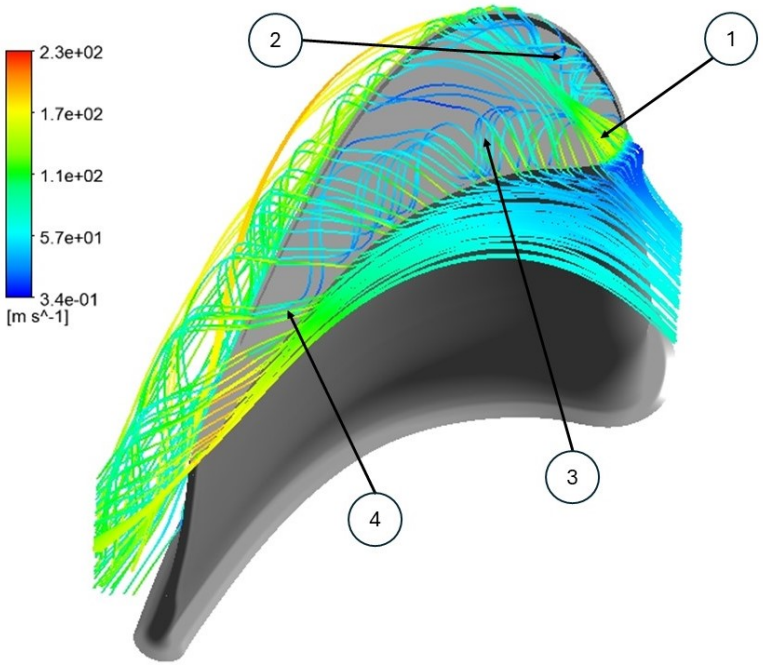


**Figure 6.27:** Vortical structures within the rotor blade cavity

the blade. In contrast to the previous streamlines, these do not form a vortical structure inside the recess. Instead, they are constrained by the aforementioned vortex and are forced to flow right against the shroud casing. They traverse the tip blade with minimal interaction and they merge with the tip leakage vortex already formed upstream.

To analyze in detail the vortical structures described, velocity vectors are displayed in Figure 6.28 along with the velocity magnitude inside the cavity for four distinct planes perpendicular to the main axis of rotation.

The streamwise evolution of the vortices is captured, illustrating the flow behavior within the recessed cavity. Close to the leading edge internal rim, the vortex exhibits a parallel orientation relative to the measurement plane. The flow in the inner area of the cavity experiences relatively uniform velocity while the vortical motion depends on the side which the structure is against to, pressure or suction side. It is important to highlight the ineffectiveness of the vortex in limiting the mass flow crossing the tip blade, as evidenced by the elevated velocity values present in the upper layer of the gap.

As the flow advances along the axial chord, the two vortices create well-defined and separate vortical structures one for each side of the internal rims. The overall velocity in the cavity decreases, reaching its minimum values at the centers of

the vortices, while the fluid closer to the external casing experiences a reduction in velocity and a change in direction consistent with the vortex rotations. At approximately 40% in the streamwise direction, the suction side vortex disappears in a more homogeneous flow, whereas the pressure side vortex expands, ultimately occupying half of the cavity area. This visualization technique also reveals the formation of a third smaller vortex situated in the central upper region of the gap, positioned directly against the shroud wall. This structure appears to clearly working as an aerodynamic seal, as evidenced by the lower velocity observed in that region compared to upstream.

Moving further downstream, the recess flow is almost entirely under the influence of the pressure side vortex. The sealing effect seems to vanish proceeding towards the trailing edge, causing the shroud casing boundary layer to gain velocity and realigning towards the suction side. This transition allows for an increasing mass flow to leak from the gap, indicating a gradual loss of the intended sealing effect as the flow evolves.

After thoroughly examining the aerodynamic behavior of the tip gap region, some considerations emerge specifically related to the recessed tip study implemented.

Firstly, it is evident that the leakage reduction experienced for all the configurations tested is closely related to the velocity decrease in magnitude, which is up to 44% compared to the original flat tip case in the geometry resulting from the second step of the analysis. In fact, the slow recirculation forces the flow to remain contained in the cavity and effectively functioning as an aerodynamic seal for the new mass entering from the pressure side. This behavior is further supported by the rising of the static pressure inside the gap compared to the flat case, contributing to the leakage reduction by diminishing the pressure difference between blade sides. Moreover, a significant correlation between tip gap velocity reduction, which directly influences the tip leakage mass flow, and the increase in cavity volume is identified. Figure 6.29 and Figure 6.30 illustrate these relationships among all the simulations tested, highlighting, by red curves, the downward trends for both the quantities with the increased volume.

Unfortunately, a drawback of this process is the reduction in total quantities inside the cavity, in particular total pressure, along with an increase in the entropy generation, by approximately 41% in the configuration shown in Figure 6.25. Consequently, the relative total pressure coefficient, presented in Figure 6.17 and Figure 6.24, which accounts for the total pressure losses in the tip gap, reflects a decrease, hence a losses increase, for geometries with larger cavity volumes.

Nevertheless, these drawbacks are effectively counterbalanced by the improvements in mass flow leakage, which leads to an overall entropy generation reduction downstream as introduced in the Section 6.4. This hypothesis is further supported by Figure 6.19 and Figure 6.26, which demonstrate a nearly complete recovery of

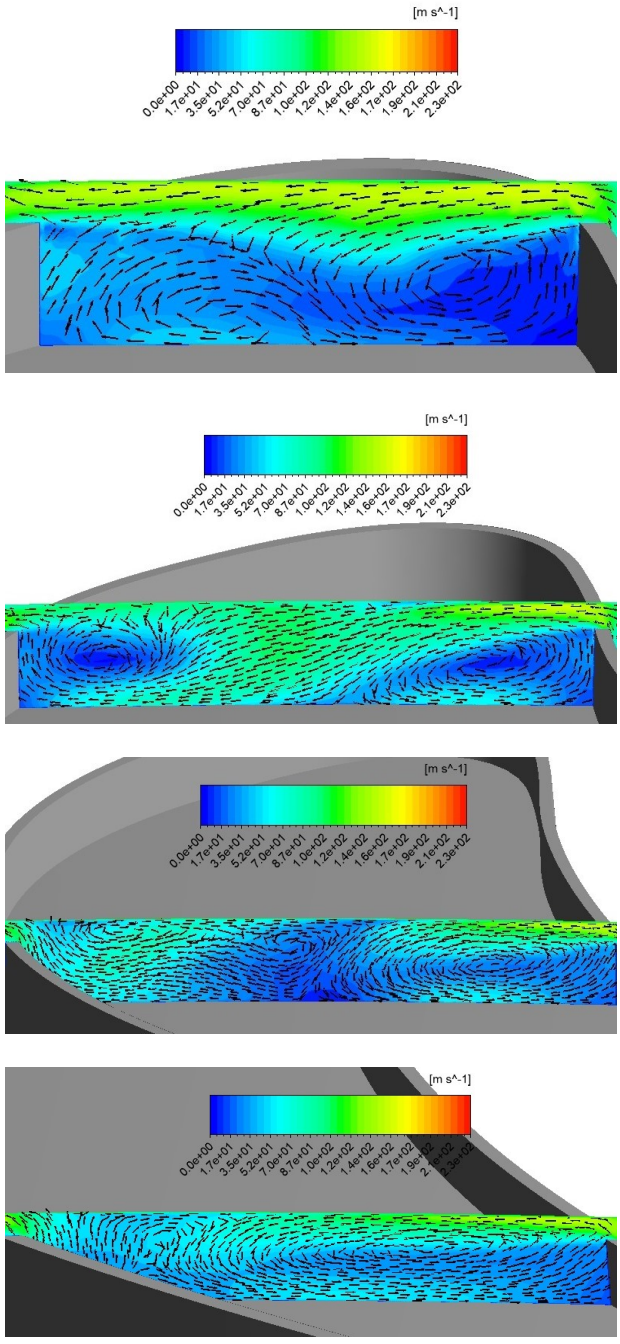


**Figure 6.28:** Velocity magnitude and velocity vectors for 15%, 20%, 40% and 60% of the axial chord

total pressure downstream of the second stator, achieving values comparable to, if not identical with, those of the flat tip baseline configuration. The consequent efficiency increase is therefore attributed to the reduction in entropy generation, displayed in Figure 6.15 and Figure 6.22.

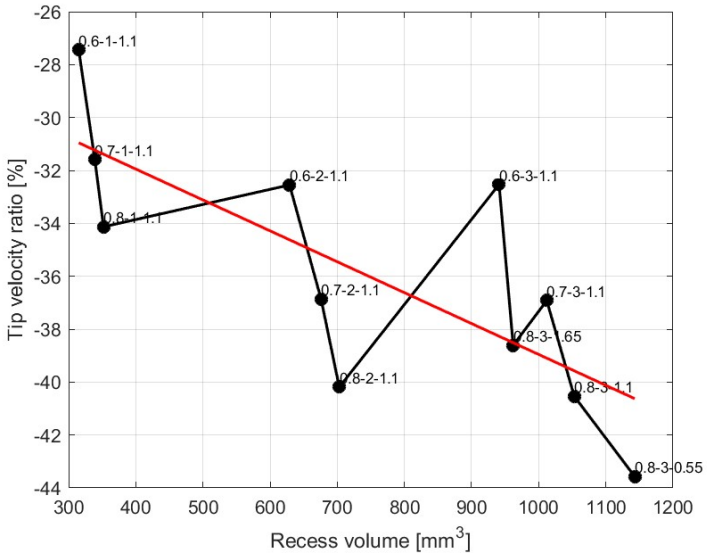


**Figure 6.29:** Tip gap velocity ratio for the tested geometries

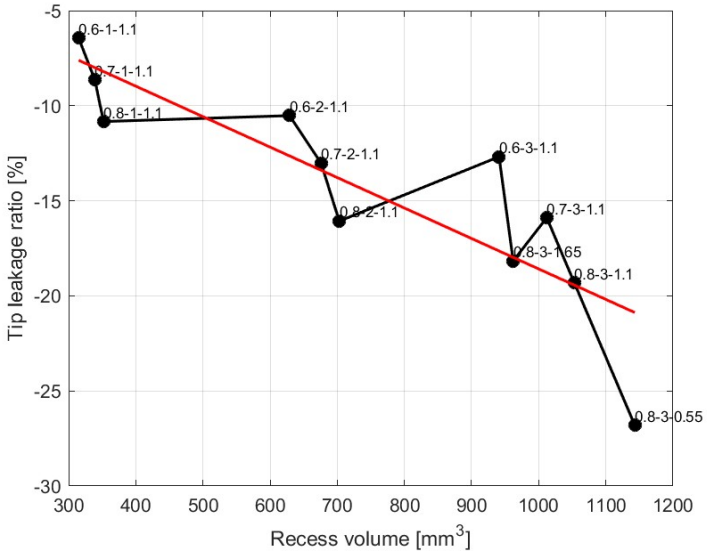


**Figure 6.30:** Tip gap leakage mass flow ratio for the tested geometries

# Chapter 7

# Conclusion

In the current study, computational fluid dynamics (CFD) simulations have been conducted on an unshrouded, 1.5 stage axial turbine using the commercial software Ansys. A significant validation process has been performed, using as reference the LISA-D turbine facility at the ETH Zurich. For ease of numerical implementation, the following modeling assumptions have been applied: steady-state conditions, no casing cavities for secondary flow inflation and perfectly smooth domain walls. Despite the significant approximations considered for the analysis, the results displayed a high degree of accuracy, showing an overall isentropic efficiency discrepancy of 0.78% between the experimental setup tested and the resulting CFD simulation from the validation process.

Furthermore, the study has been focused on the investigation of recessed tip on rotor blades for potential performance improvements, using the validated flat-tip simulation as the baseline. Different cavities in the tip surface have been tested, producing a structured, two-step parametric study and focusing on the effects of length, depth and width of the new cavities created. A total of eleven simulations has been performed to assess benefits and limitations of the tip recess technique by comparing the most significant parameters such as tip gap leakage mass flow, total pressure losses and entropy generation.

The analysis conducted revealed a unique relationship between rotor tip cavity volume and aerodynamic optimization of the turbine. The vortical structures forming within the recess, and the subsequent significant reduction of the tip gap flow velocity, are key factors for the creation of an aerodynamic sealing effect in the cavity. This results in minimizing the secondary mass flow mixing with main axial stream. For the best case tested, which corresponds to the largest cavity volume analyzed, the derived decrease of entropy generation is up to 6.8%. As an ultimate result, efficiency gains of up to 0.95% were achieved, along with a tip gap leakage mass flow reduction of approximately 27%, relative to the flat-tip configuration. Those achievements, in terms of performance of the machine, show the benefit

and importance of tip gap recess techniques and, more in general, the necessity of numerical analysis for a precise and useful definition of the machine aerodynamics.

In conclusion, the work conducted could be referred as foundational analysis for future studies on passive methods for enhancing turbine performance. While the focus of the current project has been the modifications of the three primary dimensions which characterized the recess cavity, further investigations could explore local geometric adjustments, such as rounding the rim edges or smoothing the cavity floor, to assess whether these refinements yield aerodynamic benefits without introducing sharp geometries. Moreover, the analyzed configuration could be combined with other modifications, including winglets, curvature adjustments on the blade's external surfaces, or casing refinements.

Regarding the CFD analysis, the comparison of different turbulence models for the RANS equation system could be an interesting objective for further insight, as well as the implementation of specific velocity profile for boundary layer at the turbine inlet with the aim to assess the impact on secondary flows. Furthermore, higher complexity could also be introduced into the numerical simulation, investigating how much unsteady solutions differ from the current results or incorporating secondary flow inflation to study its interaction with tip leakage flow.

Finally, the configurations analyzed could be experimentally tested in real environment, confirming the benefits assessed during this study. In conclusion, the present work is certainly suitable for being a robust baseline for future analysis and improvements, positioning it as a valuable reference for ongoing research in this area.

# Bibliography


[1] Rolls-Royce. *UltraFan - The ultimate Turbofan.* URL: `https://www.rolls-royce.com/innovation/ultrafan.aspx` (visited on 10/11/2024) (cit. on p. 2).

[2] B.V.R Ravi Kumar. «A REVIEW ON BLISK TECHNOLOGY». In: *International Journal of Innovative Research in Science, Engineering and Technology* 2 (2013), pp. 1353–1358 (cit. on p. 1).

[3] J. D. Denton. «The 1993 IGTI Scholar Lecture: Loss Mechanisms in Turbomachines». In: *Journal of Turbomachinery* 115.4 (Oct. 1993), pp. 621–656 (cit. on pp. 2, 4, 57, 71).

[4] D. Dey and C. Camci. «Development of tip clearance flow downstream of a rotor blade with coolant injection from a tip trench». In: (Jan. 2000) (cit. on p. 4).

[5] N. M. Rao and C. Camci. «Axial Turbine Tip Desensitization by Injection From a Tip Trench: Part 1 — Effect of Injection Mass Flow Rate». In: Turbo Expo: Power for Land, Sea, and Air Volume 5: Turbo Expo 2004, Parts A and B (June 2004), pp. 1075–1088 (cit. on p. 4).

[6] N. M. Rao and C. Camci. «Axial Turbine Tip Desensitization by Injection From a Tip Trench: Part 2 — Leakage Flow Sensitivity to Injection Location». In: Turbo Expo: Power for Land, Sea, and Air Volume 5: Turbo Expo 2004, Parts A and B (June 2004), pp. 1089–1098 (cit. on p. 4).

[7] M. Rezasoltani, M. T. Schobeiri, and J. C. Han. «Experimental Investigation of the Effect of Purge Flow on Film Cooling Effectiveness on a Rotating Turbine With Nonaxisymmetric End Wall Contouring». In: *Journal of Turbomachinery* 136.9 (May 2014) (cit. on p. 5).

[8] M. G. Rose. «Non-Axisymmetric Endwall Profiling in the HP NGV's of an Axial Flow Gas Turbine». In: Turbo Expo: Power for Land, Sea, and Air Volume 1: Turbomachinery (June 1994) (cit. on p. 5).

[9] N. W. Harvey, M. G. Rose, M. D. Taylor, S. Shahpar, J. Hartland, and D. G. Gregory-Smith. «Nonaxisymmetric Turbine End Wall Design: Part I—Three-Dimensional Linear Design System ». In: *Journal of Turbomachinery* 122.2 (Feb. 1999), pp. 278–285 (cit. on p. 5).

[10] J. C. Hartland, D. G. Gregory-Smith, N. W. Harvey, and M. G. Rose. «Nonaxisymmetric Turbine End Wall Design: Part II—Experimental Validation ». In: *Journal of Turbomachinery* 122.2 (Feb. 1999), pp. 286–293 (cit. on p. 5).

[11] T. Germain, M. Nagel, I. Raab, P. Schüpbach, R. S. Abhari, and M. Rose. «Improving Efficiency of a High Work Turbine Using Nonaxisymmetric Endwalls—Part I: Endwall Design and Performance». In: *Journal of Turbomachinery* 132.2 (Jan. 2010) (cit. on p. 5).

[12] P. Schuepbach, R. S. Abhari, M. G. Rose, T. Germain, I. Raab, and J. Gier. «Improving Efficiency of a High Work Turbine Using Non-Axisymmetric Endwalls: Part II—Time-Resolved Flow Physics». In: Turbo Expo: Power for Land, Sea, and Air Volume 6: Turbomachinery, Parts A, B, and C (June 2008), pp. 1121–1133 (cit. on p. 5).

[13] N. Harvey, G. Brennan, D. Newman, and M. Rose. «Improving Turbine Efficiency Using Non-Axisymmetric End Walls: Validation in the Multi-Row Environment and With Low Aspect Ratio Blading». In: Jan. 2002 (cit. on p. 5).

[14] P. Gonza´lez, M. Lantero, and V. Olabarria. «Low Pressure Turbine Design for Rolls-Royce Trent 900 Turbofan». In: Turbo Expo: Power for Land, Sea, and Air Volume 6: Turbomachinery, Parts A and B (May 2006), pp. 875–881 (cit. on p. 5).

[15] J. T. Chung and T. W. Simon. «Effectiveness of the Gas Turbine Endwall Fences in Secondary Flow Control at Elevated Freestream Turbulence Levels». In: Turbo Expo: Power for Land, Sea, and Air Volume 1: Aircraft Engine; Marine; Turbomachinery; Microturbines and Small Turbomachinery (May 1993) (cit. on p. 5).

[16] N. V. Aunapu, R. J. Volino, K. A. Flack, and R. M. Stoddard. «Secondary Flow Measurements in a Turbine Passage With Endwall Flow Modification ». In: *Journal of Turbomachinery* 122.4 (Feb. 2000), pp. 651–658 (cit. on p. 5).

[17] L. Offenberg, J.D. Fischer, and T. Vande. «An experimental investigation of turbine case treatments». In: *23rd Joint Propulsion Conference*. June 1987 (cit. on p. 5).

[18] T. C. Booth, P. R. Dodge, and H. K. Hepworth. «Rotor-Tip Leakage: Part I—Basic Methodology». In: *Journal of Engineering for Power* 104.1 (Jan. 1982), pp. 154–161 (cit. on p. 5).

[19] A. A. Ameri, E. Steinthorsson, and D. L. Rigby. «Effect of Squealer Tip on Rotor Heat Transfer and Efficiency». In: *Journal of Turbomachinery* 120.4 (Oct. 1998), pp. 753–759 (cit. on p. 5).

[20] H. Yang, S. Acharya, S. V. Ekkad, C. Prakash, and R. Bunker. «Flow and Heat Transfer Predictions for a Flat-Tip Turbine Blade». In: Turbo Expo: Power for Land, Sea, and Air Volume 3: Turbo Expo 2002, Parts A and B (June 2002), pp. 271–283 (cit. on pp. 5, 21).

[21] H. Yang, S. Acharya, S. V. Ekkad, C. Prakash, and R. Bunker. «Numerical Simulation of Flow and Heat Transfer Past a Turbine Blade With a Squealer-Tip». In: Turbo Expo: Power for Land, Sea, and Air Volume 3: Turbo Expo 2002, Parts A and B (June 2002), pp. 295–307 (cit. on p. 5).

[22] C. Camci, D. Dey, and L. Kavurmacioglu. «Aerodynamics of Tip Leakage Flows Near Partial Squealer Rims in an Axial Flow Turbine Stage ». In: *Journal of Turbomachinery* 127.1 (Feb. 2005), pp. 14–24 (cit. on p. 5).

[23] S. K. Krishnababu, P. J. Newton, W. N. Dawes, G. D. Lock, H. P. Hodson, J. Hannis, and C. Whitney. «Aerothermal Investigations of Tip Leakage Flow in Axial Flow Turbines—Part I: Effect of Tip Geometry and Tip Clearance Gap». In: *Journal of Turbomachinery* 131.1 (Oct. 2008) (cit. on p. 6).

[24] S. De Cecco, M. I. Yaras, and S. A. Sjolander. «Measurements of the Tip-Leakage Flow in a Turbine Cascade With Large Clearances». In: Turbo Expo: Power for Land, Sea, and Air Volume 1: Turbomachinery (June 1995) (cit. on p. 6).

[25] S. Acharya, H. Yang, C. Prakash, and R. Bunker. «Numerical Study of Flow and Heat Transfer on a Blade Tip With Different Leakage Reduction Strategies». In: Turbo Expo: Power for Land, Sea, and Air Volume 5: Turbo Expo 2003, Parts A and B (June 2003), pp. 471–480 (cit. on p. 6).

[26] A. K. Saha, S. Acharya, C. Prakash, and R. Bunker. «Blade Tip Leakage Flow and Heat Transfer With Pressure-Side Winglet». In: Turbo Expo: Power for Land, Sea, and Air Volume 5: Turbo Expo 2003, Parts A and B (June 2003), pp. 497–507 (cit. on p. 6).

[27] C. Zhou, H. Hodson, I. Tibbott, and M. Stokes. «Effects of Winglet Geometry on the Aerodynamic Performance of Tip Leakage Flow in a Turbine Cascade». In: *Journal of Turbomachinery* 135.5 (June 2013), p. 051009 (cit. on p. 6).

[28] J. D. Coull, N. R. Atkins, and H. P. Hodson. «Winglets for Improved Aerothermal Performance of High Pressure Turbines». In: *Journal of Turbomachinery* 136.9 (May 2014) (cit. on p. 6).

[29] C. H. Sieverding. «Recent Progress in the Understanding of Basic Aspects of Secondary Flows in Turbine Blade Passages». In: *Journal of Engineering for Gas Turbines and Power* 107.2 (Apr. 1985), pp. 248–257 (cit. on p. 7).

[30] L. Langston. «Secondary Flows in Axial Turbines—A Review». In: *Annals of the New York Academy of Sciences* 934 (June 2001), pp. 11–26 (cit. on p. 7).

[31] L. S. Langston, M. L. Nice, and R. M. Hooper. «Three-Dimensional Flow Within a Turbine Cascade Passage». In: *Journal of Engineering for Power* 99.1 (Jan. 1977), pp. 21–28 (cit. on p. 7).

[32] C. H. Sieverding and P. Van den Bosche. «The use of coloured smoke to visualize secondary flows in a turbine-blade cascade». In: *Journal of Fluid Mechanics* 134 (1983), pp. 85–89 (cit. on p. 7).

[33] B. Mischo, T. Behr, and R. S. Abhari. «Flow Physics and Profiling of Recessed Blade Tips: Impact on Performance and Heat Load». In: *Journal of Turbomachinery* 130.2 (Feb. 2008) (cit. on pp. 7, 8, 78).

[34] F. Zeng, W. Zhang, Y. Wang, X. Cao, and Z. Zou. «Effects of Squealer Geometry of Turbine Blade Tip on the Tip-Leakage Flow and Loss». In: *Journal of Thermal Science* 30 (2021), pp. 1376–1387 (cit. on p. 8).

[35] Z. Zou, F. Shao, Y. Li, W. Zhang, and A. Berglund. «Dominant flow structure in the squealer tip gap and its impact on turbine aerodynamic performance». In: *Energy* 138 (2017), pp. 167–184 (cit. on p. 8).

[36] Global Platform for the Sustainable Development of Air Transport. *GPPS Data Sets 2021*. 2021. URL: `https://gpps.global/gpps-data-sets-2021/` (visited on 10/20/2024) (cit. on pp. 9–11).

[37] T. Behr, A. I. Kalfas, and R. S. Abhari. «Unsteady Flow Physics and Performance of a One-and-12-Stage Unshrouded High Work Turbine». In: *Journal of Turbomachinery* 129.2 (June 2006), pp. 348–359 (cit. on p. 10).

[38] T. Behr. «Control of rotor tip leakage and secondary flow by casing air injection in unshrouded axial turbines». PhD thesis. Zurich, Switzerland: ETH Zurich, 2007 (cit. on pp. 10, 12).

[39] P. S. Rebholz. «Aeromechanical Challenges of Shrouded Low Pressure Turbines for Geared Turbofan Engines». PhD thesis. Zürich: ETH Zürich, 2017 (cit. on p. 11).

[40] ANSYS, Inc. *Ansys CFX-Solver Theory Guide*. Release 2021 R2. ANSYS, Inc. 2021 (cit. on pp. 16, 26, 32).

[41] H. Schlichting. *Boundary Layer Theory*. 7th. McGraw-Hill, 1979 (cit. on p. 24).

[42] ANSYS, Inc. *Ansys TurboGrid User's Guide*. Release 2021 R2. ANSYS, Inc. 2021 (cit. on p. 24).

[43] ANSYS, Inc. *Ansys CFX-Solver Modeling Guide*. Release 2021 R2. ANSYS, Inc. 2021 (cit. on pp. 26, 28, 33, 34).

[44] Bob Mischo. «Axial Turbine Rotor: Aero-thermal Blade Tip Performance Improvement through Flow Control». PhD thesis. Zurich, Switzerland: Swiss Federal Institute of Technology Zurich (ETH Zurich), 2008 (cit. on pp. 57, 58, 67).